Cryogenic deformation of CoCrFeMnNi with a focus on serrated plastic deformation

Zur Erlangung des akademischen Grades eines

DOKTORS DER INGENIEURWISSENSCHAFTEN (DR.-ING.)

von der KIT-Fakultät für Maschinenbau

des Karlsruher Instituts für Technologie (KIT)

angenommene

DISSERTATION

von

M.Tech. Aditya Srinivasan Tirunilai

Tag der mündlichen Prüfung: 09.06.2021

Hauptreferent: **Prof. Dr.-Ing. Martin Heilmaier**
Institut für Angewandte Materialien (IAM)
Karlsruher Institut für Technologie (KIT)

Korreferent: **Prof. Dr.-Ing. Gunther Eggeler**
Lehrstuhl Werkstoffwissenschaft (WW)
Ruhr-Universität Bochum (RUB)

Cryogenic deformation of CoCrFeMnNi with a focus on serrated plastic deformation

For the purpose of obtaining the academic degree of

DOCTOR OF ENGINEERING (ENG.D.)

from the KIT-Faculty of Mechanical Engineering

of the Karlsruhe Institute of Technology (KIT)

accepted

DISSERTATION

from

M.Tech. Aditya Srinivasan Tirunilai

Day of oral examination: 09.06.2021

First referee**:** **Prof. (Eng. D.) Martin Heilmaier**
Institute for Applied Materials (IAM)
Karlsruhe Institute of Technology (KIT)

Co-referee**:** **Prof. (Eng. D.) Gunther Eggeler**
Chair of Materials Science (WW)
Ruhr University Bochum (RUB)

Kurzfassung

Legierungen, die aus mehreren Hauptelementen bestehen, werden als komplexe, konzentrierte Legierungen (englisch „compositionally complex alloys“) oder konfigurationsentropiestabilisierte Legierungen (englisch „high entropy alloys“) bezeichnet und haben in der jüngeren Vergangenheit aufgrund ihrer teilweise besonderen Eigenschaften auf sich gezogen großes Forschungsinteresse. So weisen kubisch flächenzentrierte Legierungen des Systems Co-Cr-Fe-Mn-Ni und seines Subsystems Co-Cr-Ni eine hervorragende Kombination aus Tieftemperaturfestigkeit und Duktilität bzw. Zähigkeit auf. Während in der Vergangenheit eine solide Grundlage für das Verständnis des temperaturabhängige Verformungsverhaltens dieser Legierungen geschaffen wurde, wurden diese nicht weitergehend bei Temperaturen noch unterhalb von 77 K untersucht.

In der vorliegenden Arbeit wird das Verformungsverhalten sowohl von äquimolarem CoCrFeMnNi als auch von CoCrNi im Temperaturbereich zwischen 295 K und 4,2 K eingehend untersucht. Dabei werden Hypothesen aus der Literatur zum Verformungsverhalten und den auftretenden Verformungsmechanismen in diesem Temperaturbereich überprüft und verifiziert. Darüber hinaus zeigen diese Legierungen, insbesondere CoCrFeMnNi, eine einzigartig stark ausgeprägte, diskontinuierliche Verformung bei sehr tiefen Temperaturen. Dieses Phänomen wird ebenfalls genauer beleuchtet und die Ausprägung sowie dessen möglicher Ursprung auf Basis der theoretischen Grundlagen der Tieftemperaturplastizität untersucht und diskutiert.

Das Auftreten von Verformungszwillingen sowohl in CoCrFeMnNi als auch in CoCrNi wird bei kryogenen Temperaturen bestätigt, und die Beschreibung des Beitrages von Verformungszwillingen zur Kaltverfestigung wird bis auf 4,2 K erweitert. Außerdem zeigte sich, dass der in CoCrNi gebildete ε-Martensit keine deutliche Festigkeits- bzw. Verfestigungssteigerung hervorruft, was mit dem Entstehungsmechanismus des ε-Martensits begründet werden kann.

Bei Temperaturen nahe 0 K zeigen sowohl CoCrFeMnNi als auch CoCrNi eine diskontinuierliche plastische Verformung. Während über dieses Phänomen bereits 1957 berichtet wurde, gibt es bis heute verschiedene Hypothesen zu dessen Erklärung. In der

aktuellen Arbeit konnte bestätigt werden, dass diese Art der diskontinuierlichen plastischen Verformung aus dem Aufstau von Versetzungen an sesshaften Lomer-Cottrell-Versetzungen resultiert. Diese können aufgrund mangelnder thermischer Aktivierung bei sehr tiefen Temperaturen nicht durch Quergleiten umgangen werden. Durch systematische Untersuchungen wurden alternative Hypothesen ausgeschlossen und das auf dem Versetzungsaufstau beruhende Modell verifiziert. Dabei wurden aktuelle und zuvor veröffentlichte Ergebnisse validiert. Dabei stellt sich CoCrFeMnNi als eine nahezu optimale Modell-Legierung dar, da die diskontinuierliche Verformung und die damit verbundenen Phänomene deutlich ausgeprägter sind als bei anderen binären oder ternären Legierungen.

Abstract

Alloys composed of multiple principal elements, called concentrated complex alloys or high entropy alloys have garnered significant interest in the recent past. Among these alloys FCC CoCrFeMnNi and CoCrNi reportedly have an excellent combination of cryogenic strength and ductility. While a firm foundation has been laid out in understanding the deformation behavior of these alloys, the studies have not been investigated temperatures below 77 K.

In the current work the deformation characteristics of both CoCrFeMnNi and CoCrNi are investigated in the temperature range between 295 K and 4.2 K. Through this, hypotheses from previous literature are verified. Additionally, these alloys, specifically CoCrFeMnNi, show some peculiar discontinuous deformation at very low temperatures. This phenomenon is also investigated and the nature and possible origins of the same examined.

The importance of deformation twinning in both CoCrFeMnNi and CoCrNi is presently confirmed at cryogenic temperatures, and the previous observations of twinning contribution to work-hardening at 77 K is extended down to 4.2 K. However, other hypotheses, including the proposed formation of ε-martensite in CoCrFeMnNi at 4.2 K were invalidated. Additionally, it was seen that the ε-martensite formed in CoCrNi provides no distinct strengthening benefit despite such an expectation.

At temperatures close to 0 K, both CoCrFeMnNi and CoCrNi show discontinuous or serrated plastic deformation. While this phenomenon has been reported as early as 1957, there are multiple hypotheses associated with it. In the current work the nature of the serrated plastic deformation was confirmed to be the result of dislocation pile-ups at LC locks, as a result of cross-slip inability at very low temperatures. Through a series of tests, alternate hypotheses were disregarded and the model based on dislocation pile-ups was established to validate current and previously published results. CoCrFeMnNi was an effective probe material exaggerating the phenomenon, making it easier to distinguish the effects under different conditions. This test case demonstrates that concentrated complex alloys can act as probe materials with embellished characteristics making them ideal when attempting to investigate specific phenomena.

Abbreviations

APT	Atom Probe Tomography
ASD	Atomic Size Difference
BCC	Body Centered Cubic
BSE	Back Scattered Electrons
DFT	Density Functional Theory
DIC	Digital Image Correlation
EBSD	Electron Back-Scatter Diffraction
EDS	Energy Dispersive Spectroscopy
FCC	Face Centered Cubic
FFT	Fast Fourier Transform
FIB	Focused Ion Beam
FWHM	Full Width Half Maximum
GND	Geometrically Necessary Dislocations
HAGB	High Angle Grain Boundary
HCP	Hexagonal Close Packed
HEA	High Entropy Alloy
HSFE	High Stacking Fault Energy
ICP-OES	Inductively Coupled Plasma Optical Emission Spectroscopy
iFFT	Inverse Fast Fourier Transform
IPF	Inverse Pole Figure
KAM	Kernal Average Misorientation

LC	Lomer-Cottrell
LSFE	Low Stacking Fault Energy
MEA	Medium Entropy Alloy
MSAD	Mean Square Atomic Distance
NR	Nelson-Riley
OP-S	Oxide Polishing Suspension
RT	Room Temperature
SAD	Selected Area Diffraction
SEM	Scanning Electron Microscope
SFE	Stacking Fault Energy
SFW	Stacking Fault Width
STEM-HAADF	Scanning Transmission Electron Microscopy- High Angle Annular Dark Field
TEM	Transmission Electron Microscopy
TRIP	Transformation Induced Plasticity
TWIP	Twin Induced Plasticity
UTS	Ultimate Tensile Strength

Symbols

σ_e	Engineering stress
ε_e	Engineering strain
σ_t	True stress
ε_t	True strain
σ_{YS}	Yield stress
$\Delta\sigma_e$	Stress drop amplitude
σ_{max}	Maxima stress of serrations
γ_{SFE}	Stacking fault energy
G	Shear modulus
M	Taylor factor
m	Schmid factor
m_{max}	Maximum Schmid factor for a specific orientation
m_{twin}	Schmid factor for Shockley partial motion, slip system $(1\bar{1}1)[\bar{2}\bar{1}1]$, associated with twinning
m_{slip}	Schmid factor for full dislocation motion, slip system $(1\bar{1}1)[\bar{2}\bar{1}1]$, associated with dislocation slip
a	Basal plane lattice parameter in hexagonal crystal
c	Non-basal plane lattice parameter in hexagonal crystal
K_{HP}	Hall-Petch constant
b	Burger's vector for a given dislocation
δ	Atomic size difference
x_i	Elemental atomic composition of element i

r_i	Radius of atom of element i
$\bar{r}$	Average radius of all the elements in the alloy
K_{const}	coefficient of temperature dependent slope of $\sigma_{YS} - T$ variation
E_{CS}	Energy for cross-slip
E_{con}	Energy for constriction of extended dislocations
B	Lomer-Cottrell lock density
B_{cr}	Critical Lomer-Cottrell lock density to initiate serrations
τ_e	Shear stress at the head of a dislocation pile-up
τ_{cr}	Critical shear stress at the head of a dislocation pile-up to initiate serrations
τ_{bow}	Stress to allow for dislocation bow out
$\tilde{F}_{LC}^{+}$	Lomer-Cottrell lock formation rate as a function of change in temperature for a given dislocation density
τ	Shear stress acting on a dislocation, making it glide
F	Force on a dislocation as a result of shear stress acting on it
F_{jog}	Force on the jog dislocation
s	Dislocation line vector for a given dislocation
l_0	Length between pinning points of a dislocation
λ_{twin}	Free dislocation length in a twinned crystal
f_{twin}	Fraction of grains that can undergo twinning
λ	Thermal conductivity
C_p	Specific heat capacity
T	Temperature

Table of Contents

1 Introduction and motivation

Material science has made significant progress towards achieving the ideal metallic materials for various structural applications. This has been done both through alloy design via composition variation, as well as microstructure manipulation, through process parameter optimization. Modern metal physics has been predominantly concentrated on refining these approaches. This has resulted in a focus on alloys of specific compositions with well understood properties, and further investigations are limited to incremental variations from these compositions. These investigations are correspondingly restricted to alloys with a single major component (principal element). However, more recently a different approach and a new class of materials known as High Entropy Alloys (HEAs) have garnered significant attention [1, 2, 3, 4, 5, 6, 7, 8, 9]. These alloys consist of multiple elements (≥ 5) in significant proportion (typically between 5 and 35 at.%) as opposed to the conventional alloy design (single principal element). HEAs were reported in different phase compositions, however, the most interesting ones were those having a single phase Face Centered Cubic (FCC) [10, 11, 12, 13, 14] or Body Centered Cubic (BCC) crystal structure [15, 16, 17, 18, 19]. Among the alloys with an FCC structure, equiatomic CoCrFeMnNi was most intensely researched, showing multiple interesting features [12, 20, 21, 22, 23]. One of these features was the excellent cryogenic ductility, in combination with its strength. Otto et al. [12], had originally presented mechanical and microstructural results of the alloy, deformed at 77 K. It showed greater ductility than at ambient temperatures and significant strengthening as well. This was the result of the lowered Stacking Fault Energy (SFE) of CoCrFeMnNi at that temperature, thus activating different deformation mechanisms [21]. The decreasing SFE has additional implications at even lower temperatures. While intermediate SFE ($13 - 49\ mJ \cdot m^{-2}$) is associated activation of Twinning Induced Plasticity (TWIP) [24, 25, 26], low SFE is associated with Transformation Induced Plasticity (TRIP), specifically into Hexagonally Close Packed (HCP) ε-martensite. This is the case with equiatomic CoCrNi, a subset of the Co-Cr-Fe-Mn-Ni system [27], that shows perceivable martensite formation at cryogenic temperatures. CoCrNi has been considered an improvement on the CoCrFeMnNi alloy, based on its higher yield strength [11, 14] and its additional TRIP ability [27]. However,

certain statements made in previous publications with regards to the cryogenic deformation of CoCrFeMnNi and CoCrNi need to verified [11, 27, 28]. Specifically, the following questions need to be addressed: (i) Is CoCrNi stronger than CoCrFeMnNi on the basis of an intrinsic property like solid solution strengthening? The implied inference of Ref. [11] indicates the higher yield strength of CoCrNi at various temperatures is a direct result of the solid solution strengthening effect (ii) Does the TRIP effect strengthen CoCrNi, as stated in Ref. [27]? In CoCrNi, the TRIP effect is additionally noticeable at 77 K in comparison to its insignificant presence at Room Temperature (RT). Does the trend extend to even lower temperatures? (iii) Can CoCrFeMnNi also show the TRIP effect at sufficiently low temperatures, as hypothesized in Ref. [28]? The TWIP effect has already been activated at 77 K; would a further decrease in temperature intensify the SFE change and thus additionally activate TRIP? (iv) Considering the lowered SFE of CoCrFeMnNi at cryogenic temperatures, does CoCrNi still show a superior strength-ductility performance? While the initial results with respect to cryogenic behavior are quite promising [12, 14, 21, 27], the effect of these phenomena should not be overstated. A discrete study has been presently undertaken in order to address these questions. Additionally, to evaluate the contribution of solid solution strengthening to the inherent strength of the alloys CoCrNi and CoCrFeMnNi, CoNi was deformed under the same conditions. In contrast to CoCrNi and CoCrFeMnNi, this alloy is expectedly weakly solid solution strengthened [11]. Correspondingly, the behavior of CoNi is that of an alloy devoid of the intense effects expected in CoCrNi and CoCrFeMnNi. Chapt. 4 is focused on the deformation behavior of CoCrFeMnNi as well as CoCrNi, and serves to answer the proposed questions and justify the corresponding answers.

Apart from the general deformation behavior, CoCrFeMnNi shows additional interesting phenomena close to 0 K [29, 30, 31]. Most prominent of these interesting features is that of serrated plastic deformation occurring at very low temperatures. As seen in Fig. 1.1, it is quite distinct from continuous deformation seen at higher temperatures. While high temperature discontinuous plasticity has been a point of scientific interest which yielded a general consensus on the origins [32, 33, 34], low temperature discontinuous plasticity has no such consensus. Certain often cited hypotheses exist, along with other less popular ones [35], however, they each have their shortcomings (elaborated in Chapt. 5). Moreover, while these hypotheses give possible origins, there exists no phenomenological model explaining

the transition from continuous to discontinuous plasticity. The two main goals for the current work were therefore to (i) identify a valid basis for the phenomenon of serrated plastic deformation at cryogenic temperatures, and (ii) to develop a phenomenological model which supports both the current and previously published experimental results.

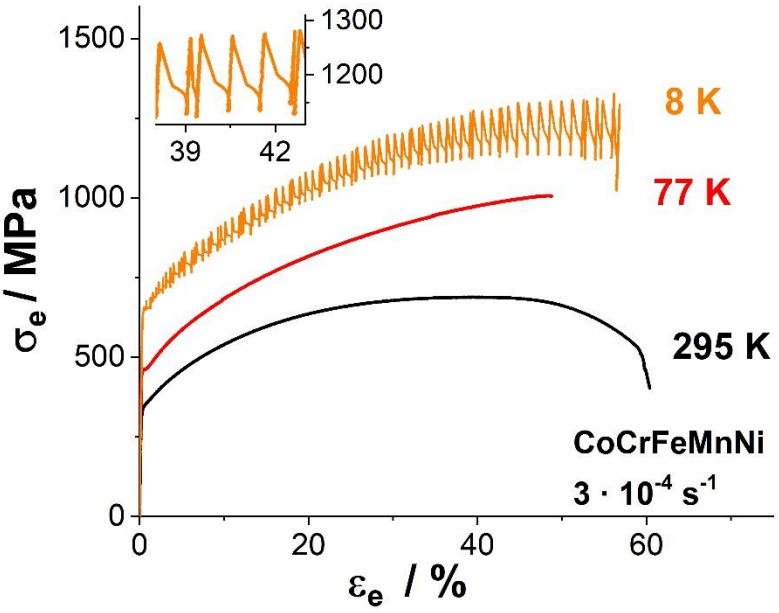

Figure 1.1: Engineering stress vs. strain diagram ($\sigma_e - \varepsilon_e$) of tensile tests conducted on equiatomic CoCrFeMnNi at 295, 77 and 8 K. The inset on the top left shows a close up of the serrations.

CoCrFeMnNi is uniquely suited to fulfilling the goal of understanding serrated plastic deformation at low temperatures. It is quite similar to the popular probe material for low temperature serrated plastic deformation study, austenitic steel (refers to multiple austenitic steels, namely 304 [36], 316 LN [37], 308 [38] and 310S [39] to name a few). However, with regards to the focused attempt at studying characteristics of this phenomenon, CoCrFeMnNi proves to be an even better candidate. The reasons for this are elaborated in Sect. 5.2 and validated by the results in Sects. 5.3, 5.4 and 5.5.

In this way the current work seeks to explain both the nature of cryogenic deformation at very low temperature in FCC CCAs, and also to explain the cause and nature of cryogenic serrated plastic deformation.

2 Experimental details

2.1 Synthesis of the material

The requisite alloys were synthesized from bulk elemental material. Co, Cr, Fe, Mn, and Ni with respective purities of 99.95%, 99.99%, 99.99%, 99.99% and 99.97%, were appropriately weighed to obtain equiatomic compositions and were then melted under an Ar atmosphere using an AM/0.5 arc melting device from the company Edmund Bühler GmbH (Germany). The Mn was pre-etched by the supplier and stored in an Argon filled container prior to the melting operation. The melting chamber was evacuated down to a pressure of $5 \cdot 10^{-2}$ mbar and then flooded with Ar. This process was repeated three times before finally evacuating to a high vacuum of less than $2 \cdot 10^{-4}$ mbar. The chamber was then flooded with Ar once more, so as to carry out the melting. During the arc melting operation the Ar pressure was initially set to 600 mbar. A Zr globule was first melted in order to getter residual oxygen in the chamber and then the elements were melted into an ingot. The ingots were flipped and re-melted five times before finally being cast as rod-shaped ingots in a water-cooled Cu mold. The rods were 175 mm long with a diameter of 14 mm for CoCrFeMnNi and 12 mm for CoCrNi and CoNi.

Homogenization of the as-cast microstructure was performed in evacuated fused silica tubes at 1200 °C for 72 h and quenched in water. The homogenized material was deformed down to 6 mm in diameter via rotary swaging, applying a reduction of approximately 20% in the individual steps[1]. Tensile test specimens were machined from these deformed rods as described in the Sect. 2.3. The machined specimens were finally recrystallized by annealing for 1 h at 800, 850 and 600 °C for CoCrFeMnNi, CoCrNi and CoNi, respectively. The recrystallization treatments were carried out in evacuated fused silica ampules and the specimens were quenched post annealing. The grain sizes subsequent to recrystallization were estimated using horizontal grain intercept method on Backscatter Electron (BSE) images. Twin boundaries were considered as High Angle Grain Boundaries (HAGB) and were included in the assessment of the mean grain sizes.

[1] This work was carried out in the laboratory of Prof. Jens Freudenberger, Metal Physics, Leibniz Institute for Solid State and Materials Research Dresden.

2.2 Materials characterization

The composition of the first batch of CoCrFeMnNi alloy in the as-cast state was determined by Inductively Coupled Plasma Optical Emission Spectrometry (ICP-OES), confirming an equiatomic composition. The compositions of the other batches were determined to be equiatomic through standard-related, Energy-Dispersive X-ray Spectroscopy (EDS). The EDS evaluations were carried out on a Zeiss EVO 50 equipped with a Thermo Scientific EDX system, Thermo Fisher Scientific. XRD analyses were carried out on recrystallized and polished longitudinal sections of the alloys with the use of a D2 Phaser system equipped with a Lynxeye line detector (Bruker, Billerica, Massachusetts). The lattice parameter was determined by extrapolating toward $\Theta = 90°$ similar to the approach by Nelson–Riley, using the weighted function $\frac{1}{2} \cdot (cot^2\Theta + cot\Theta \cdot cos\Theta)$ of the indexed planes. For the purpose of microstructural investigations, a standard metallographic procedure was used to prepare the specimens. The specimens were first ground with a series of abrasive SiC papers of increasing grit number. They were then polished using 3 µm and 1 µm diamond suspensions. This was followed by a polishing operation using a non-crystallizing Oxide Polishing Suspension (OP–S) with a pH = 9.8, supplied by Struers. Scanning Electron Microscopy (SEM) was performed using three different devices, namely a Zeiss Evo 50, Zeiss Leo 1530 and a Zeiss Auriga 60. Electron Backscatter Diffraction (EBSD) was carried out on the Auriga 60 system which is equipped with an EDAX DigiView EBSD camera system.

Transmission Electron Microscopy (TEM) analysis of deformed CoCrFeMnNi was carried out on a Tecnai F20 ST device operated at 200 kV equipped with a field emission gun and an Orius SC600 CCD camera (Institute for Nanotechnology, KIT, Karlsruhe). High Angle Annular Dark Field Scanning TEM images (STEM-HAADF) and Selected Area Diffraction (SAD) patterns were acquired to study the local crystallography and microstructure. For this purpose, target preparation was performed by in situ lift-out using the FIB of the Zeiss Auriga 60 system. Following the Pt deposition, done for the protection of the target, specimen preparation was performed using 30 kV Ga^+ ions with final polishing at 5 and 2 kV to reduce the effects of beam damage.

TEM analysis of deformed CoCrNi was performed on a Tecnai Supertwin F20 G2 instrument operating at 200 kV (Ruhr University Bochum)[2]. The specimen was ground to a thickness of 100 µm using 600-grit SiC paper and further thinned by double-jet electrochemical thinning at 16 V. The electrolyte consisted of 70 vol% Methanol, 20 vol% Glycerine, and 10 vol% Perchloric acid and the operation was carried out at a temperature of 253 K. The high-resolution TEM images were subjected to fast Fourier transform (FFT) and subsequent inverse fast Fourier transform (iFFT) to isolate and identify distinct features. In this process, the FFT result of the HRTEM image gives an intensity map in the reciprocal space. This is similar to the SAD pattern. Correspondingly, each intensity maximum can be correlated with a different set of planes of a given crystal structure/phase. iFFT processing of this FFT result can be performed by selectively, focusing on or ignoring specific intensity maxima. The resultant image is similar to the original HRTEM based image, but only for the selected planes of selected phases. This region correspondingly appears in focus and can be seen as sets atomic columns perpendicular to the image plane. Regions with other phases, that were intentionally ignored, appear out of focus and are hence undiscernible in this final image. This process of selecting specific intensities from the FFT processed image and recreating the final image through iFFT is called "applying masks". Using the program "Digital Micrograph", FFTs were estimated, and masks were subsequently applied.

2.3 Mechanical testing

Tensile tests have been performed at RT (RT ~ 295 K) and a range of cryogenic temperatures, down to a minimum of 4.2 K. These tests were performed at the Cryogenic Material Test Lab Karlsruhe (CryoMaK, KIT). The cylindrical tensile specimens have M6 connecting threads, a total length of 45 mm, a uniform length of 22 mm, a transition radius of 10 mm and a gauge diameter of 4 mm. A schematic representation of this is seen in Fig. 2.1. Furthermore, the recrystallization treatment (see section 2.1) was performed after the machining and polishing steps, in order to prevent any effect from deformed surface layers. Tensile tests performed at temperatures down to 8 K were carried out on the machine MTS 25, while those conducted at 4.2 K and 77 K were carried out in a liquid helium and nitrogen

[2] Work carried out by Christian Reinhart in the laboratory of Prof. Guillaume Laplanche in Ruhr University of Bochum.

baths, respectively, in the machine ATLAS and MTS 100 (further information on machines available in Ref. [40]). Tensile testing was performed until fracture, with constant crosshead movement under standard conditions according to ASTM E8M. The elongation was measured using two extensometers attached to the specimens. Based on the measured force, elongation data and the specimen dimensions, other parameters such as stress, strain, work-hardening, true stress and true strain were derived. This was done using the proprietary software package Origin 2020b by OriginLab. Additionally, with reference to the observed serrations, the maxima and minima of each of these serrations were identified using an in-house script, using MATLAB R2018a (MathWorks) which was then used in the estimation of the work-hardening rate.

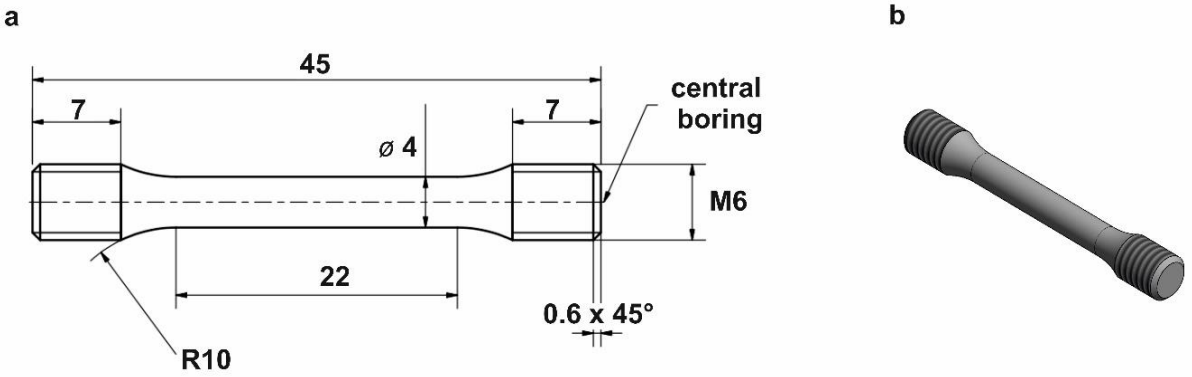

Figure 2.1: (a) Schematic representation of tensile specimen with dimensions specified in mm.
(b) 3-D model of the corresponding tensile specimen.

3 Initial state

Considering that the primary focus of the research was on the deformation behavior and associated phenomena for CoCrFeMnNi, a standard initial state was established and consistently reproduced prior to mechanical testing. Additionally, CoCrNi and CoNi specimens were prepared to compare certain specific features. To ensure a fair comparison, these alloys were processed to achieve similar standard initial states.

3.1 Microstructural characterization

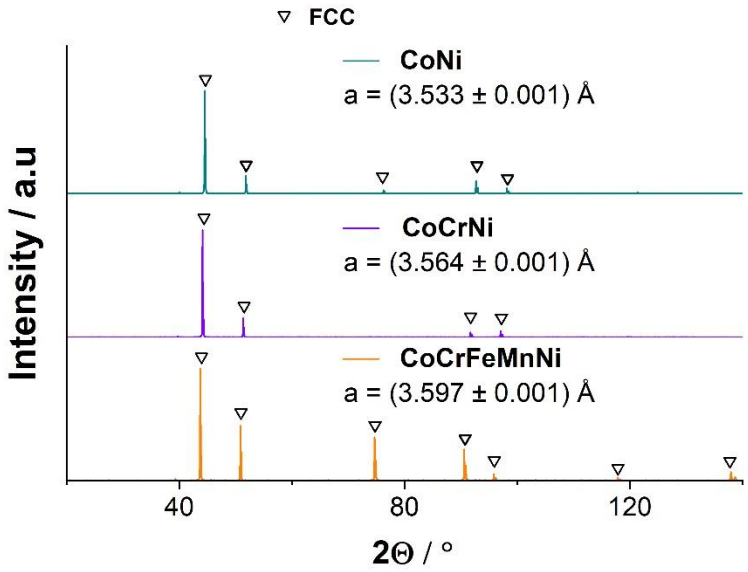

Figure 3.1: XRD results for CoCrFeMnNi, CoCrNi and CoNi. All three alloys are of single-phase FCC crystal structure. The lattice parameters were determined using a Nelson-Riley type approach (section 2.2).

The XRD results shown in Fig. 3.1 confirm that all the investigated alloys are single-phase FCC (Cu prototype). The corresponding lattice parameters, as determined from a Nelson-Riley type function as described in section 2.2, is included in the figure. This is fairly consistent with the lattice parameters determined in Refs. [14, 27, 41]. The values are provided in Tab. 3.1. The lattice parameter values measured through SAD analysis in Ref. [27], are slightly greater than those in the current work and those estimated by Laplanche et al. [14]. It is, however, unclear if this SAD analysis was carried out on a strain

free specimen. Any straining in the specimen could lead to lattice parameter estimation under non-ideal circumstances.

Table 3.1: Lattice parameter values for CoCrFeMnNi, CoCrNi and CoNi as determined through XRD in the current results as well as in Refs. [14, 27, 41].

Alloy	Lattice paramter / Å	Source
CoCrFeMnNi	3.597	Current work
CoCrFeMnNi	3.59	Bhattacharjee et al. [41]
CoCrNi	3.564	Current work
CoCrNi	3.567	Laplanche et al. [14]
CoCrNi	3.59	Miao et al. [27]
CoNi	3.53	Current work

The average grain size for CoCrFeMnNi, CoCrNi and CoNi , as determined by horizontal line intercept method, is 6.3 $\pm$ 0.5 µm , 5.8 $\pm$ 0.6 µm and 7.0 $\pm$ 1.1 µm respectively. The grain size was determined using horizontal grain intercept method on BSE orientation contrast images like those shown in Fig. 3.2, containing approximately 1500 – 2000 grains. Twin boundaries were considered to be arbitrary High Angle Grain Boundaries (HAGB).

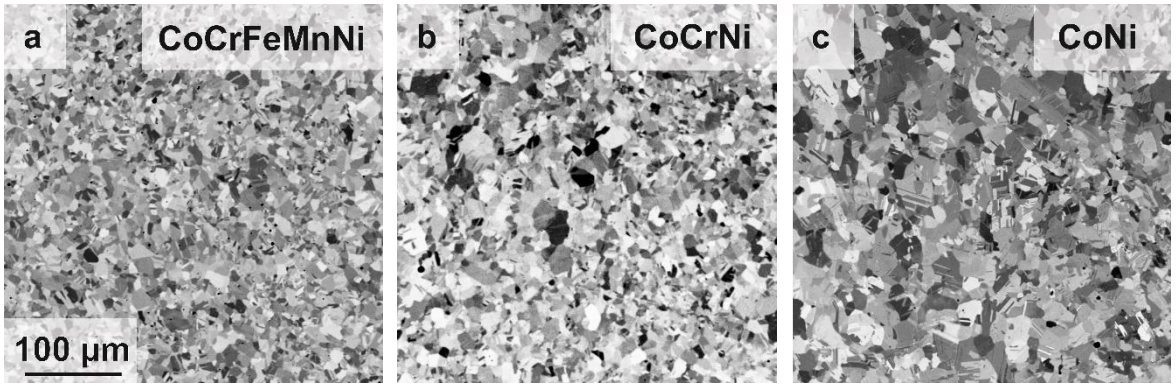

Figure 3.2: BSE images of (a) CoCrFeMnNi, (b) CoCrNi and (c) CoNi in the fully recrystallized state. The contrast is based on orientation since the chemical composition of the specimen is homogeneously distributed (section 3.2).

Color coded Inverse Pole Figure (IPF) Map reveals no distinctly visible texturing (Fig. 3.3). Rather, the texture was found to be near random, with weak components along ⟨111⟩ and ⟨001⟩ directions, but their effect is minimal. This mild texturing is the result of the rotary swaging processing step, seen in FCC alloys [42]. Nevertheless, the average Taylor factor is 3.05, which almost the same as completely random texture. The same processing sequence has been used in other mechanical studies for both CoCrFeMnNi [21] and CoCrNi [14].

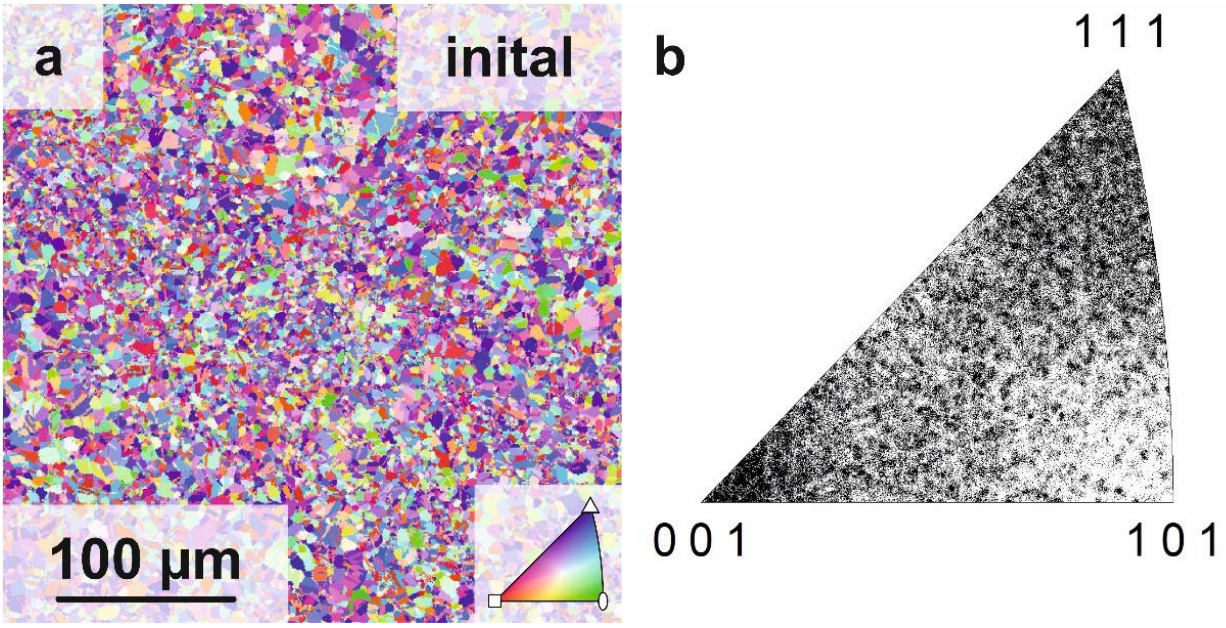

Figure 3.3: (a) EBSD based color coded IPF map corresponding (b) inverse pole figure triangles showing texture intensity. The specimen shows near random texture. The color coded legend is as given in inset on the bottom right. A pole figure map made for number intensity of the various orientation indexed on this image is shown on the top left.

3.2 Chemical homogeneity

Fig. 3.4 shows an example EDS area map for CoCrFeMnNi. The elemental distribution is homogeneous at the microscopic level. The uniform distribution of elements in CoCrFeMnNi, in nm range, was previously confirmed through Atom Probe Tomography (APT) [43].

While CoCrFeMnNi has been shown to exist as a single phase with uniform elemental distribution in the nm range, FCC phase decomposition has been previously achieved

through thermomechanical processing [44, 45]. The precipitates were Cr rich in nature. They were formed as a result of extended annealing treatments of 500 days at intermediate temperatures (500 - 700 °C). At both 900 and 1200 °C no precipitates were formed. This is in line with the current results considering that homogenization was carried out at 1200 °C, recrystallization at 800 °C (only for 1h). Also to be noted, the specimens were quenched after each heat treatment as opposed to being slow cooled, where they might spend a large amount of time at intermediate temperatures.

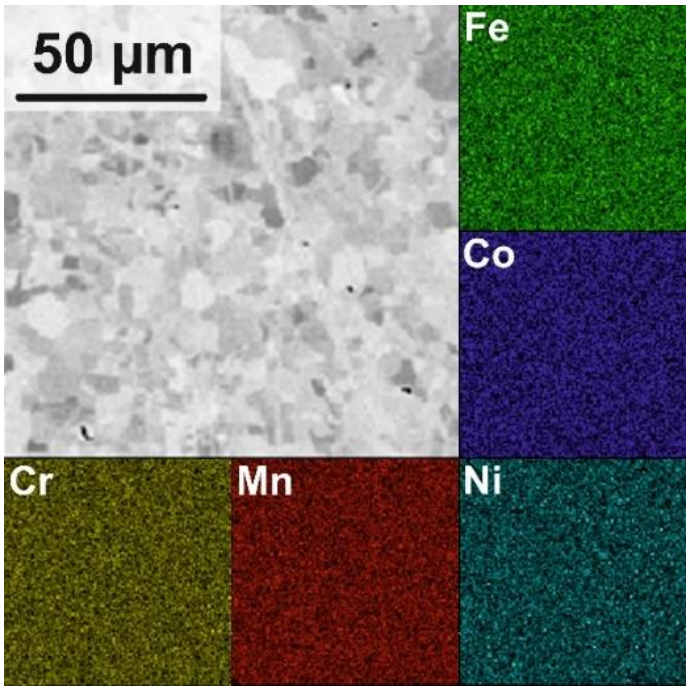

Figure 3.4: EDS map of CoCrFeMnNi specimen. Insets on the right hand side and bottom show the elemental concentration distribution of the constituent elements Fe, Co, Ni, Mn and Cr in the corresponding micrograph, given on the top left. There no discernable segregation or particle formation.

In contrast, CoCrNi has been thought to show Short Range Ordering (SRO) [46, 47]. However, there are significant issues with this consideration. Firstly, the proposed nature of the ordering in CoCrNi, changes depending on the method used to estimate it. Density Functional Theory (DFT) proposes distinct segregation of Cr [46] while Molecular Dynamics (MD) simulations predict that Cr-Cr and Co-Co clustering has the weakest intensity of all possible clustering pairs [47]. While SRO has been identified in CoCrNi [48], it is unclear which

elemental species have separated from the matrix and clustered. More importantly this was only achieved through long term annealing treatment at 1000 °C for 120 h, followed by slow cooling. The sample quenched from high temperatures (1200 °C) was used as a standard SRO free reference in the same report. All samples in the current work were subject to shorter annealing times and were quenched. Correspondingly, the CoCrNi specimens presently considered are devoid of SRO by any standard. It should also be noted that Yin et al. [49] , showed that the influence of SRO on mechanical properties is mostly imperceptible. Considering these factors, CoCrNi was not subject to any analysis along the lines of SRO. Further, it is noteworthy that Hong et al. [50] have claimed the presence of SRO in CoCrFeMnNi on the basis of activation volume estimates during deformation. However, unlike for CoCrNi there exists no additional proof, as evaluated by a characterization method. Moreover, Laplanche et al. [51] pointed out errors in the activation volume estimation in Ref. [50]. Ref. [51] made activation volume estimates that proved less counterintuitive and correspondingly eliminated the basis for the SRO in CoCrFeMnNi, as stated in Ref. [50].

Based on the given observations, in comparison with published literature, CoCrFeMnNi, CoCrNi and CoNi exist as fine grained polycrystalline specimens, in the single-phase FCC form.

4 Cryogenic deformation

Otto et al. [12] first showed an effective improvement in both strength and ductility of CoCrFeMnNi with decreasing temperature, down to 77 K. This was explained on the basis of active deformation mechanisms as a result of the prevalent stress state and temperature dependent SFE of the alloy [21]. As stated previously, low to medium SFE alloys ($13 - 49\, mJ \cdot m^{-2}$) revealed deformation twinning during RT deformation [24, 25, 26]. While this effect was seen down to temperatures of 77 K in CoCrFeMnNi, mechanical behavior and possible additional effects were not investigated at lower temperatures. Based on DFT calculations made in Ref. [28], an even greater change is expected in the deformation behavior of CoCrFeMnNi at lower temperatures, specifically due to change in SFE. Allain et al. [52] have stated that austenitic steels are expected to show mechanical ε-martensite transformation when the SFE of the material is less than $18\, mJ \cdot m^{-2}$. Kim and De Cooman [26] have shown ε-martensite formation in austenitic steel (Fe15Mn0.6C) of SFE $\sim 13\, mJ \cdot m^{-2}$. Ref. [28] predicts that SFE of CoCrFeMnNi will drop to less than $10\, mJ \cdot m^{-2}$ below 77 K, correspondingly being low enough to activate the TRIP effect under any consideration. In order to verify this, deformation behavior at near 0 K was investigated. Apart from this, to evaluate the effect of the deformation mechanisms at these temperatures their relative strengthening contributions were evaluated. In order to effectively do so, CoCrNi was used for comparison. This alloy has a higher RT yield strength (σ_{YS}) and lower equilibrium SFE, compared to CoCrFeMnNi [14]. Correspondingly, CoCrNi has been reported as showing ε-martensite formation at 77 K [27]. It should be noted that throughout the current work CoCrNi is considered to be a stable FCC alloy and not a metastable FCC alloy, that should exist in the HCP phase, as predicted by Niu et al. [53]. This is a valid assertion considering CoCrNi exists in the FCC crystal structure and shows no indication of the HCP phase in the fully recrystallized state, in the current work as well as former publications on the alloy [14, 27, 30, 31, 54]. Accordingly, equilibrium SFE here refers to the SFE of dissociated dislocations estimated from their width in the unstressed state. Furthermore, it has been asserted that the ε-martensite formed in CoCrNi contributes to its

strengthening and increases in proportion on decreasing the temperature further [27]. This claim is presently investigated.

CoCrNi has been seen as an improvement on CoCrFeMnNi, in terms of strength and ductility. The validity and possible reasons for this are investigated as well. Additionally, the origins of serrated plastic deformation, discussed in Sect. 5, cannot be appropriately analyzed without a sound understanding of the conventionally evaluated deformation characteristics. In order to fulfill all the above stated goals the current section covers a series of tensile tests carried out at room and cryogenic temperatures, followed by characterization studies. Most of the results in this section have previously been published and discussed in Refs. [29, 30], with the author of the thesis being the first author of the studies.

4.1 Solid solution strengthening

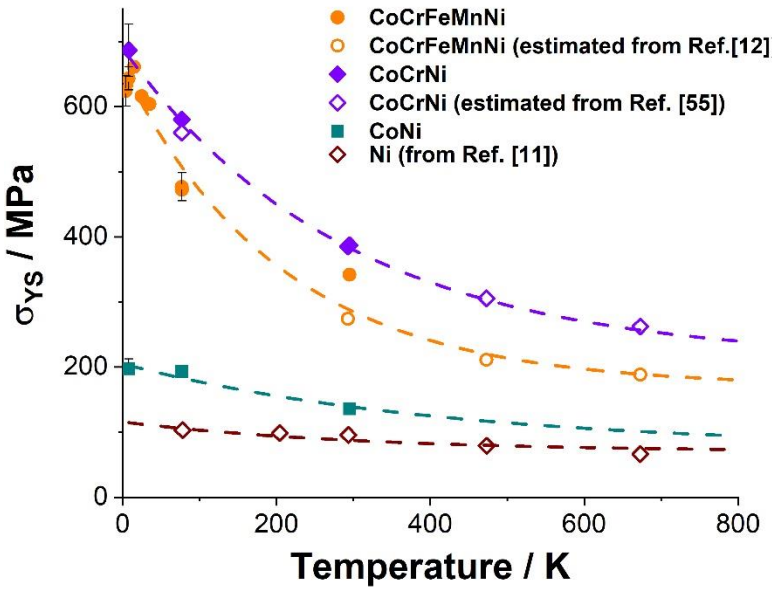

Figure 4.1: Plot of σ_{YS} of polycrystalline CoCrFeMnNi, CoCrNi, CoNi and Ni vs. temperature. Solid symbols represent experimental data from the present study, open symbols represent experimental results reported in the literature, which were either directly measured or estimated based on the HP relationships.

As a result of the tensile tests conducted at various temperatures σ_{YS} was determined for CoCrFeMnNi, CoCrNi and CoNi in the temperature range between 295 K and 4.2 K, depicted in Fig. 4.1. The serration behavior seen at very low temperatures was primarily studied

through CoCrFeMnNi (previously displayed in Fig. 1.1) and correspondingly significantly more tests were performed for this alloy at low temperatures. Tensile tests for CoCrNi and CoNi were performed only at RT, 77 K and 8 K. As stated in Sect. 3.1, the grain size for all three alloys were similar ($\sim 6 - 7$ µm). Apart from the experimental results obtained in the current research (marked by solid symbols), σ_{YS} at higher temperatures were calculated based on the Hall-Petch (HP) relations, as estimated by Otto et al. [12] for CoCrFeMnNi and Schneider et al. [55] for CoCrNi (marked by open symbols in Fig. 4.1). The data of Ni was added here as well [11], adjusted for a grain size of *7* µm, to illustrate the variation of stress with temperature in a pure FCC metal. The HP constants of Ni were only available at RT [56]. The value of k_{HP} was adjusted considering a linear variation of room temperature k_{HP} at the rate of $2 \cdot 10^{-4} \cdot (k_{HP}^{295})\ K^{-1}$. Fig. 4.2 depicts the $k_{HP} - T$ variation for both CoCrFeMnNi and CoCrNi as reported in Refs. [12, 55]. The straight line trend for CoCrNi ($2 \cdot 10^{-4} \cdot (k_{HP}^{295})\ K^{-1}$) was considered since like in Ref. [55], twin boundaries were presently considered to be HAGB. The curve in Fig. 4.1 is an approximate equivalent of Ni data at the given grain size.

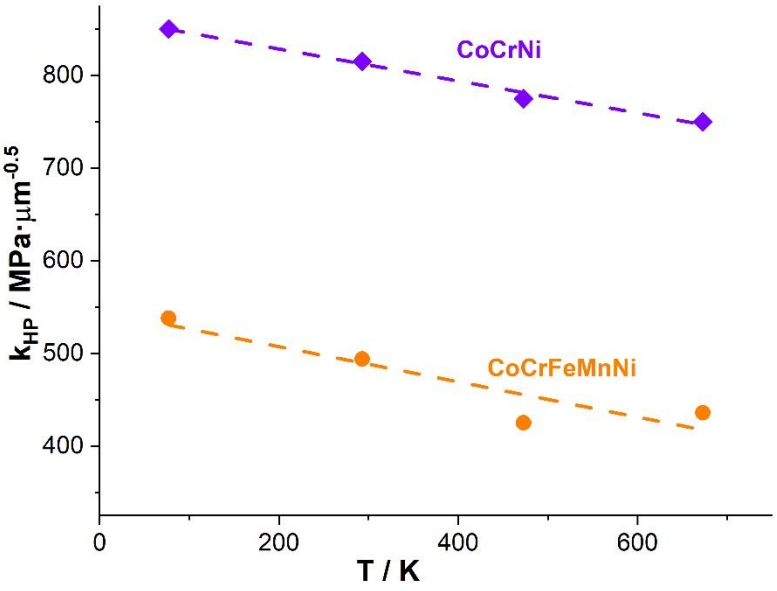

Figure 4.2: Plot of k_{HP} of polycrystalline CoCrFeMnNi and CoCrNi vs. temperature. The data was taken from Refs. [12, 55]. Both alloys exhibit a near linear trend.

The σ_{YS} variation with temperature appears quite steep in the case of both CoCrFeMnNi as well as CoCrNi. The trend is milder for CoNi and almost insignificant in the case of pure Ni.

The σ_{YS} ratio $\sigma_{YS}^{8K}/\sigma_{YS}^{295K}$ is ~ 1.3 for Ni, ~ 1.5 for CoNi, ~ 1.8 for CoCrNi and ~ 1.9 for CoCrFeMnNi. When considering all the contributing factors for strengthening at cryogenic temperatures in these alloys, particle strengthening and dislocation strengthening can be neglected. This is because, as shown in Sect. 3.1, the specimens being tested are single phase alloys in the fully recrystallized state. The grain boundary strengthening contribution at RT is clear, however when considering its variation with decreasing temperature, k_{HP} varies minimally in the given alloys (9% for CoCrFeMnNi [12] and 4% for CoCrNi [55] between 295 K and 77 K). So despite its prominent contribution to strength it doesn't contribute significantly to $\sigma_{YS} - T$ variation. Finally, the high solute content in the given alloys corresponds to significant solid solution strengthening. In combination with the Peierls stress, solid solution strengthening is not only a prominent strengthening contributor but also the one that changes significantly with decreasing temperature. Thus, a change in σ_{YS} with decreasing temperature is primarily an indicator of solid solution strengthening. This idea is borne out when considering the theory for solid solution strengthening in HEAs, elaborated below.

Solid solution strengthening in HEAs has been characterized by the Labusch type model [57, 58]. This is expected since HEAs have a high solute content [59]. In this model, the dislocation lines exist as pseudo-straight lines occupying energetically favorable atomic environments. On the application of sufficient stress, the dislocation lines slip across energetically unfavorable environments before once more settling at another favorable environment (Fig. 4.3). The solute pinning of dislocations in certain atomic environments is based on the local lattice distortion caused by the solutes. The Varvenne model of solid solution strengthening is based on the Labusch model, but makes evaluations for concentrated solid solutions in the absence of a principal matrix element [58]. It has provided an accurate calculation of strength for the equiatomic alloys of the Co–Cr–Fe–Mn–Ni system [58]. However, these estimates were made at RT. At cryogenic temperatures like 77 K, the predicted strengths were underestimations. A possible cause for this is the lack of consideration of Angstrom-level fluctuations in the calculations [58, 60]. At ambient temperatures (~295 K), the dislocation line shows minor deviations from a long straight line. These deviations are mesoscopic fluctuations that the dislocation line makes in order to

be accommodated in a favorable atomic environment. Angstrom level fluctuations refer to the pinning of the local portions of the dislocation line by solute atoms. These angstrom level fluctuations are not substantial and their contributions at RT are enveloped within the mesoscale calculations. However, they would generate additional energy barriers at lower temperatures and correspondingly become relevant at 77 K [58, 60].

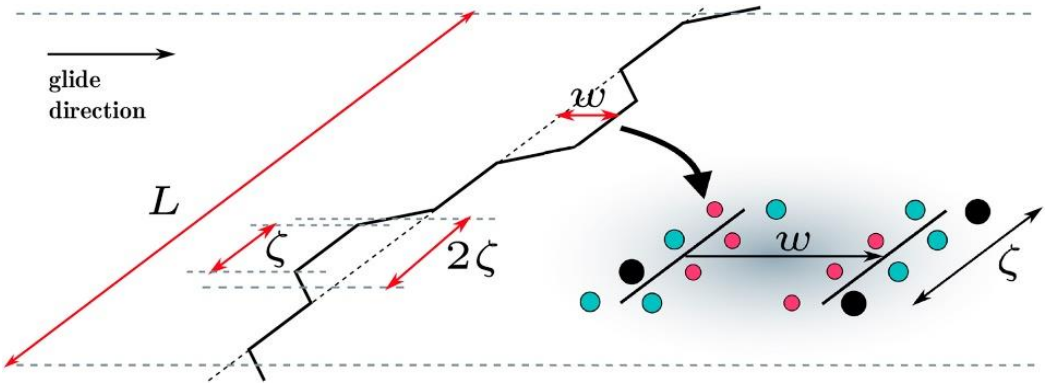

Figure 4.3: Dislocation glide from one favorable atomic environment to another. The dislocation is pinned at various sections by the local solute content. Figure taken from Ref. [58].

Based on the report of Owen et al. [61], at RT the static displacements of atoms (contributing to solid solution strengthening), is significantly mediated by the dynamic displacements (due to thermal contributions). Thus, under cryogenic conditions, as thermal contributions are minimized, the differences in atomic sizes have a clear effect on dislocation motion. The effect of this size difference is not *'damped'* like at higher temperatures. Accordingly, the static displacements of specific atoms or the solid solution strengthening effect would have a more pronounced effect on σ_{YS}. This increased effect of static displacement of atoms [61] leads to the importance of Angstrom-level fluctuations [58] at cryogenic temperatures. At these temperatures solute misfit/local lattice distortion effects are, thus, maximized and $\sigma_{YS} - T$ variation trends are a reflection of the level of solid solution strengthening.

The local lattice distortion in the Co–Cr–Fe–Mn–Ni system is reportedly the highest in the vicinity of Cr and Mn [58, 62, 63]. The high concentration of Cr in CoCrNi as well as Cr and Mn in CoCrFeMnNi validate this statement. CoNi comparatively exhibits a weak variation of strength with temperature. Co has a weak effect on the bond lengths in the alloy, and

correspondingly a low lattice distortion effect [62, 63]. The temperature dependent variation in σ_{YS} was given by the equation determined by Wu et al. [11]:

$$\sigma_{YS} = \sigma_a \cdot exp\left(\frac{-T}{C}\right) + \sigma_b \quad \text{Eq. 4.1}$$

Here $\sigma_{thermal}$ is the temperature dependent stress contribution, $\sigma_{athermal}$ is the temperature independent stress contribution and C is a constant. The derivative of the equation with respect to temperature is

$$\frac{d\sigma_{YS}}{dT} = -\sigma_{thermal} \cdot \left(-\frac{1}{C}\right) \cdot exp\left(\frac{-T}{C}\right) \quad \text{Eq. 4.2}$$

which can in turn be simplified as

$$\frac{d\sigma_{YS}}{dT} = -K_{const} \cdot exp(-T) \quad \text{Eq. 4.3}$$

K_{const} being the coefficient of the temperature dependent derivative of σ_{YS} with respect to temperature. Fig. 4.4 is a plot of lattice distortion as estimated by different methods as a function of K_{const} for the equiatomic single phase FCC alloys of this system as estimated from the data in Ref. [11].

Local lattice distortion in concentrated solid solutions has been measured as Atomic Size Difference (ASD) [58, 64] and Root Mean Square Atomic Distance ($MSAD^{0.5}$) [63]. ASD is given by the following equation:

$$\delta = \sqrt{\sum_i x_i \cdot \left(1 - \frac{r_i}{\bar{r}}\right)^2} \quad \text{Eq. 4.4}$$

Here x_i is the atomic concentration of element i with an atomic radius of r_i. This is calculated using radii extrapolated from the lattice parameter values of multiple binary alloy systems, as done in Ref. [58]. Alternatively, the radii may be calculated using an overdetermined set of alloys from the Co-Cr-Fe-Mn-Ni system, similar to the calculations made in Ref. [64]. $MSAD^{0.5}$ instead, is the root mean square of the distance by which atoms in a lattice are displaced from their ideal distortion-free position. MSAD values were listed by Okamoto et al., calculated from atomic radii estimated by ab initio calculations [63].

Fig. 4.4 indicates a positive correlation between the estimated lattice distortion and calculated temperature dependent slope K_{const} (Eq. 4.3) irrespective of the method of evaluation.

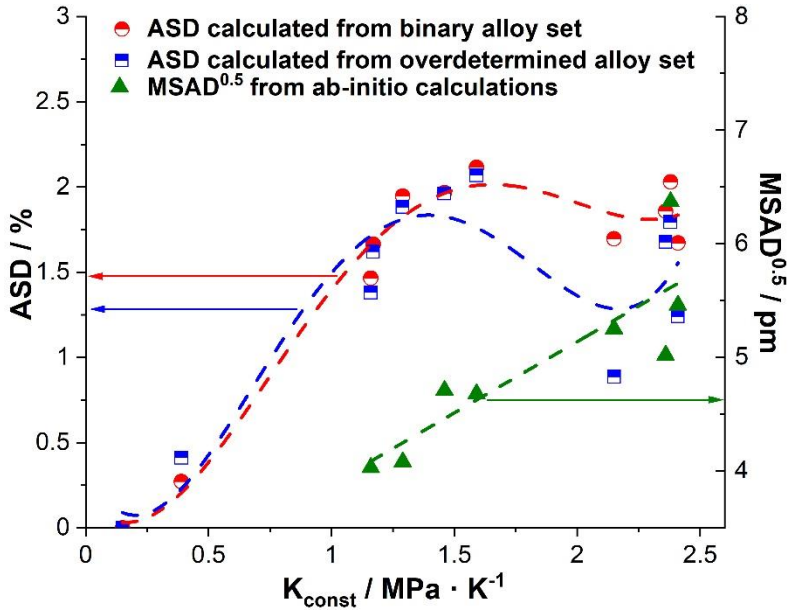

Figure 4.4: A plot of ASD and MSAD$^{0.5}$ as a function of coefficient of temperature dependent slope of $\sigma_{YS} - T$ variation, K_{const}. There is consistent positive trend for the different plots displayed. The dashed trend lines showing ASD variation (red and blue) are polynomial fits, while the dashed trend lines showing MSAD$^{0.5}$ variation (green) is a linear fit.

It should be noted that the radii used for ASD calculations are approximations of some order. The atomic radius of a metal within the alloy is expected to vary widely based on the local atomic environment [62, 63]. For this reason the quaternary and quinary alloys, seen at $K_{const} > 2$, show a deviation from the expected trend as well as scatter based on the method of ASD estimation. The ASD values in these alloys are not necessarily as accurate as in the case of binary and ternary alloys. In contrast, when considering MSAD, which was calculated based on ab initio estimations of atomic radii the data points follow a near-linear relationship, with the exception of one underestimation. Thus, $\sigma_{YS} - T$ acting as a reliable indicator for lattice distortion, shows that while CoCrNi has a higher σ_{YS} than CoCrFeMnNi the extent of solid solution strengthening is similar for both (comparing estimated ASD, MSAD and experimental K_{const}). It should be noted that Varvenne et al. [58] have also showed the similar values of σ_{YS} for CoCrNi and CoCrFeMnNi, estimated from the data of Ref. [10, 11], after subtracting grain boundary contribution to strength. Thus there is no

notably distinct advantage in terms solid solution strengthening for CoCrNi, despite the expectation based on previous reports [10, 11].

4.2 Deformation mechanisms

Post yield, the strength and ductility of an alloy is the result of active deformation mechanisms. These mechanisms are activated based on the flow stress, for an alloy of a given SFE. Presently, the effects of deformation twinning and ε-martensite formation on strength and ductility of CoCrFeMnNi are evaluated. CoCrNi was used as a partner alloy to appropriately correlate deformation mechanisms and their effects, since it shows additional deformation mechanisms. Thus, by comparing strengthening with different active deformation mechanisms the contribution of each of those to strengthening may be evaluated.

4.2.1 Deformation twinning

Before investigating cryogenic behavior of CoCrFeMnNi, the RT deformation was fully analyzed in tandem with CoCrNi. Fig. 4.5a shows the engineering stress-strain diagram for CoCrFeMnNi and CoCrNi. CoCrFeMnNi exhibits a uniform strain of ~30% while CoCrNi has a uniform strain of ~50%. Fig. 4.5b is a plot of the work-hardening rates of both alloys normalized by their respective shear moduli (G), determined in Refs. [65, 66, 67], as a function of $\frac{\sigma_t - \sigma_{YS}}{G}$ (σ_t and ε_t represent true stress and true strain, respectively). The abscissa term represents the extent of plastic deformation that has occurred, expressed as respective stress differences. Since dislocation interactions scale with G, it was used to normalize alloy-specific interactions. The abscissa was offset by respective σ_{YS} values to ensure an appropriate starting point when comparing different alloys. The work-hardening curves were reproduced for specimens from different batches to ensure consistency. During the initial deformation, up to $\frac{\sigma_t - \sigma_{YS}}{G} \approx 2 \cdot 10^{-3}$, the work-hardening rates were consistently similar for both CoCrFeMnNi and CoCrNi. Beyond this point, CoCrNi shows a change in the work-hardening rate, transforming to a gentler slope. The first part of the curve can be characterized by dislocation based deformation. The subsequent deflection in CoCrNi has been attributed to the activation of deformation twinning [14]. The presence of deformation

twins in CoCrNi, contrary to their absence in CoCrFeMnNi can be seen in BSE images of the specimens deformed to fracture (Fig. 4.6).

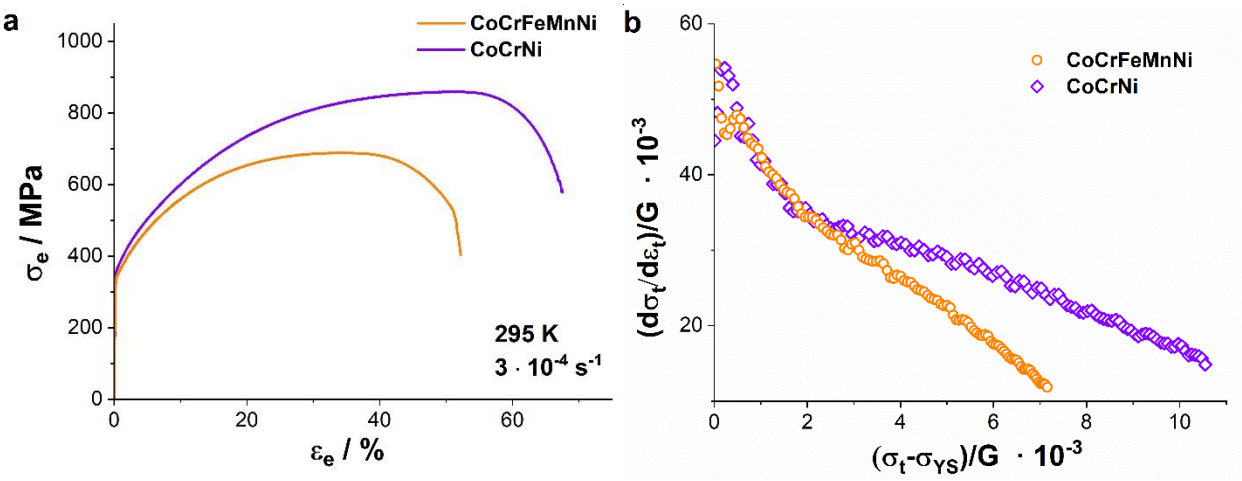

Figure 4.5: (a) $\sigma_e - \varepsilon_e$ plot for CoCrFeMnNi and CoCrNi at 295 K and the corresponding (b) plot of shear modulus normalized work-hardening, $\left(\frac{d\sigma_t}{d\varepsilon_t}\right)/G$, vs. extent of deformation, $\frac{\sigma_t-\sigma_{YS}}{G}$.

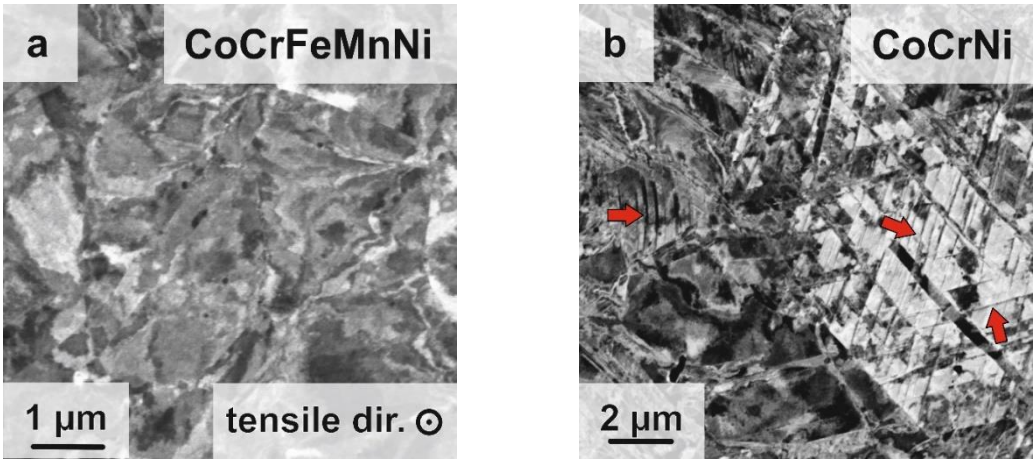

Figure 4.6: BSE orientation contrast images of (a) CoCrFeMnNi and (b) CoCrNi deformed at 295 K until fracture. Tensile direction (indicated in (a)) is the same for both micrographs and deformation twins are indicated by red arrows in (b).

While High Stacking Fault Energy (HSFE) alloys do not exhibit deformation twinning, alloys with medium to low SFE ($\gamma_{SFE} < 49\ mJ \cdot m^{-2}$) show deformation twinning, which increases

in propensity with lower SFE [25, 68]. This proceeds down to a $\gamma_{SFE} \sim 13\, mJ \cdot m^{-2}$, below which martensite transformation becomes active [26]. Despite CoCrFeMnNi having a room temperature $\gamma_{SFE} = 30\, mJ \cdot m^{-2}$, as measured by Okamoto et al. [69] deformation twinning was not prominent. Comparatively, CoCrNi with a measured $\gamma_{SFE} = 22\, mJ \cdot m^{-2}$ [14] does show substantial twinning.

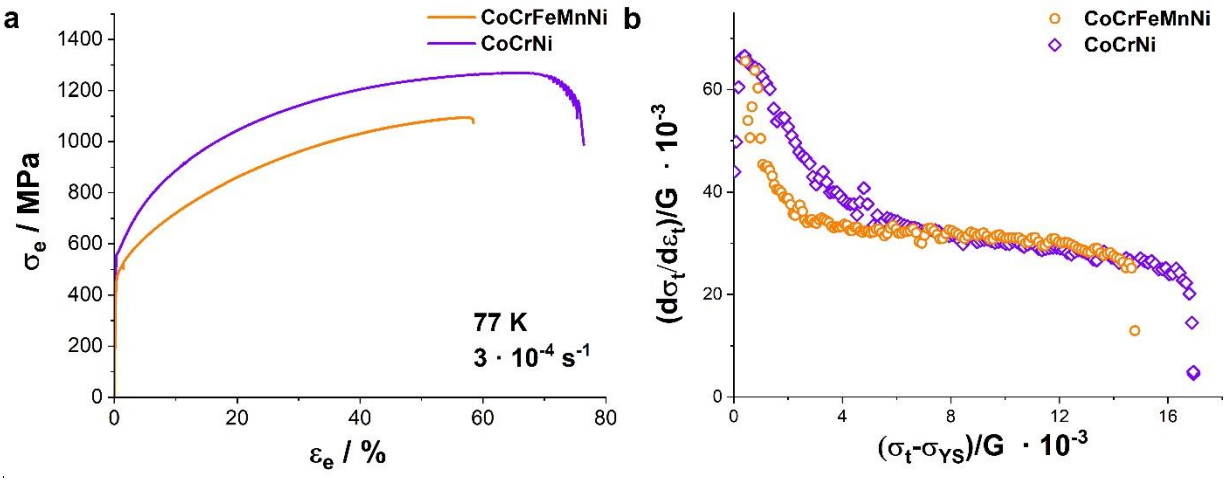

Figure 4.7: (a) $\sigma_e - \varepsilon_e$ plot for CoCrFeMnNi and CoCrNi at 77 K and (b) the corresponding plot of shear modulus normalized work-hardening $\left(\frac{d\sigma_t}{d\varepsilon_t}\right)/G$, vs. extent of deformation, $\frac{\sigma_t - \sigma_{YS}}{G}$.

For a given metal or alloy, SFE decreases with temperature. In combination with the increasing σ_{YS}, this would lead to the possible activation of deformation twinning in medium SFE alloys. This should be expected in CoCrFeMnNi, with the estimated SFE for CoCrFeMnNi in the range of a TWIP alloy at 77 K [28]. Fig. 4.7 depicts the engineering stress-strain plots for CoCrFeMnNi and CoCrNi at 77 K as well as the corresponding work-hardening rates. The plateau region in Fig. 4.7b depicts the plastic zone where deformation twinning is active. The synchronously active deformation mechanisms in both alloys result in significant overlap of the work-hardening rates. The increased work-hardening rate from deformation twinning

leads to significantly more uniform deformation prior to failure, since achieving Considère criterion[3] is further delayed [21].

The change in work-hardening rate due to deformation twinning has been attributed to dislocations being blocked by twin boundaries. While dislocations may interact with twin boundaries and in turn be transmitted through or glide along it [70, 71], they act as barriers to slip of certain orientations [72, 73]. Regardless of the nature of interaction, deformation twinning is associated with an increase in work-hardening rate [74]. Considering that in polycrystalline materials multiple slip systems are active, it is likely that multiple types of dislocation-twin interactions take place simultaneously. Among these interactions twin boundaries acting as dislocation barriers are the greatest contributor to work-hardening rate [75]. The corresponding effect is called the dynamic Hall-Petch effect, where twin boundaries result in strengthening analogous to other HAGB.

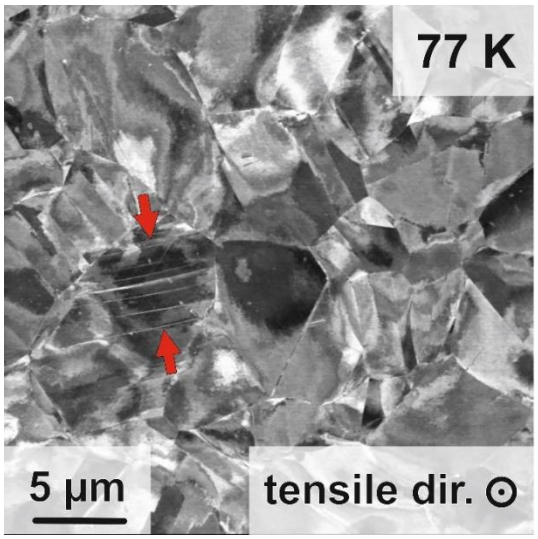

Figure 4.8: BSE orientation contrast images of CoCrFeMnNi deformed to $\sigma_t \sim 720\ MPa$, the twinning stress. Deformation twinning is observed only to a limited extent and thus, has just been initiated. A bundle of deformation twins is marked by two red arrows.

[3] Considère criterion is illustrated by the equation $\frac{d\sigma_t}{d\varepsilon_t} = \sigma_t$. This corresponds with the $\sigma_t$value beyond which necking takes place.

An interrupted tensile test was performed at the work-hardening rate deflection point ($\sigma_t \sim 720\ MPa$) and the corresponding BSE orientation contrast image (Fig. 4.8) shows minor deformation twinning, indicating that it has just begun. Twin initiation is thus linked to the change in work-hardening rate. Gutierrez-Urrutia and Raabe [76], proposed an equation to measure the relative strengthening contribution from deformation twins blocking dislocations as a part of the dynamic HP effect. The simple version of the equation is as follows:

$$\sigma = \sigma_0 + \frac{f_{twin} \cdot K_{HP}}{\sqrt{\lambda_{twin}}} \qquad \text{Eq. 4.4}$$

σ represents the strength, σ_0 is the strength in the absence of twinning, f_{twin} is the fraction of grains capable of twinning based on orientation, k_{HP} is the HP constant and λ_{twin} is the new crystallite size as a result of twinning. Consider the values $\sigma_0 = 475\ MPa$ (yield stress seen at 77 K for the given grain size), $f_{twin} = 0.375$ (the fraction of grains where twinning is favourable in the as recrystallized state was determined to be 0.375, as elaborated below), $k_{HP} = 538\ MPa \cdot \mu m^{0.5}$ (determined in Ref. [12]) and the grain size is considered to be 11 μm (grain size of the specimens tested currently, not considering annealing twin boundaries as grain boundaries). If we assume a single deformation twin is formed in each grain with favorable orientation, then σ jumps from $475\ MPa$ to $\sim 560\ MPa$.

During the test the occurrence of twinning is neither sudden nor is it instantaneously massive. All grains that have a favorable orientation do not instantly show twinning, and most grains that show twinning show multiple deformation twins as opposed to multiple grains showing single deformation twins. Based on the twin fraction and twin width estimations made in Ref. [21], the change in twin boundary length during deformation of CoCrFeMnNi at 77 K is shown in Fig. 4.9a. This change in length was expressed as fraction of all HAGB that were twin boundaries. Based on the data from Fig. 4.9a and Eq. 4.4, an estimate was made for the contribution of stress from twin boundaries shown in Fig. 4.9b, alongside the $\sigma_t - \varepsilon_t$ curve for CoCrFeMnNi deformed at 77 K [21]. The contribution was expressed as a function of the fraction of grains that underwent twinning. A greater fraction of grains undergoing twinning at any stage of deformation would result in a greater stress contribution and vice versa. The relative change in fraction of grains capable of twinning is elaborated in the following paragraphs. The calculations were based on the assumptions that

(i) the grains in the given specimen are hexagonal in shape, (ii) the twins are all of the same width with twin boundaries of a given twin parallel to each other and (iii) twin length far exceeds twin width. Thus while the plot undoubtedly indicates a strong contribution towards strengthening from deformation twinning, the value of stress is not necessarily reproducible. The considerations for the calculations made to illustrate Fig. 4.9a are elaborated in the Appendix. Based on Fig. 4.9 and the example calculation made above it is valid for deformation twinning to significantly impact mean free path of mobile dislocations despite being activated in a limited number of grains.

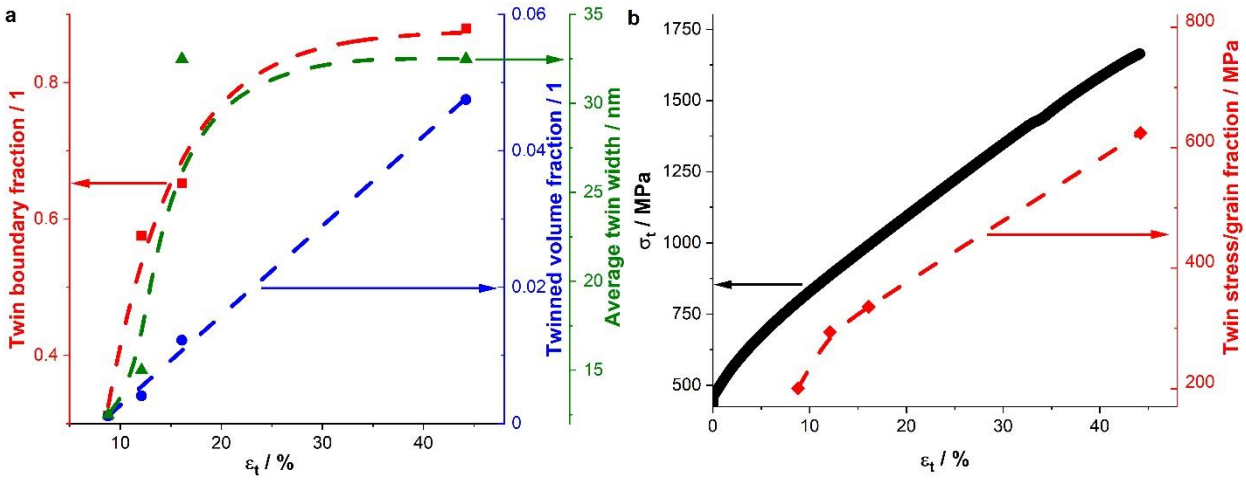

Figure 4.9: (a) Plot of twin boundary length as a fraction of total HAGB length, volume of twinned fraction and average width of deformation twins as a function of true strain. (b) $\sigma_t - \varepsilon_t$ plot of CoCrFeMnNi deformed at 77 K and the calculated stress contribution from twinning based on the increasing twin volume with ε_t. The twin volume fraction and average twin width were taken from Ref. [21]. They were used to calculate twin boundary length, shown in (a), which was subsequently used to estimate twin stress contribution in combination with Eq. 4.4. The stress contribution from twinning was expressed as a function of fraction of grains that exhibited twinning. The calculations were made for a square area of 1000 X 1000 μm side length. Further details of the considerations made to make these calculations are elaborated in the Appendix 11.1.

As deformation in uniaxial tension proceeds, the extent of twinning progressively increases. This is possibly linked to the texturing of the specimen. Under tension, deformation twinning

in FCC metals and alloys is possible only for certain orientations as illustrated in Fig. 4.10 [77, 78, 79, 80]. The twinning and non-twinning orientations are separated by a '*magic line*' terminated by the orientations [102] and [113]. This line represents the division between relative values of Schmid factors of the partial dislocations of an extended dislocation. The green portion of Fig. 4.10, represents slip plane orientations under tension for which the leading Shockley partial dislocation has a greater Schmid factor than that of the trailing partial [81]. It should be noted that this condition is in no way absolute and should only be taken as an indicator. Nevertheless, the empirical evidence from literature [77, 78, 79, 80] shows that for FCC metals and alloys tested under uniaxial tension, twinning does not take place in the red zone (Fig. 4.10).

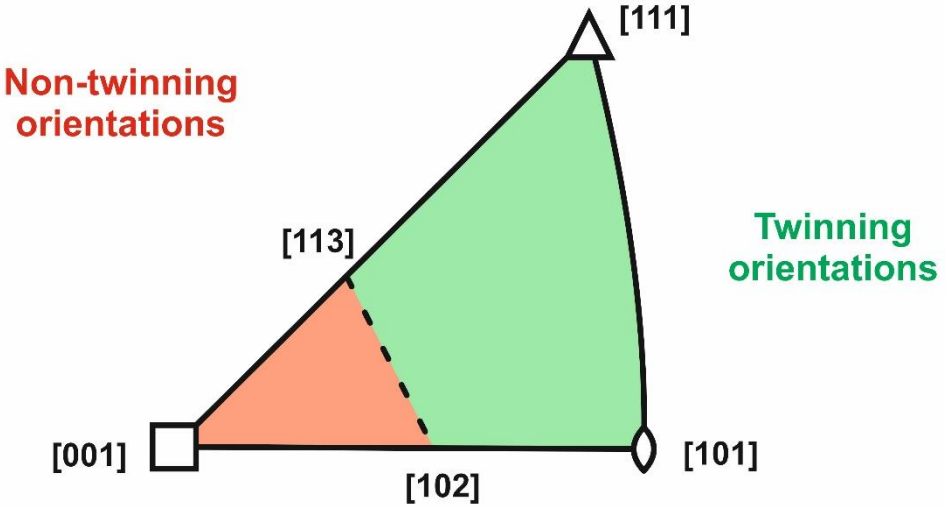

Figure 4.10: IPF triangle of the tensile axis showing orientations which are capable of twinning (in green) or not capable of twinning (in red) under tension. The two regions are separated by a '*magic line*' connecting the orientations [113] and [102], [77, 78, 79, 80].

As deformation proceeds, grains with ⟨001⟩ and especially ⟨111⟩ directions parallel to the loading axis increase in proportion, as is expected in polycrystalline FCC alloy undergoing uniaxial tensile strain [82, 83, 84]. This is illustrated in Fig. 4.11c where the progressive strengthening of these orientations with deformation is measured in terms of Taylor factor

(*M*) (the interrupted tests have total strains corresponding to deflection of the work-hardening curve and middle of the work-hardening plateau, depicted in Figs. 4.11a and b).

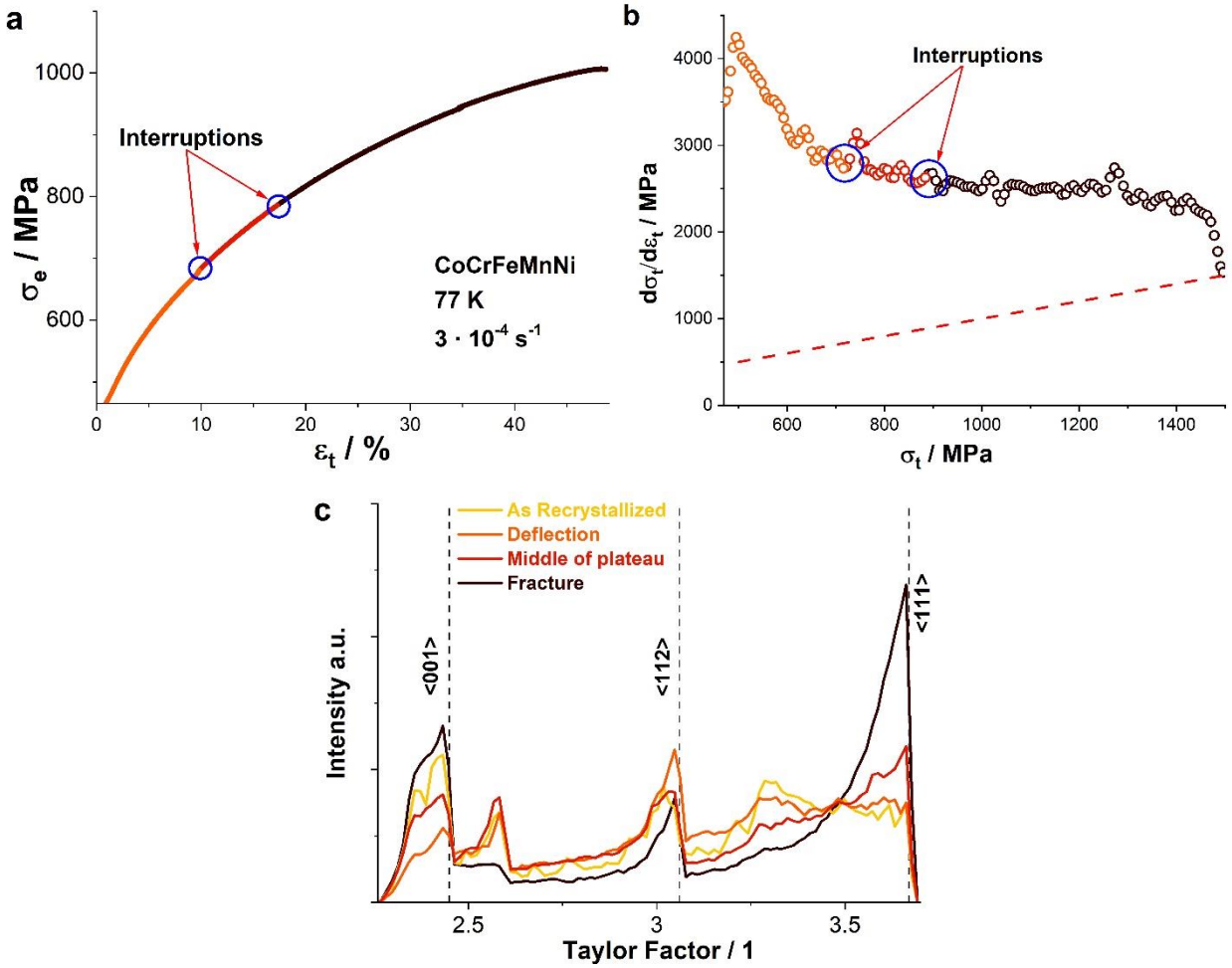

Figure 4.11: (a) Plastic region of $\sigma_e - \varepsilon_e$ plot for CoCrFeMnNi deformed at 77 K. The different colors represent different specimens interrupted at different stages in deformation. The interruption is marked by blue circles. (b) Corresponding plot of $\frac{d\sigma_e}{d\varepsilon_e} - \sigma_e$, with the different stages of deformation marked. The dashed red line represents the Considère criterion. (c) The Taylor factor distribution for each of the specimens, with ⟨001⟩, ⟨112⟩ and ⟨111⟩ indicated by dotted lines.

Fig. 4.11c was determined by performing an EBSD scan on each of the deformed specimens indicated in Figs. 4.11a and b, as well as the recrystallized condition. Using the orientation specific microstructural data, the Taylor factor distribution of all grains was calculated. Apart

from the strong ⟨111⟩ and ⟨001⟩ orientations parallel to the loading direction at fracture, the ⟨112⟩ orientation became significant at intermediate stages.

During deformation of grains, that are constrained by not allowing free lateral movement of instrument cross heads, the dislocation activity results in grain rotation. During uniaxial tensile deformation of an FCC crystal the rotations tend towards either the ⟨111⟩ or ⟨001⟩ orientation depending on the original orientation [85]. Grains of several orientations (closer to the $\langle 111\rangle - \langle 011\rangle$ orientations), that tend to the ⟨111⟩ orientation first rotate to an orientation along the line connecting the ⟨001⟩ and ⟨111⟩ orientation in the IPF triangle. They then progressively move towards the ⟨111⟩ orientation. Since the grain rotation takes place sequentially towards ⟨111⟩ and not directly in a straight line path, there is an intermediate strengthening of texture on the $\langle 001\rangle - \langle 111\rangle$ line, specifically seen for the ⟨112⟩ orientation in the current case.

The average maximum Schmid factor and Taylor factor for slip (slip system $\{1\bar{1}1\}[\langle\bar{1}01\rangle]$) changes minimally as deformation proceeds (Fig. 4.12a). Additionally, the proportion of twinning orientation (shown in the green zone in Fig. 4.10) does not change significantly with deformation (Fig. 4.12b). It remains at ~70% throughout deformation.

This implies that as deformation proceeds twin activity increases [21] even though (i) slip is not made more difficult by texturing towards orientations of lower Schmid factors and (ii) there is no texturing towards favorable twinning orientations. If only the grains with the orientations that most easily show deformation twinning are considered, instead of considering all orientations where twinning is possible (green zone in Fig. 4.10), it may illustrate why there is a progressive increase in grains that undergo twinning. Based on this argument twinning is progressively seen in more grains as the number of grains where dislocation slip stress is at least as high as twinning stress increases. To this end, Figs. 4.13a and b show Inverse Pole Figure (IPF) maps, illustrating the Schmid factor for the slip systems of type $\{1\bar{1}1\}[\langle\bar{1}01\rangle]$, $\{1\bar{1}1\}\langle\bar{2}\bar{1}1\rangle$ and their ratio as well (Fig. 4.13c).

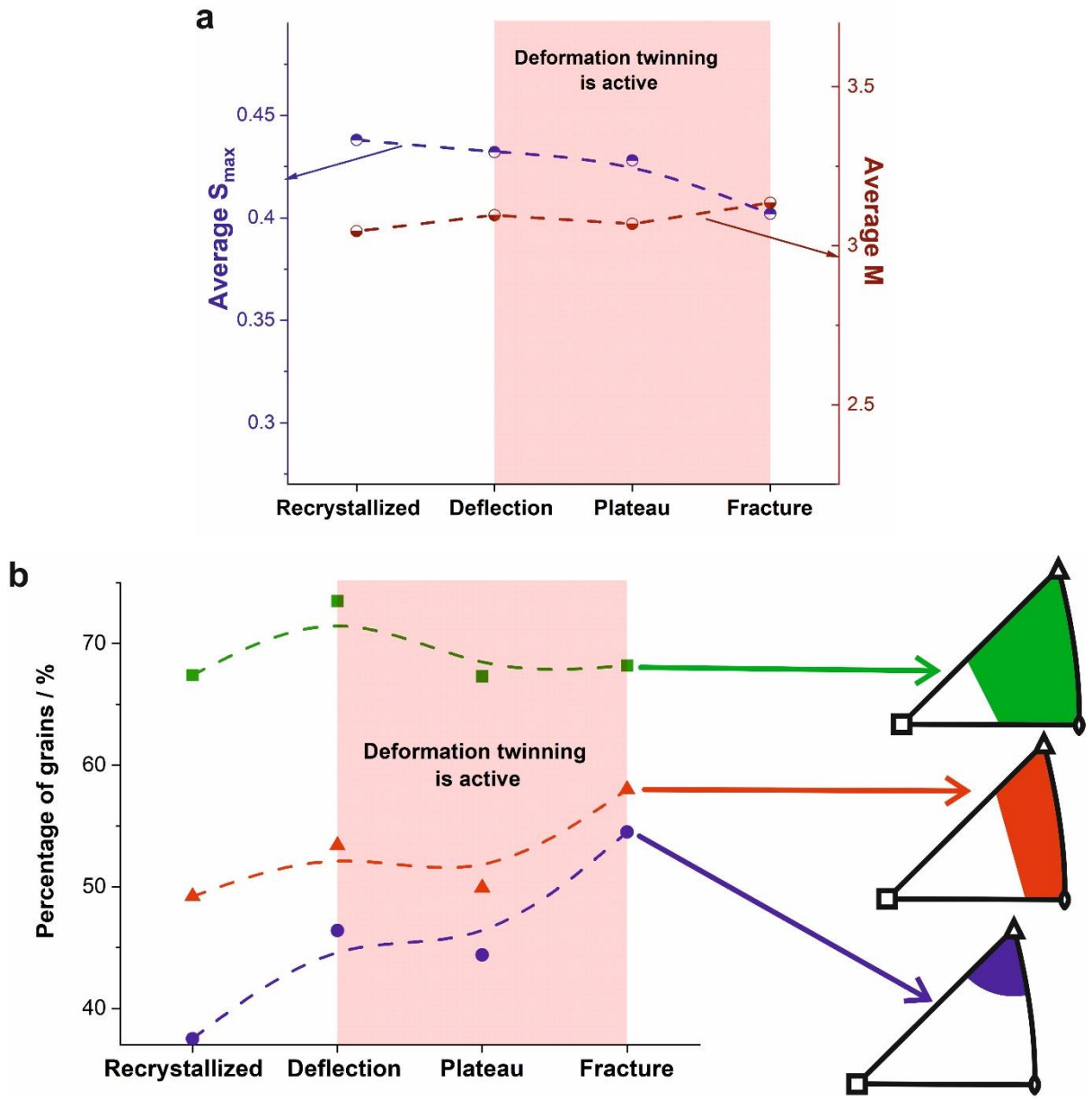

Figure 4.12: (a) The average maximum Schmid factor, m_{max} (in dark blue), and average Taylor Factor, M (in dark red), as estimated by EBSD at different stages of deformation. The ordinate axis in each case has been adjusted to show the full range of possible values of m_{max} and M for any given orientation. (b) The variation in fraction of grains that have orientations corresponding to twin zone in green (as shown in Fig. 4.10), to '*hot zone*' in red (shown in Fig. 4.13c as region with $\frac{m_{twin}}{m_{slip}} \geq 1$) and the region around ⟨111⟩ (within a 20° tolerance) depicted in blue.

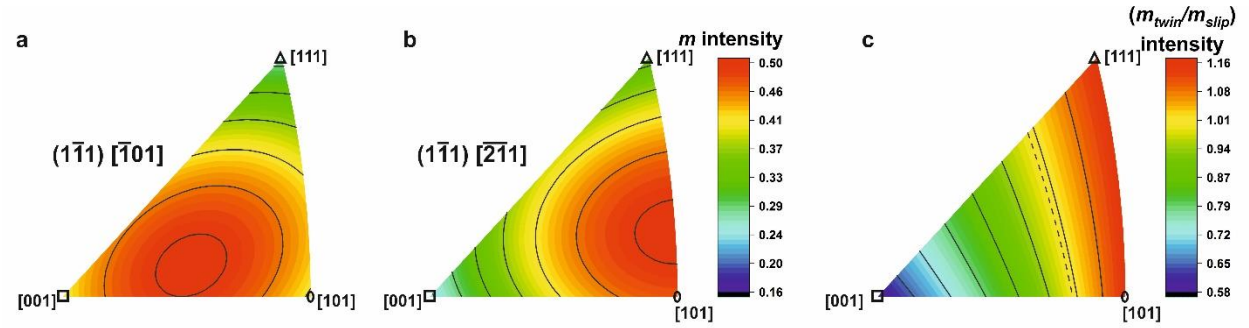

Figure 4.13: IPF maps showing Schmid factor calculated for tensile axis parallel to a direction within the standard triangle for the slip system (a) $(1\bar{1}1)[\bar{1}01]$, (b) $(1\bar{1}1)[\bar{2}\bar{1}1]$, (c) Ratio of $(1\bar{1}1)[\bar{2}\bar{1}1]$: $(1\bar{1}1)[\bar{1}01]$, (twin:slip). The dashed line in (c) is the contour line for Schmid factor ratio = 1. Schmid factor intensity legend for $(1\bar{1}1)[\bar{1}01]$ and $(1\bar{1}1)[\bar{2}\bar{1}1]$ is the same as shown in (b). The intensity legend for the ratio of Schmid factors is as displayed in (c).

Fig. 4.13a represents the Schmid factor distribution for motion of a full dislocation while Fig. 4.13b represents the Schmid factor distribution for deformation twinning considering the Venables pole mechanism [86]. According to this mechanism the jogged portion of a forest dislocation forms a stacking fault by splitting into a glissile Shockley partial, of $\vec{b} = \frac{1}{6}[\bar{2}\bar{1}1]$,while being anchored by a sessile Frank partial, of $\vec{b} = \frac{1}{3}[1\bar{1}1]$. The sessile partial is of screw nature and in turn causes a screw like deformation in the glide plane of the dislocation of $\vec{b} = \frac{1}{6}[\bar{2}\bar{1}1]$. A glissile dislocation when anchored at a point would glide circularly (like a Frank-Reed source) but due to the screw natured deformation caused by the sessile dislocation, it instead forms a spiral. This spiral extends layer on layer resulting in an intrinsic stacking fault in each atomic layer, thus forming the deformation twin. In light of this mechanism the principle stress to form a twin relates to the stress required to enable glide for dislocations of type $\vec{b} = \frac{1}{6}[\bar{2}\bar{1}1]$ as it is the only mobile dislocation in the pair.

Fig. 4.13c shows an IPF of the ratio of Schmid factors for twin over slip $\left(\frac{m_{twin}}{m_{slip}}\right)$. The most favorable region for deformation twinning in the map is to the right of the dotted line, which represents $\frac{m_{twin}}{m_{slip}} = 1$. This zone will be referred to as the *'hot zone'*. As deformation proceeds in CoCrFeMnNi, within the hot zone (i) there is practically no texturing towards ⟨101⟩,

(ii) maximum texturing occurs towards ⟨111⟩ and (iii) the least favorable orientation for dislocation slip as estimated by the Schmid factor, is ⟨111⟩ (Fig. 4.13a).

Fig. 4.12b shows that as deformation proceeds of the number of grains with the orientation within the 'hot zone' increases. However, a more significant strengthening of the ⟨111⟩ texture was seen during the same. As these orientations in the vicinity of ⟨111⟩ progressively increase, greater deformation twinning is justified. The number of grains with orientations in the vicinity of ⟨111⟩ increases by ~ 50 % over the course of deformation. It should be noted that the deviation from ⟨111⟩ considered here is 20°, since beyond this angle $\frac{m_{twin}}{m_{slip}} \leq 1$. The combination of increasing stress and favorable texturing under tension, as deformation proceeds, explains the severe twin activity seen in CoCrFeMnNi at 77 K.

4.2.2 ε-martensite formation

As explained in previously in this chapter, the activation of TRIP in CoCrFeMnNi at lower temperatures was a significant point of interest. While TWIP, characteristic of low to medium SFE alloys, shows improvement in work-hardening rate, resulting in (i) higher strength and (ii) greater elongation prior to failure, an even more pronounced effect may be expected from TRIP. TRIP steels show significantly greater change in work-hardening rates when compared to TWIP steels and correspondingly an even better combination of mechanical properties [87]. TRIP is seen in LSFE materials with $\gamma_{SFE} < 13\ mJ \cdot m^{-2}$ [26]. Based on the estimates of Huang et al. [28], CoCrFeMnNi should show TRIP activity at close to 0 K. To this end, a tensile test was conducted on CoCrFeMnNi at 4.2 K, in a liquid Helium bath. The microstructure of the specimen deformed at multiple temperatures along with the initial recrystallized condition was shown in Fig. 4.14. The texturing at 4.2 K is similar to that seen at higher temperatures and additionally shows significant twinning. However, no martensite phase could be reasonably indexed. It should be noted that the martensite in reference here and for the remainder of the chapter is HCP ε-martensite.

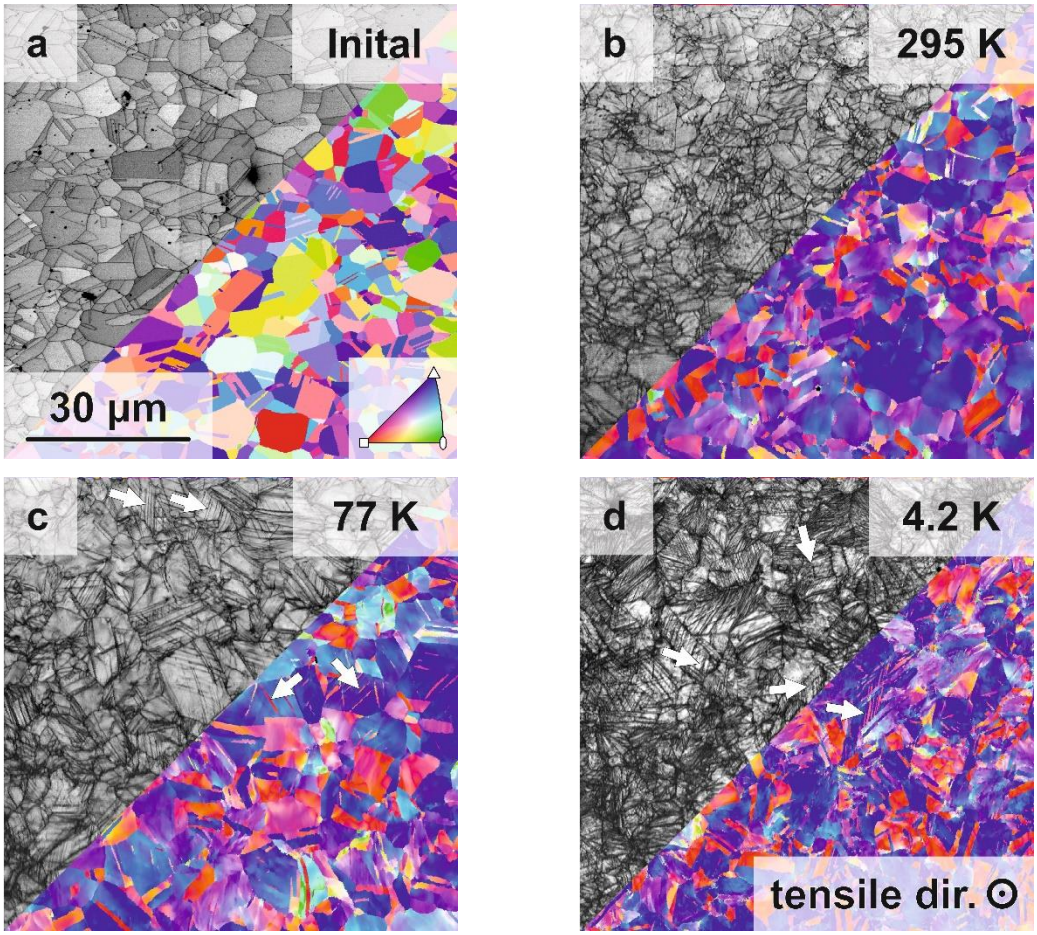

Figure 4.14: Orientation imaging microscopy: the top left shows a gray scale image quality map and the bottom right shows the colored orientation map of (a) the recrystallized initial state; specimen deformed to fracture at (b) RT (295 K), (c) 77 K and (d) 4.2 K. All micrographs have the same magnification and specimen orientation with respect to the loading axis. Some of the deformation twins are marked by white arrows.

Additionally, the STEM-HAADF and corresponding SAD pattern for the specimen deformed at 4.2 K illustrates only a matrix FCC phase and corresponding twin (Fig. 4.15).

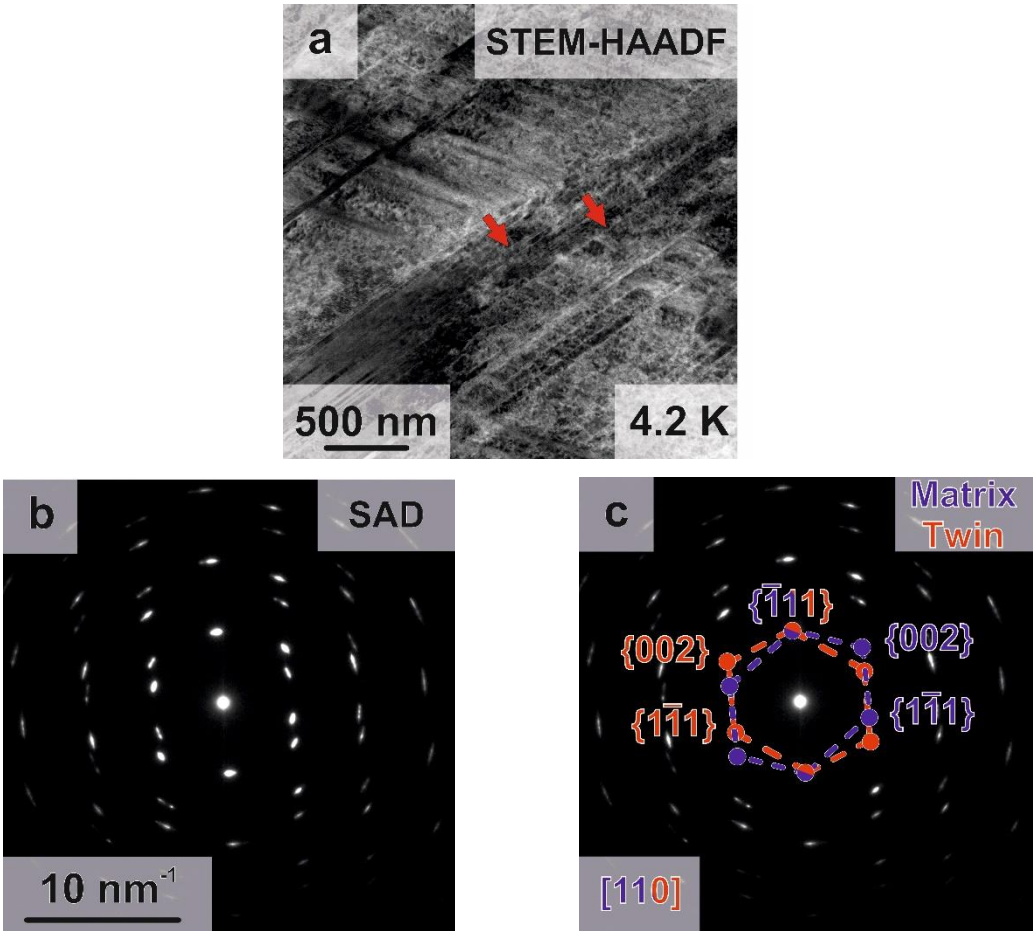

Figure 4.15: TEM analysis of CoCrFeMnNi deformed at 4.2 K: (a) BF image of the selected area with deformation twins indicated by red arrows, (b) corresponding TEM- SAD pattern, (c) TEM-SAD pattern with indexed FCC matrix (blue) and twin (red). The zone axis is indicated at the bottom left.

The absence of the predicted ε-martensite can be reasoned in the following ways:

i. It is possible that ε-martensite has recovered during the heat up following the cryogenic test. However, considering that the phase in discussion was athermally formed during cryogenic deformation, complete recovery of strain induced phase transformation in this temperature range is unrealistic. This line of reasoning may also be extended to possible recovery during the TEM-sample preparation vis-à-vis FIB lift-out.[4]

[4] Later in the current section, TEM analysis of CoCrNi revealed nm thick layers of ε-martensite which were indexed in the SAD pattern. This was despite the heat up from 8 K to RT as well as specimen preparation for the TEM. Thus when martensite is formed during deformation it is not removed during the specimen preparation phase.

ii. Under certain circumstances, in some regions the stacking sequence can resemble a HCP phase (ε-martensite). In these regions every alternate layer of the close packed plane in an FCC crystal has an intrinsic stacking fault. This changes the stacking sequence from A-B-C-A-B-C (FCC) to A-B-A-B-A-B (HCP). However, these compact aggregates are only a few atomic layers in thickness and are a statistical result. They are not a consequence of a nucleation and growth sequence as seen in TRIP steels [88] or even other alloys in the CoCrFeMnNi system [53, 89]. As such, they cannot be identified by EBSD and are not classified herewith as ε-martensite.

iii. The DFT calculations made by Huang et al. [28] correlate the SFE directly with the estimated difference in free energies of the HCP phase to the FCC phase and correspondingly predict ε-martensite formation at 4.2 K. This is in contrast to Olson and Cohen [88], who additionally accounted for strain energy from the new phase as well as the energy cost of the interphase surfaces. The implication, in turn, is that the estimated free energy difference must be offset appropriately to correctly estimate SFE.

iv. SFE estimations in Ref. [28] may have overestimated the temperature dependence of chemical contributions to the change in SFE. This would lead to a significantly lower predicted SFE.

In contrast to CoCrFeMnNi, CoCrNi shows the formation of ε-martensite during deformation. While it was reported to only be a 3 layer A-B-A sequence at RT, a noticeable nano-aggregate was found at 77 K [27]. The aggregates were substantial enough to be indexed as a HCP phase using TEM-SAD. Miao et al. [27] asserted that the formation of this new phase (i) would increase with decreasing temperature and (ii) would increase the work-hardening rate and in turn strength of the alloy. Both of these hypotheses are presently tested in the upcoming pages.

First to verify the ε-martensite presence CoCrNi at cryogenic temperature, a tensile test was carried out on CoCrNi at 8 K. The microstructure of the fractured specimen indicated a clear presence of deformation twins (Fig. 4.16a). Additionally, the TEM-SAD pattern illustrates a matrix FCC phase and twin as well as a HCP ε-martensite phase (Fig. 4.16c and d). The orientation relationships are as follows: $(0002)_{\mathrm{HCP}} \,||\, (\bar{1}11)_{\mathrm{FCC}}$ and

$[2\bar{1}\bar{1}0]_{\mathrm{HCP}} \,||\, [110]_{\mathrm{FCC}}$ and the lattice parameters of the ε-martensite was estimated to be $c = 4.11$ Å, $a = 2.56$ Å. The results are in line with previous observations of Miao et al. [27].

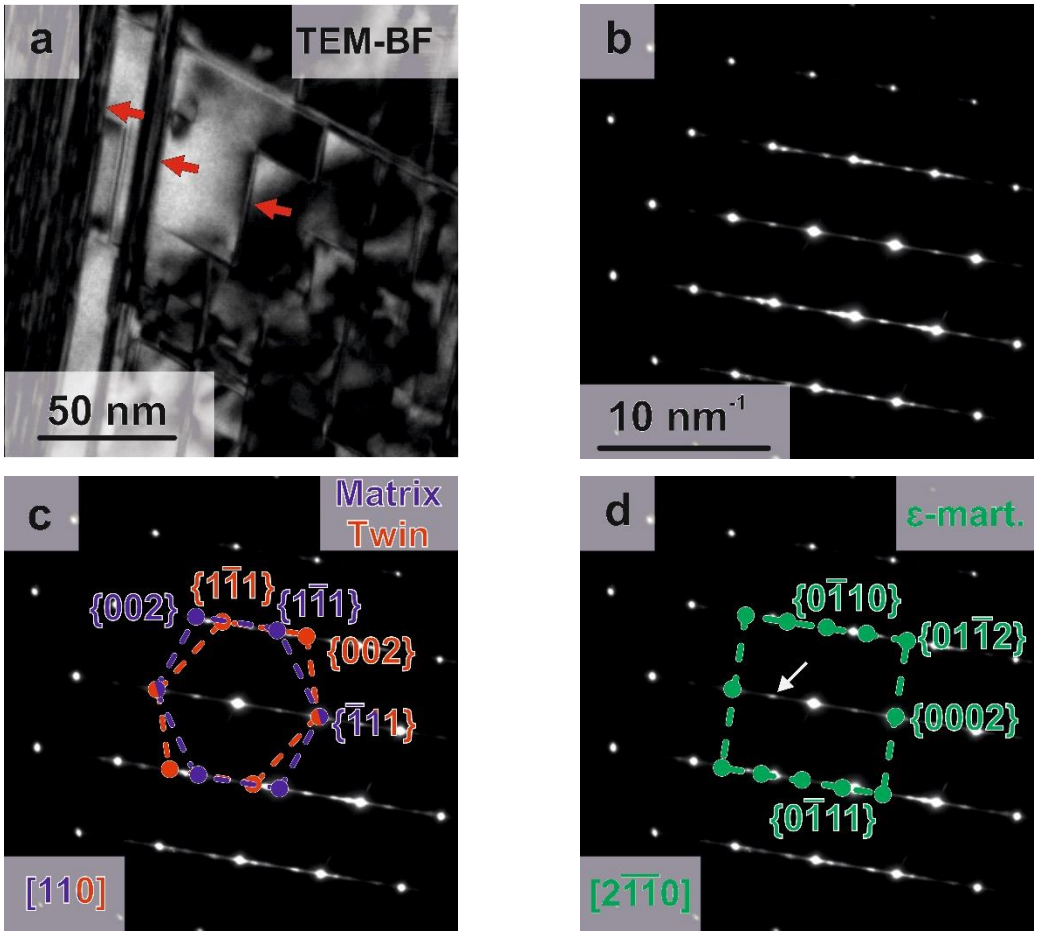

Figure 4.16: TEM analysis of CoCrNi deformed at 8 K: (a) BF image of the selected area with deformation twins indicated by red arrows, (b) corresponding TEM- SAD pattern, (c) TEM-SAD pattern with indexed FCC matrix (blue) and twin (red) and (d) TEM-SAD pattern with indexed ε-martensite (green). The zone axes in each case are illustrated at the bottom left of figures (c) and (d). The diffraction spot highlighted with a white arrow in (d) is a forbidden reflection of type {0001}, which becomes visible due to a double diffraction.

Fig. 4.17 shows TEM-BF image and false color maps DF images corresponding to specific twin and ε-martensite diffraction peaks. The corresponding peaks have been specified in the

insets (Fig. 4.17c). ε-martensite is found overlapping with practically all twins (Fig. 4.17b). This may be explained by the method of ε-martensite nucleation and growth in CoCrNi.

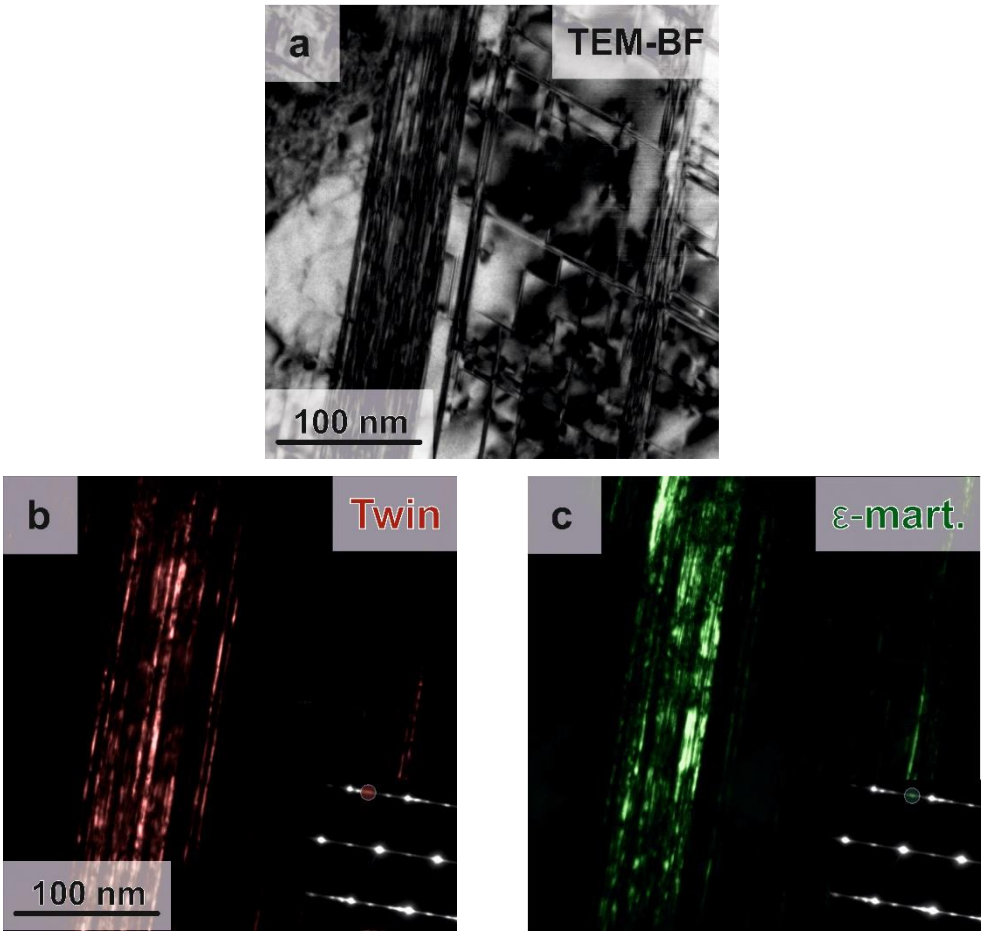

Figure 4.17: (a) TEM-BF image of CoCrNi deformed at 8 K. Corresponding colored TEM-DF images showing (b) deformation twins (red), acquired using $(1\bar{1}1)_{\text{twin}}$ diffraction spot and (c) ε-martensite (green) acquired using $(0\bar{1}10)_{\varepsilon-\text{mart.}}$. The diffraction patterns are as shown in the inset.

According to Niu et al. [53], dissociated near edge dislocations (60°) have the leading partial dislocations interact with the twin boundary. During this interaction, the partial dislocation will glide along the twin boundary, leaving behind a sessile dislocation. In turn, the stacking sequence at the twin boundary changes to that of a HCP lattice structure. Subsequent dislocations react with this interface and add additional atomic layers, thus building a HCP aggregate.

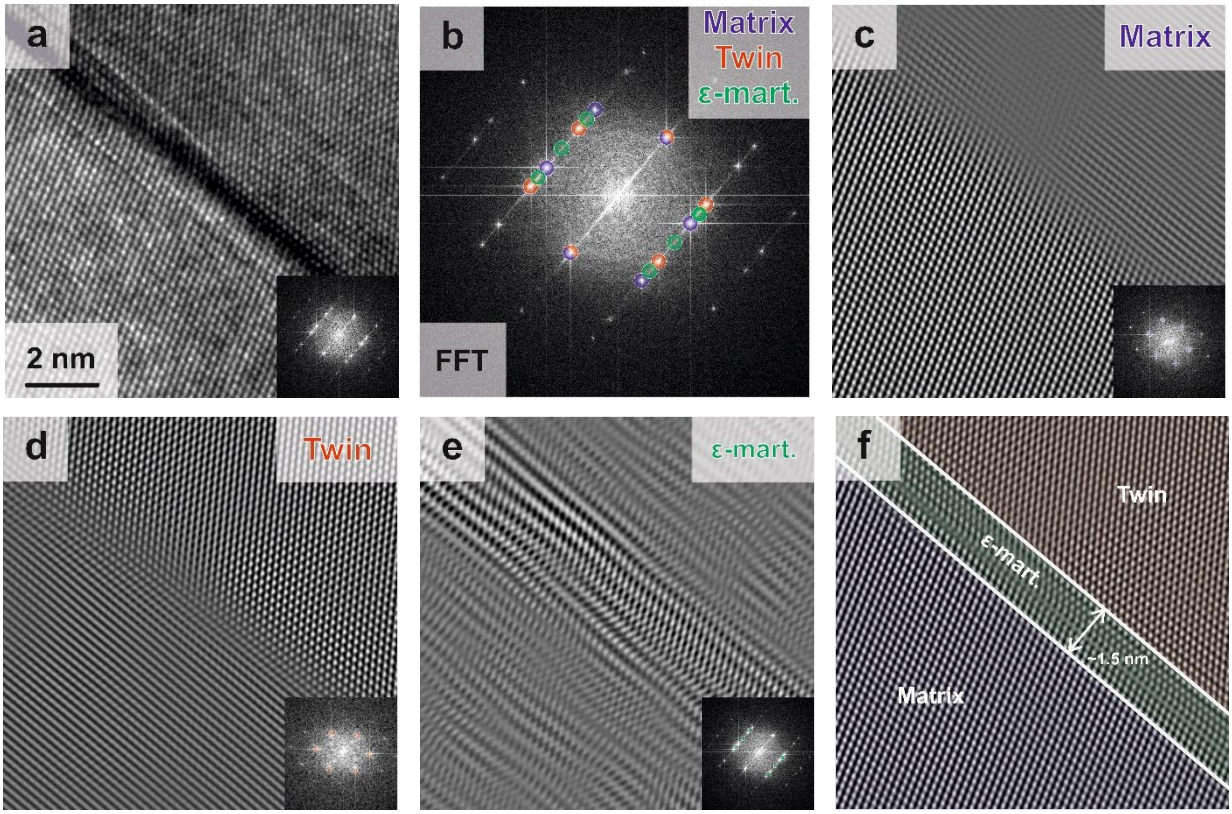

Figure 4.18: (a) High-resolution TEM image of CoCrNi tested in tension at 8 K, (b) FFT for the high-resolution image. Spots of the matrix and twin were identified with blue and red circles. The points where ε-martensite was expected (based on TEM-SAD pattern Fig. 4.16) were marked with green circles, (c) image constructed with a mask applied to the matrix spots; the bottom left of the image is in focus, (d) image constructed with a mask applied to the twin spots; the top right of the image is in focus, (e) image constructed with a mask applied to the expected spots for ε-martensite in the FFT; parts of the diagonal region from top left to bottom right appear to be in focus, (f) composite of all three regions, showing matrix and twin separated by a ε-martensite plate which is approximately 1.5 nm thick. Images (a), (c), (d) and (e) all have insets of corresponding FFT/iFFT.

Fig. 4.18a depicts a high-resolution TEM image where three different regions can be distinguished based on contrast and symmetry. The FFT, Fig. 4.18b, reveals the FCC phase, twin and ε-martensite. Masks were applied to focus on each of these features. (i) The spots circled in blue in Fig. 4.18b belong to the matrix and atomic columns appear sharp at the bottom left of the iFFT shown in Fig. 4.18c while the remainder of the image appears blurred.

(ii) The mask applied to spots belonging to the deformation twin (see red circles in Fig. 4.18b), shows an iFFT (Fig. 4.18d) of the twinned region located at the upper right corner of the image. (iii) Finally, when a mask is applied on the spots which belong to ε-martensite (see green circles in Fig. 4.18b) a thin ~ 1.5 nm thick layer appearing diagonally from the top left to the bottom right of Fig. 4.18e appears in sharp. A color-coded summary is depicted in Fig. 4.18f.

Based on Figs. 4.17 and 4.18 it is clear that (i) ε-martensite is formed at twin boundaries and (ii) appears as nano-layers sandwiched between the matrix and the twinned regions. This is in line with the Niu et al. model of martensite nucleation and growth [53].

Contrary to the report of Miao et al. [27], the ε-martensite was of a reportedly similar size for deformation at 8 K as compared with 77 K (seen in Ref. [27]). The volume of martensite aggregates did not show a jump at lower temperatures. There are three possible reasons for this:

i. The first relates to the discontinuous deformation seen at such low temperatures. Fig. 4.19a shows the engineering stress strain curves for CoCrFeMnNi and CoCrNi deformed at 8 K. They both show severely discontinuous deformation. It is possible that due to the localized nature of deformation, the engineering strain may not be representative of the actual strain at the investigated point in the specimen. However, considering that (i) the strain was in excess of 70 % and (ii) the sample surface was quite smooth, indicating no severe localization of strain, the dislocation density may be considered to be sufficiently high to generate significant ε-martensite.
ii. The rate of twin formation at lower temperatures is expectedly higher. A higher number of twins, implies a possible lower number of dislocation-twin boundary interactions for a given dislocation density. However, just like in the previous case the dislocation density is extremely high due to the high strain and sufficient not to restrict ε-martensite growth.
iii. Finally, the thermodynamic motivation for ε-martensite nucleation and growth is based on the difference in free energy of the FCC and the HCP structure. Based on DFT calculations by Niu et al. [53], it is observed that the rate change in this free energy difference becomes progressively lower and practically plateaus at cryogenic temperatures. There is no additional thermodynamic driving force for the formation of

ε-martensite at lower temperatures. However, the stress to move a dislocation, including that of gliding the Shockley partial along the twin boundary, increases non-linearly with decreasing temperature. This makes phase transformation significantly more difficult at lower temperatures. Considering the (i) consistence of thermodynamic driving force at cryogenic temperatures and (ii) increased difficulty of dislocation glide, integral to martensite nucleation and growth, the volume fraction of martensite formed at cryogenic temperatures does not change significantly as a function of temperature.

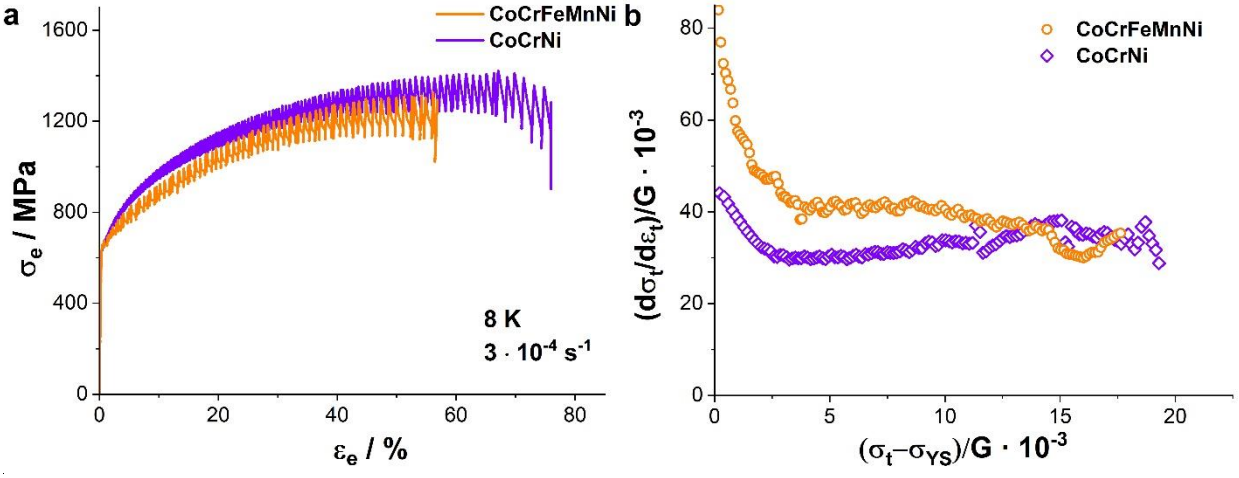

Figure 4.19: (a) $\sigma_e - \varepsilon_e$ plot for CoCrFeMnNi and CoCrNi at 8 K and the corresponding (b) plot of shear modulus normalized work-hardening, $\left(\frac{d\sigma_t}{d\varepsilon_t}\right)/G$, vs. extent of deformation, $\frac{\sigma_t - \sigma_{YS}}{G}$. The work-hardening rate was estimated from the stress maxima points of the serrations seen in (a).

Pursuant to the second question: does this highly proliferated martensite have an additional strengthening contribution? To verify this the work-hardening rate of CoCrNi is evaluated in comparison to non-TRIPing CoCrFeMnNi at 8 K (Fig. 4.19b). It is seen that the work-hardening plateau region, where TRIP and TWIP effects are active, are quite similar in magnitude for both alloys. This is further reinforced by the significant overlap in work-hardening curves, already discussed above at 77 K (Fig. 4.7b). At 77 K and 8 K CoCrFeMnNi shows twinning and CoCrNi shows both twinning and martensite formation. Despite this, there is no additional work-hardening contribution. This is likely due the low volume fraction of the ε-martensite. The dislocation twin boundary interactions in both alloys have

a similar strengthening contribution, despite their different natures. However, the higher strain to failure in CoCrNi may be a result of dislocation delocalization. The accumulation of dislocations leads to a stress concentration and crack initiation. This is true for a pile-up consisting of mainly edge dislocations, as formulated in the seminal work of Stroh [90]. In the case of CoCrNi, the Shockley partials are expected to glide along the twin boundary for full dislocations of near edge character. This delocalizes dislocation accumulation at twin boundaries. On the other hand, since CoCrFeMnNi does not show any martensite formation it does not have a dislocation delocalization effect. Direct microstructural evidence for CoCrFeMnNi and CoCrNi showing this effect is hard to establish, however, the consistently large strains to failure for CoCrNi are indicative of this hypothesis.

5 Serrated plastic deformation

5.1 Current state and outcome

Serrated plastic deformation at cryogenic temperatures was first reported in the fifties [77, 91, 92] as an auxiliary observation while investigating fundamental stress-strain behavior in single crystals. Early works in the fifties and sixties put forth fundamental hypotheses explaining the possible causes for serrated plastic deformation. This was mainly related to either (i) thermomechanical instability [93, 94] or (ii) dislocation dynamics based mechanical instability [91]. Subsequently, alternative hypotheses were made, considering materials specific phenomena like TWIP and TRIP [95, 96] related to machine stiffness, dislocation particle interactions [97] and dislocation velocity variation [98] to name a few. Despite this, most of the research in the field was primarily focused on the former two hypotheses.

Some of the work done on austenitic steels (304, 316 LN, 308 and 310S to name a few) in the past few decades indicates mechanical basis for the origin of the phenomenon [36, 37, 38, 39, 95, 99]. However, a thermomechanical origin [100] and TWIP based origin [101] have been considered in reports published as recently as 2020. The goal of the current work is to identify the origin of cryogenic serrated plastic deformation. This is done by understanding the nature of the instability, identifying a model and verifying it based on experimental results. Additionally, the alternative causes for cryogenic serrations were invalidated. Most of the work presented in this chapter has already been published in Refs. [29, 31].

5.2 Thermomechanical and mechanical instability model

The thermomechanical instability model was first proposed by Basinski [93, 94]. The fundamental basis of this model is that discrete localized deformation causes a heat release which in turn leads to stress drops. Thermal conductivity (λ) and specific heat capacity (C_p) for a metal/alloy decrease non-linearly with decreasing temperature [102, 103, 104]. At 0 K, these parameters tend to zero. Correspondingly, the heat release from local deformation remains localized due to the low conductivity and results in a large temperature spike, due

to the low specific heat capacity. Since there is an exponential variation in yield/flow stress with respect to temperature, a localized temperature spike results in local thermal softening. This in turn manifests itself in a stress drop or a serration when plotting the engineering stress-strain curve. Multiple reports have illustrated temperature spikes, coincident with stress drops [38, 94, 99, 105].

The mechanical model on the other hand is based on dislocation motion being restricted. Seeger [91] first proposed a model based on screw dislocation mobility at cryogenic temperatures. According to this model, jogged screw dislocations leave behind trails of zero-dimensional defects (mainly vacancies), which are formed after having intersected forest dislocations [106]. In contrast jogged edge dislocations do not generate any vacancies. Fig. 5.1 illustrates how this happens. Fig. 5.1a and b display an edge dislocation (orange) intersecting a forest dislocation (black), resulting in an out of plane defect (jog highlighted in blue). The plane for conventional motion of the parent dislocation as well as the jogged portion are parallel to each another. When a screw dislocation intersects a forest dislocation, the corresponding planes of motion for the jogged and unjogged portions are perpendicular to each other (Fig. 5.1c and d). As the parent dislocation moves forward it is pinned at the jog and bows outwards from this point (Fig. 5.1e). At some critical value of stress, the jogged portion lurches forward leaving behind rows of vacancies (Fig. 5.1f). Vacancy generation is inherently associated with an energy cost. At higher temperatures, this cost is met through thermally activated vacancy generation. The temperature based contribution is minimized at cryogenic temperatures and needs to be compensated by a higher applied stress. This in turn makes screw dislocations less mobile at lower temperatures. Expectedly below a particular temperature there is no screw dislocation motion.

During the course of deformation, dislocations are blocked by and pile up at lattice barriers. At higher temperatures where screw dislocations are mobile they cross-slip out of these pile-ups. However, at lower temperatures, where they are supposedly immobile and pile-ups are made of edge dislocations, cross-slip is not a viable option. Correspondingly, dislocations remain in pile-ups until the stress field generated at the head of the pile-up breaks down the barrier or activates a dislocation source on the adjacent side of the barrier. This in turn allows for sudden flow of dislocations without any hindrance, which is manifested by a stress drop or serration. The primary barrier considered here are Lomer-Cottrell (LC) locks.

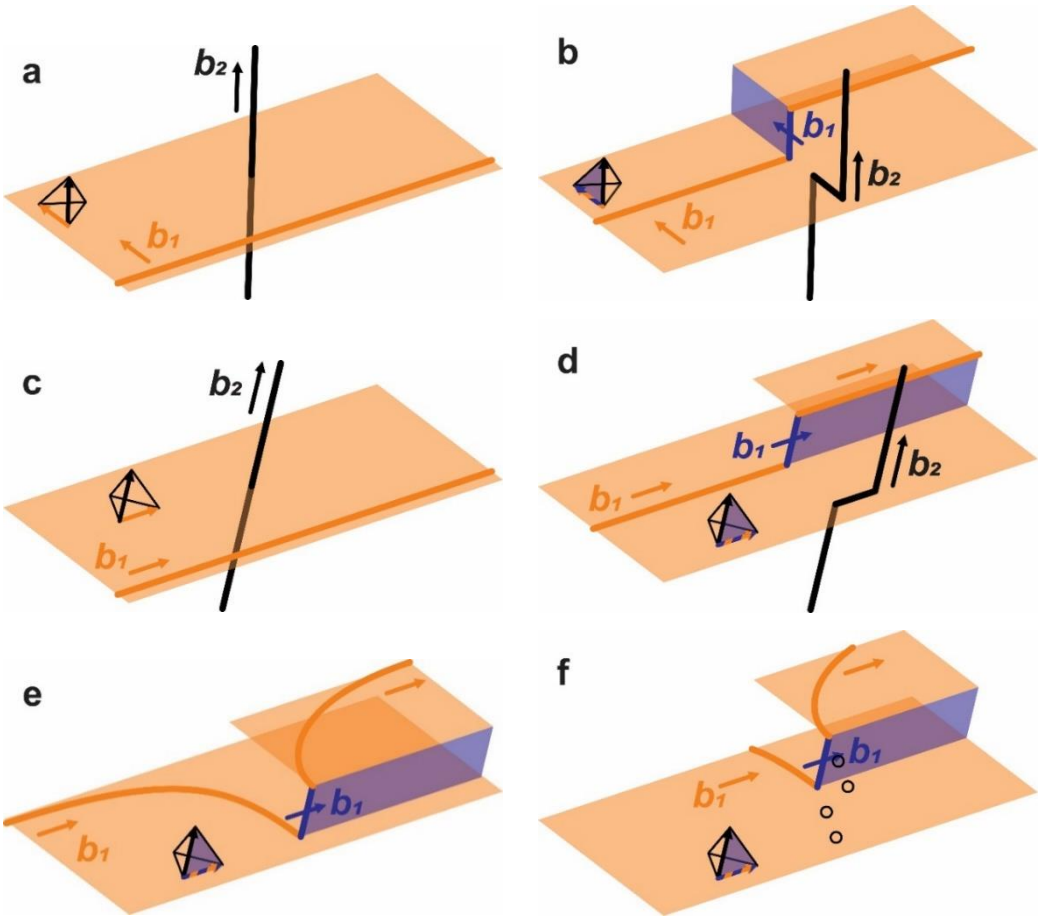

Figure 5.1: Intersection process of a moving dislocation with a forest screw dislocation: (a,b) moving edge and (c–f) moving screw dislocation. The orange lines represent the main dislocations, the black lines represent forest dislocations and the blue lines represent jogs. The slip planes of the original dislocations and the jogged segments are given by the orange and blue planes, respectively. The Thompson tetrahedra on the lower left indicate the slip plane along which each of the dislocations can be found. Moving edge dislocation: (a) prior to intersection and (b) post- intersection with a glissile reaction segment (jog). Moving screw dislocation: (c) prior to intersection, (d) post-intersection with sessile reaction segment (jog), (e) bowing out of the parent dislocation on either side of the jog and (f) formation of trails of vacancies (black circles) behind the jog as it engages in non-conservative motion.

In order to effectively evaluate if the cause for serrated plastic deformation is thermomechanical or mechanical in nature a suitable alloy has to be chosen. The primary

requirement would be that of a single phase material, likely of an FCC crystal structure. A single phase FCC crystal structure provides a significant ductility during mechanical testing and correspondingly a wide range for investigation. Solid solution strengthening correlates positively with this effect [35], so an alloy with significant solute content is preferred. Based on the tenets of the mechanical model, low to medium SFE materials would maximize this effect [91, 107]. On the basis of the thermomechanical effect, an alloy showing exponentially decreasing C_p and λ, with temperature, would have the highest sensitivity to local deformation. Accordingly, this material would show the highest propensity for serrations.

Given these requirements, austenitic steels appear to be the perfect probe material. This class of steels has often been the material of choice for the investigation of this phenomenon in the past [36, 37, 95, 99, 108, 109]. However, there are two underlying issues with it: (i) Austenitic steels show generally martensite transformation at cryogenic temperatures, intervening with existing phenomena [110]. This makes serration-cause correlation more complex. (ii) Austenitic steels have a non-negligible interstitial content (C and/or N) which makes it difficult to both control the composition from batch to batch as well as ensure homogenous interstitial solute distribution within the alloy. To this end, CoCrFeMnNi not only emphatically fulfills the requirements (predominantly confirmed in Chapt. 4), it also circumnavigates both the issues seen in austenitic steels.

The primary focus of the study has been to first evaluate the validity of the thermomechanical vs. mechanical model and additionally build a model that fully explains the experimental results. It should be noted that alternate hypotheses were deliberately avoided since the phenomenon has long been considered to be only thermomechanical or mechanical in nature. Nevertheless, Sect. 5.7.1 considers both, the established and alternate variants of proposed hypotheses in literature and explains why they would be invalid, given the current results.

5.3 Influence of extrinsic factors

Serrated plastic deformation of CoCrFeMnNi was analyzed under different experimental conditions to maximize the influence of experimental parameters. Based on the resulting differences the fundamental cause for the serrations could be analyzed. Three sets of experiments were conducted, namely (i) in different cooling media, (ii) with different gauge

dimensions and (iii) at different strain rates. The former two conditions serve to change the heat dissipation ability of the specimen, however, the third condition changes the time allowed for heat dissipation.

5.3.1 Varying cooling medium

Fig. 5.2a shows the $\sigma_e - \varepsilon_e$ curves of CoCrFeMnNi tested in liquid He (at 4.2 K) and He vapor (at 8 K) along with the corresponding stress-drop amplitude ($\Delta\sigma_e$) measurements plotted as function of σ_e in Fig. 5.2b. $\Delta\sigma_e$ was measured as the drop in stress from the maxima of a serration to the following minima. A minor portion of the drop is a result of the machine contributions. It comes from the machine being unable to unload the sample and maintain a constant extension rate, as soon as a stress drop takes place. This minor contribution was suitably eliminated. The details of how the characteristic data points of the serrations were determined and other values were measured is explained in Appendix 11.2.

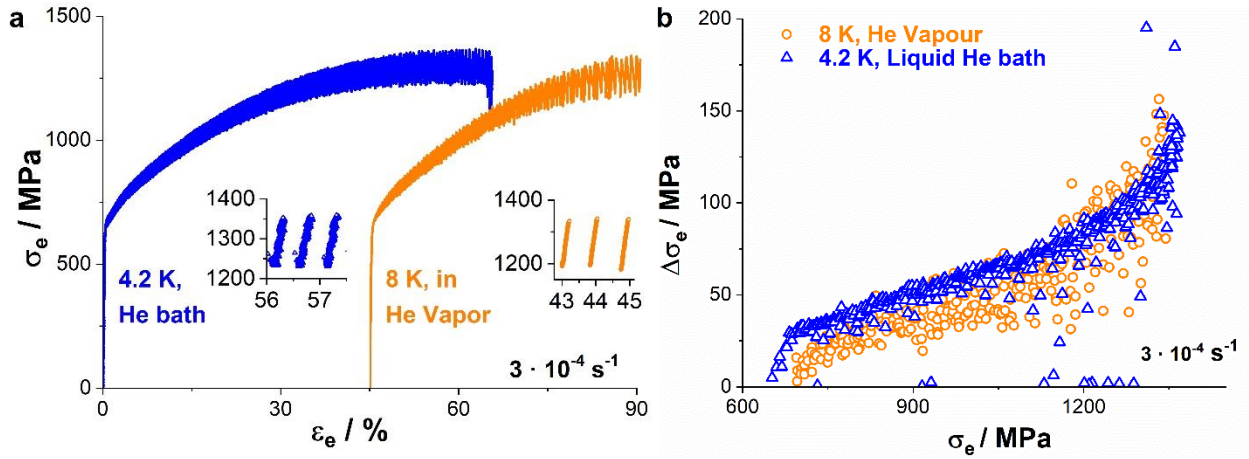

Figure 5.2: (a) $\sigma_e - \varepsilon_e$ plot for CoCrFeMnNi deformed in liquid He, 4.2 K (blue) and He vapor, 8 K (orange), and (b) the corresponding $\Delta\sigma_e - \sigma_e$ plot showing serration intensity variation with deformation. The $\Delta\sigma_e$ was measured from serration maximum to subsequent serration minimum. The machine contribution to the stress drop was accounted for and suitably eliminated.

The test conducted at 4.2 K was carried out in a liquid He bath. On the other hand, the test conducted at 8 K took place in a sealed chamber with He vapor of partial pressure 50 mbar. It should be noted the specimen immersed in liquid He was not constantly in active contact

with the cooling medium, as a result of the Liedenfrost effect [111]. Nonetheless, the specimen heat dissipation abilities would be quite different from the specimen in He vapor. Fig. 5.2b, shows a minimal difference in serration characteristics despite the difference in heat dissipation abilities. The specimen immersed in liquid He has slightly higher $\Delta\sigma_e$, during the initial deformation but both curves align almost completely for the majority of deformation. Under the thermomechanical theory, a liquid cooling medium (even with an unstable coupling), has a better heat dissipation effect in comparison to low pressure vapor environment. Based on this, the $\Delta\sigma_e$ at 4.2 K should be significantly lower than at 8 K. This is, however, not the case. Two assumptions have been made here (i) the variation in strength between these two specimens is not significant and (ii) the critical step in heat dissipation has to do with cooling medium-specimen thermal coupling. The first condition is justified since $\sigma_{YS} = 650\ MPa$ for both specimens shown in Fig. 5.2. If the second condition is false and the critical step in heat dissipation has to do with heat conduction through the specimen (and not with heat conduction from specimen to cooling medium) then this question is answered in the following section, Sect. 5.3.2. Nevertheless, the $\Delta\sigma_e - \sigma_e$ variation shows insignificant difference from the varying 'thermal coupling' of the specimen and cooling medium.

5.3.2 Varying gauge dimensions

In contrast to the varying cooling medium the critical condition for heat dissipation in this section may be considered as heat conduction through the specimen. The previously presented specimens have had a gauge section of 4 mm in diameter. The current test was conducted on specimens of gauge diameter 2 mm. This doubles the surface area to volume ratio of the specimen (from 1 mm^{-1} to 2 mm^{-1}).

Both specimens were tested at 8 K and the corresponding results were presented in Fig. 5.3. Once again the serration characteristics are quite consistent despite the varying heat dissipation ability. In combination with the effect of cooling medium it seems quite evident that the serration characteristics are not varied by changing heat dissipation characteristics. This is true regardless of when considering thermal coupling between specimen and cooling medium or on the specimen's thermal conductivity.

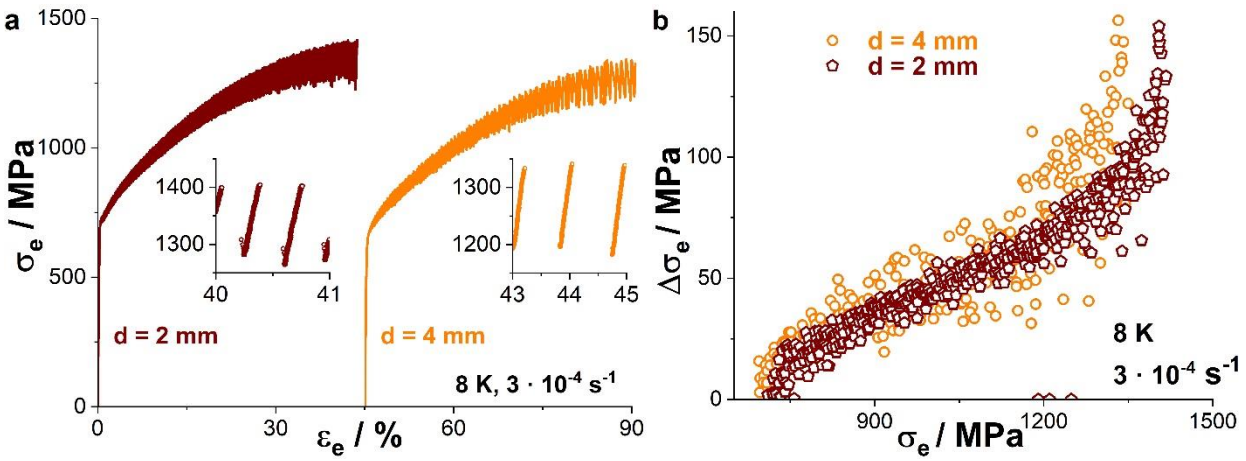

Figure 5.3: (a) $\sigma_e - \varepsilon_e$ plot for CoCrFeMnNi deformed at gauge diameter of 4 mm (orange) and 2 mm (brown), and (b) the corresponding $\Delta\sigma_e - \sigma_e$ plot showing serration intensity variation with deformation.

5.3.3 Varying strain rate

The specimens tested thus far have been strained using a constant cross-head displacement rate of 0.5 mm/min. This corresponds with an approximate plastic strain rate of $3 \cdot 10^{-4}\ s^{-1}$. Two additional tests were conducted at 8 K at plastic strain rates of $6 \cdot 10^{-5}\ s^{-1}$ and $1 \cdot 10^{-3}\ s^{-1}$. The results of these tests are as presented in Fig. 5.4.

For the strain rate of $6 \cdot 10^{-5}\ s^{-1}$, the $\Delta\sigma_e - \sigma_e$ plot is shifted slightly upwards. Considering the intrinsic scatter of the data, the difference is minor. In the case of a slower strain rate, there should have been greater time to allow for heat dissipation during local strain events. This should avoid stress drop events altogether or at least reduce their intensity. It is possible that the stress drops occur at such a velocity that the change in strain rate at these orders of magnitude make no difference, however, no version of the thermomechanical model would allow for a higher stress drop amplitude at a slower strain rates. These results contradict the thermomechanical effect. Additionally, at the higher strain rate of $1 \cdot 10^{-3}\ s^{-1}$, the shape of the discontinuous stress-strain curve is quite different. Instead of the consistent sharp stress drops there exists a step-like curve. The reason for the lack of stress drops has formerly been attributed to the thermal state of the sample. According to this, there exists a maximum strain rate for serrations to be clearly observed, above which the deformation is so fast that the resultant heat from plastic straining does not have

sufficient time to dissipate [112]. The specimen is then being deformed at a temperature higher than the nominal test temperature. This reason appears plausible, but does not explain the step-like nature of the deformation. The present feature will be explained in Sect. 5.5, on the nature of strain during serrated plastic deformation.

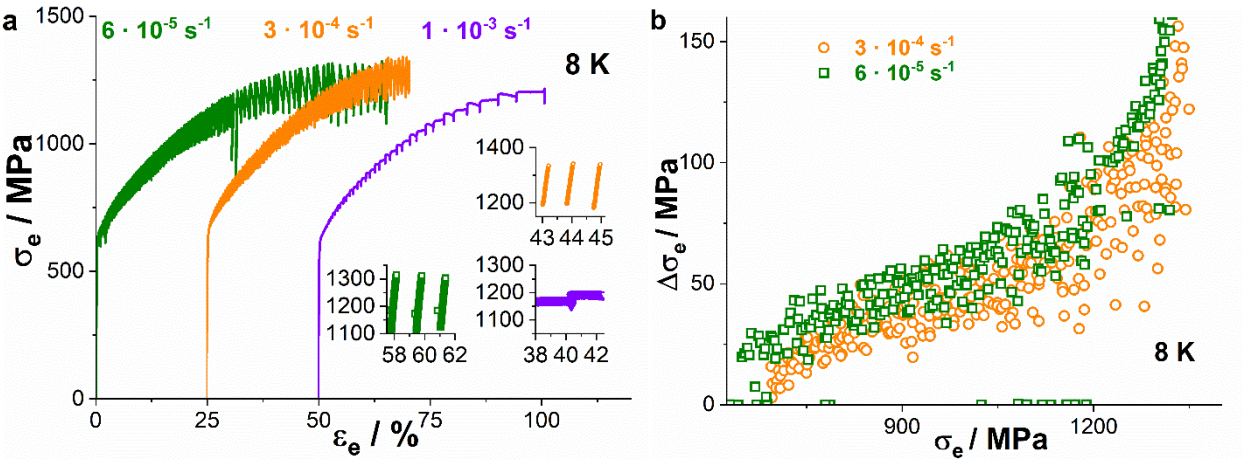

Figure 5.4: (a) $\sigma_e - \varepsilon_e$ plot for CoCrFeMnNi deformed at plastic strain rates of $3 \cdot 10^{-4}\ s^{-1}$ (orange), $6 \cdot 10^{-5}\ s^{-1}$ (green) and $1 \cdot 10^{-3}\ s^{-1}$ (violet), and (b) the corresponding $\Delta\sigma_e - \sigma_e$ plot showing serration intensity variation with deformation. The $\Delta\sigma_e - \sigma_e$ at $1 \cdot 10^{-3}\ s^{-1}$ has not been plotted. The discontinuities for this condition are not in the form of sudden stress drops, that may be readily evaluated. The nature of this special type of discontinuity is discussed in greater detail in Sect. 5.5.

Considering the effects of the different experimental conditions in the current section, there is clearly no effect from the thermal coupling or heat dissipation characteristics. Additional experimental results in the current chapter reinforce this. It is currently clear that the serrations are motivated by some dislocation based phenomenon with consistent stress relations and not by local thermomechanical instability. The likely candidate is thus the mechanical model.

5.4 Mechanical model for serrations

There have already been some well-established proponents of the mechanical model [37, 99, 109, 113], based on the original model of Seeger [91]. They have firmly established some

aspects of the model but these articles did not accurately characterize the microstructure or measure relative intensities of the serrations given by the different conditions, as is done in the current work. These reports investigated austenitic steels which actively show the TRIP effect. Despite this, martensite was not actively considered as a microstructural feature. Additionally, while Ref. [37], proposes a consistent phenomenological basis, it doesn't provide a model for transition from continuous plasticity to discontinuous plasticity with decreasing temperature. This transition is explained through the mathematical model in Ref. [99]. In this case there are two points that define the model: (i) The critical condition for serrated plastic deformation to occur is a combination of a minimum shear stress at the head of dislocation pile-ups and a minimum number of LC locks causing pile-ups. This condition was illustrated in Fig. 5.5a. It is based on the fact the in the mechanical model serrated plastic behavior is motivated by edge dislocations pile-up at LC locks. According to this condition when either one or a combination of LC lock density or number of dislocations piled up at LC locks reaches a critical value, serrations will be seen. (ii) In the temperature range of 40 – 0 K, the number of LC locks increase exponentially with decreasing temperature. This is illustrated in Fig. 5.5b. Accordingly, as the temperature decreases, condition (i) is more easily fulfilled. As a result of the higher LC lock density, serrations are seen below a given temperature. Using these conditions as the basis serrated plastic deformation was mathematically modelled in Ref. [99]. In spite of the elegant analytical modeling, this solution leads to some counterintuitive phenomenological notions (like the expectation of an exponentially increasing LC lock density with decreasing temperature). The report additionally fails to make some considerations, like the effect of TRIP, which had formerly been accounted for in similar investigations [114].

The task at hand is then to develop an appropriate model, which correctly accounts for the results of these previous reports while still answering the questions they cannot. To do so, two sets of experiments on the CoCrFeMnNi alloy were carried out. A series of tests were conducted from 8 K to 35 K and the serration characteristics were evaluated. Additionally, a pre-deformed specimen with significantly higher dislocation density was deformed at 8 K and compared with the fully recrystallized specimen with a significantly lower dislocation density.

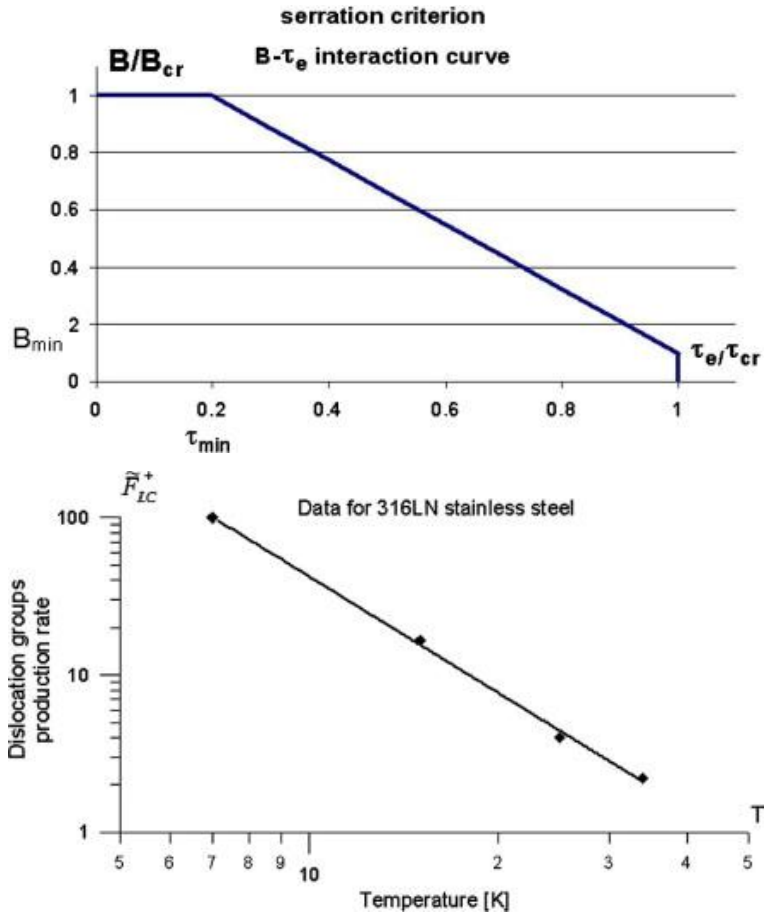

Figure 5.5: (a) Critical condition for serrations as defined by the plot of normalized LC lock density vs. normalized shear stress at the head of the dislocation. B is the LC lock density in the specimen. B_{cr} is the critical lock density beyond which serrations are seen irrespective of stress at the head of the dislocations pile-up. τ_e is the stress at the head of a pile-up and τ_{cr} is the critical stress for which, regardless of the LC lock density serrations are seen. (b) Plot of LC lock formation rate ($\tilde{F}_{LC}^{+}$) as function of temperature on a log-log scale. Both (a) and (b) were taken directly from Ref. [99].

5.4.1 The effect of temperature

Fig. 5.6a and b, respectively, show the $\sigma_e - \varepsilon_e$ and $\Delta\sigma_e - \sigma_e$ trends for CoCrFeMnNi at four different temperatures ranging from 8 K to 35 K. The curves for each temperature are offset in the former graph to clearly resolve the results. The first observation is that a lower temperature corresponds with a comparatively greater stress drop amplitude. Serrations are thus more intense at lower temperatures. They additionally require some critical

minimum plastic strain to be activated at a given temperature (when tested above 15 K). The precondition is thus linked to a minimum dislocation density, stress value or a combination of the two. Furthermore, it appears that despite the consistently greater stress drops seen at 8 K in comparison to 15 K, the $\Delta\sigma_e - \sigma_e$ slopes are similar. At these two temperatures, the serrations begin at yield point. Thus, at higher temperatures like 25 and 35 K, it is likely that a greater dislocation density corresponds with a steeper change in the $\Delta\sigma_e - \sigma_e$ slope.

The steepest slope is seen at 35 K where the greatest amount of continuous deformation is present prior to the initiation of serration behavior and correspondingly highest dislocation density is expected at this stage. This is based on the assumption that the change in dislocation density with change in strain is approximately similar in the temperature range of 8 – 35 K.

CoCrFeMnNi shows cryogenic serrations at a higher temperature than any other material, both at yield point (15 K) as well as at some point during plastic deformation (35 K). While 316LN steel reportedly shows stress drops at similar temperatures, 34 K in Ref. [37] and 36 K in Ref. [109], they are quite sparse. At 34 K, only three stress drops were visible and they did not have a consistent trend. At 36 K a single stress drop was seen and it is not clear if this was a result of the same phenomenon. It is possible this single stress drop is associated with necking instability/failure. In the case of CoCrFeMnNi, however, a clear discernable trend was observed. The trend provided valuable information related to yielding , the $\Delta\sigma_e - \sigma_e$ trend, and strain during serrated plastic deformation (discussed in Sect. 5.5).

It should be noted, Fig. 5.6c representing the work-hardening behavior for each of the specimens, shows similar deformation behavior in each case. Chapt. 4 has already shown that different deformation mechanisms are associated with different work-hardening rates. There exists a consistence between serrated and continuous deformation. This is especially important at 25 K, which shows significant strain in both ways. Consequently, it may be stated that no new deformation mechanism is activated in order to facilitate serrated plastic deformation.

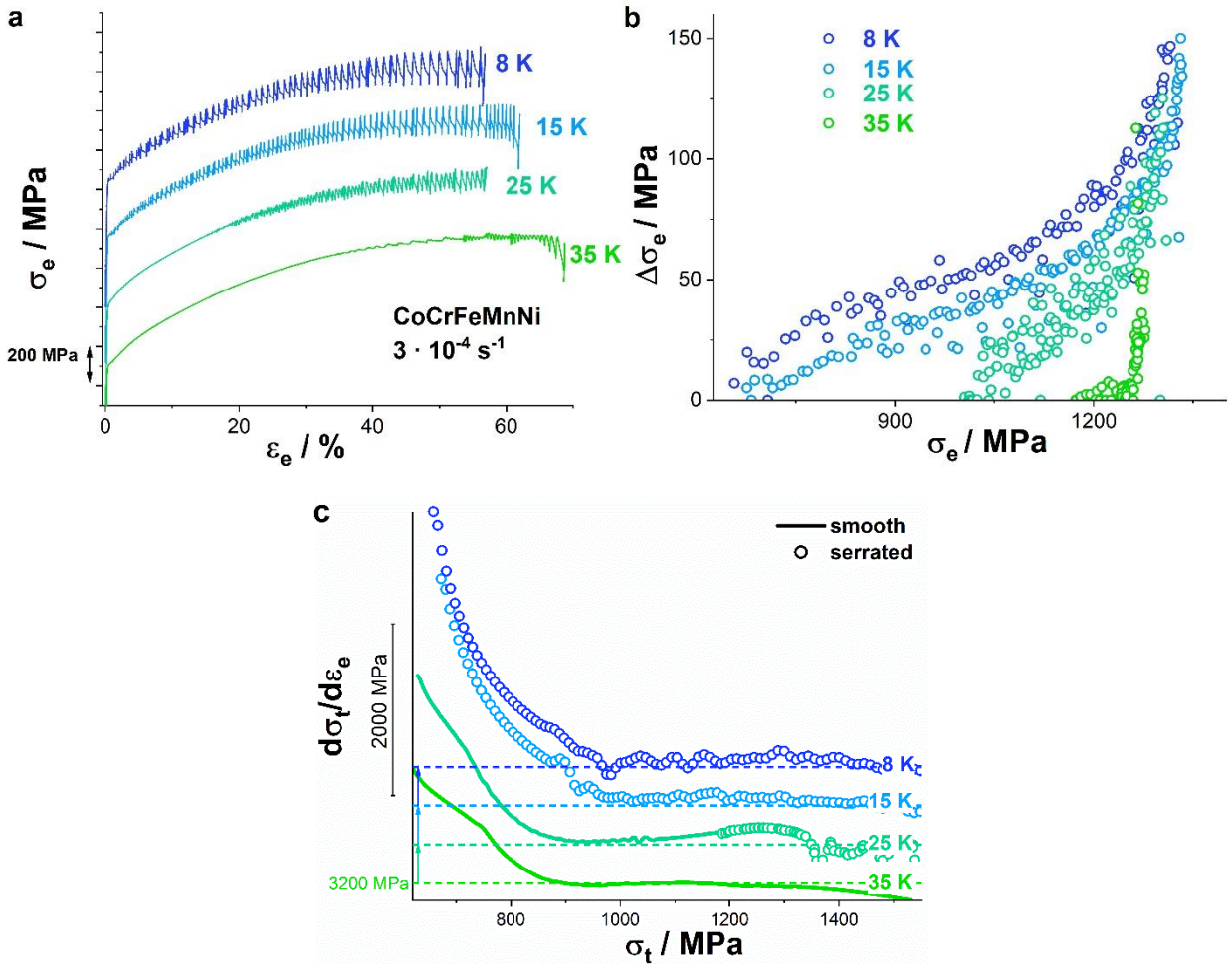

Figure 5.6: (a) $\sigma_e - \varepsilon_e$ curves of CoCrFeMnNi deformed at 35 K, 25 K, 15 K and 8 K, (b) corresponding $\Delta\sigma_e - \sigma_e$ curves. In (a), the $\sigma_e - \varepsilon_e$ curves are vertically offset to better resolve the individual features as the curves would otherwise overlap significantly. (c) $\frac{d\,\sigma_t}{d\,\varepsilon_t} - \sigma_t$ curves of CoCrFeMnNi deformed at 35 K, 25 K, 15 K and 8 K. The data in (c) has been smoothened to allow for interpretation of the serration data. The offset of each data set is indicated using the 3200 MPa dashed baseline. The circles represent data for serrated deformation and the smooth line represents data for continuous deformation. The $\frac{d\,\sigma_t}{d\,\varepsilon_t} - \sigma_t$ for the serrated portion was determined from the maxima of the serrations.

5.4.2 The effect of pre-deformation

Based on practically all conceivable models, dislocation density has a dominant effect on the intensity of serrations. Correspondingly, CoCrFeMnNi was wire drawn (subsequent to a

homogenization) to a true strain (ε_t) of 40 % at 77 K. A tensile test of a specimen was then conducted at 8 K. The dislocation density for the fully recrystallized states and the wire drawn specimens are expected to differ by multiple orders of magnitude. The $\sigma_e - \varepsilon_e$ and $\Delta\sigma_e - \sigma_e$ plots for the reference recrystallized case as well as the wire drawn specimen are shown in Fig. 5.7.

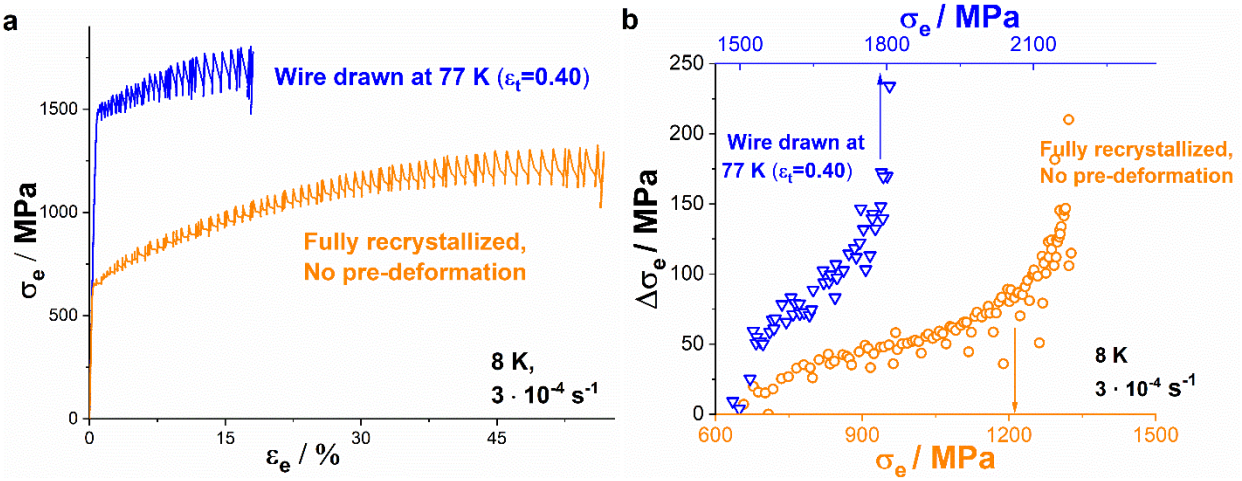

Figure 5.7: (a) $\sigma_e - \varepsilon_e$ curves for deformation of CoCrFeMnNi at 8 K in the recrystallized and the pre-deformed condition and (b) corresponding $\Delta\sigma_e - \sigma_e$ curves. The range of the abscissa is the same in (b), implying that a visually steeper curve does have a higher $\Delta\sigma_e - \sigma_e$ variation. The appropriate axes for each of the specimens is specified using arrows.

Contrary to expectation, the initial stress drop amplitude of the pre-deformed specimen is quite low and increases at a significantly faster rate than the reference condition. The $\Delta\sigma_e - \sigma_e$ relation is much weaker than for the fully recrystallized case. These observations contradict the expectedly higher $\Delta\sigma_e$ in the pre-deformed specimen. However, the steep $\Delta\sigma_e - \sigma_e$ slope is akin to deformation at 25 and 35 K, where the dislocation density at serration initiation is higher than at lower temperatures. Thus, it is clear that dislocation density does not have a one to one correlation to the stress drop amplitude. The effect of dislocation density has been interpreted further in Sect. 5.4.4.

5.4.3 Cross-slip propensity

Based on the above set of experiments the established observations include: (i) serrations are more intense at lower temperatures; (ii) a higher dislocation density, while not directly influential, plays a significant role. The intuitive question is how does this information play in to the mechanical model? To incorporate these results correctly into the model, the original model is reinvestigated. While Seeger [107], attributed the serrations to a fundamental lack of mobility of screw dislocations, the cause is more likely inability to cross-slip and dislocation pile-up characteristics. Screw dislocation mobility was considered to be the only important factor for cross-slip, however, there are other factors that affect cross-slip propensity as well as pile-up characteristics at low temperatures. The four key factors are as follows:

i. Cross slip energy: Cross-slip seen during stage III deformation in single crystals is an activate part of plastic straining in polycrystalline samples. Cross-slip is inherently more difficult at lower temperatures, as well as for lower SFE materials [92, 115]. The activation energy originally proposed for cross-slip is related to the SFE and the shear modulus (G) in the following way:

$$E_{CS} = K \cdot \frac{G}{\gamma_{SFE}} \qquad \text{Eq. 5.1}$$

Considering that γ_{SFE} decreases and G increases with decreasing temperature E_{CS} is the greatest at 0 K. This equation represents the Schoeck-Seeger theory [92, 115]. However, even when considering the widely accepted Friedel–Escaig mechanism of cross-slip [116, 117], this statement remains valid. By contrast, the Fleischer mechanism of cross-slip need not be considered here, since it has mainly been used when discussing cross-slip in metals with high SFE (like Al) [118, 119]. Fig. 5.8 shows the variation of constriction energy of partial dislocations (the critical factor in cross-slip energy estimation), according to the formula given in Ref. [116], based on the Friedel–Escaig model [117].

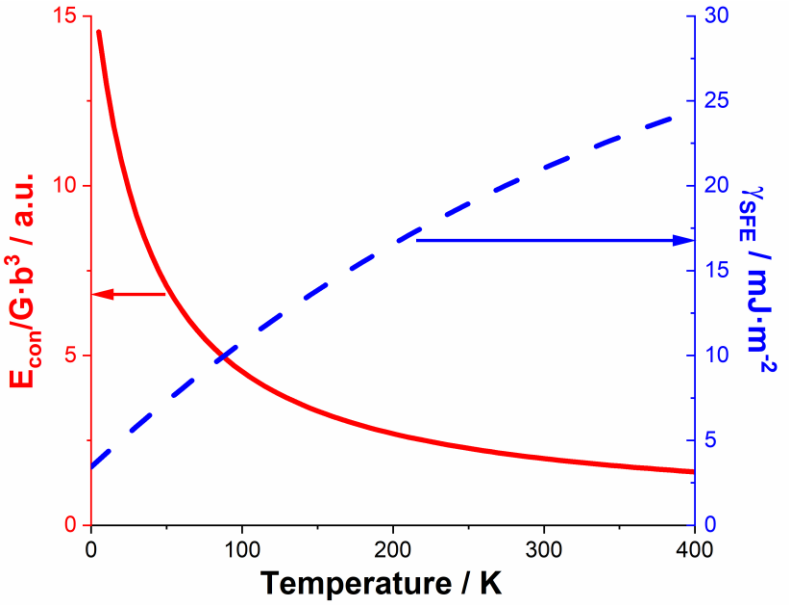

Figure 5.8: Plots for the variation of $E_{con}/G \cdot b^3$ for CoCrFeMnNi and γ_{SFE} as a function of temperature. The normalization is carried out since E_{con} is directly proportional to this term ($G \cdot b^3$) as per the formula given in Ref. [116]. The respective ordinate axes have been marked by arrows. γ_{SFE}, G and b at various temperatures were as estimated in/extrapolated from Ref. [28, 66, 103] respectively.

The SFE variation for CoCrFeMnNi was taken from Ref. [28]. The G and b variations were extrapolated from equations for the same at higher temperatures, as given in Refs. [66] and [103] respectively. The plot clearly shows that with decreasing temperature, the decreasing SFE corresponds with a drastically increasing constriction energy (E_{con}). This in turn results in increased difficulty of cross-slip at these low temperatures. E_{con} only represents the chief energy cost associated with cross-slip. However, cross-slip propensity is statistical in nature and varies according to the Arrhenius relation. This makes cross-slip even less likely at lower temperatures in particular when considering a given E_{con}.

ii. Dislocation mobility: As already discussed in Sect. 5.2, the mobility of (jogged) screw dislocations decreases intensely with decreasing temperature. The example in that section considered a full screw dislocation. However, real metallic materials, like CoCrFeMnNi, generally have extended or dissociated dislocations and loops with mixed

character. In order to imagine the effect in a 60° dislocation (near edge) an illustration has been provided (Fig. 5.9).

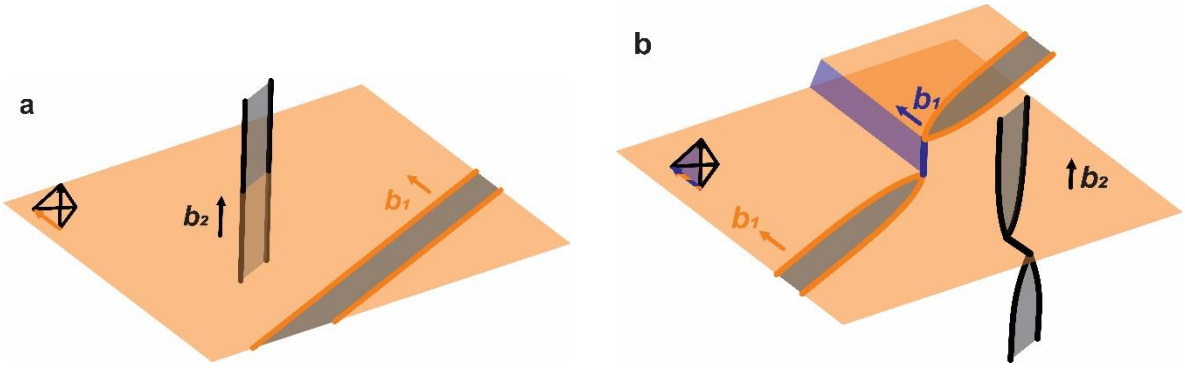

Figure 5.9: Intersection process of a moving extended near edge (60°) dislocation with a forest screw dislocation: (a) Near edge and forest screw dislocation are shown with their respective Burgers vectors (b_1 and b_2). (b) Post interaction, the formation of jogs on the intersecting dislocations. The parent dislocation and jog are indicated by the orange and blue lines respectively. The forest dislocation is indicated by the black line. The faulted region between the partial dislocations is indicated by the transparent grey portion. The slip planes of the original dislocations and the jogged segments are given by the orange and blue planes, respectively. The Thompson tetrahedra, indicates the slip planes along which each of the dislocation can be found.

In general, the dislocation product of a mobile and a forest dislocation (jog/kink), glides on the plane given by the cross product of the Burgers vector of both dislocations. The direction of conservative motion for the jog in the current case is off-angle from the direction of motion of the parent dislocation. Since this dislocation is a 60° dislocation, the jog deviates by 30° in its direction of motion. This is still not so significant as to necessitate interstitial defect formation during dislocation motion.

Fig. 5.10 shows a 2-D representation of the Thompson tetrahedron. All the slip systems in an FCC crystal are represented in this figure with green lines representing full

dislocation Burgers vectors and the blue lines representing partial dislocation Burgers vector.

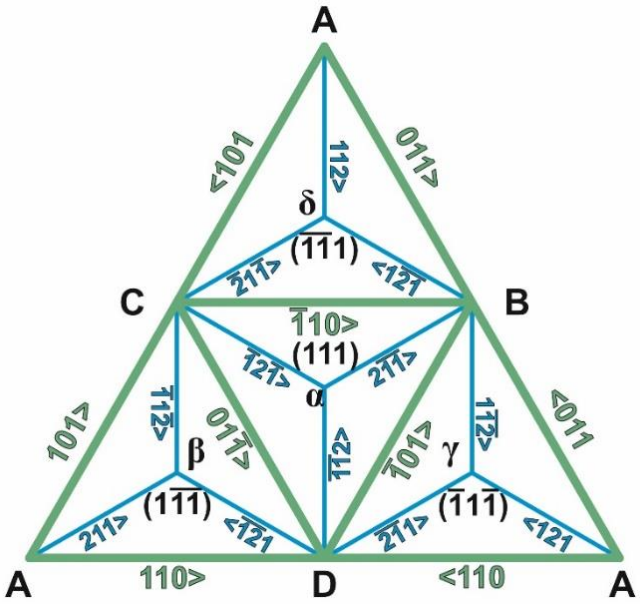

Figure 5.10: 2-D representation of the Thompson tetrahedron. The green lines represent Burgers vectors for full dislocations and the blue lines represent the Burgers vectors of Shockley partials. The different planes are indicated in black text (α, β, γ and δ) along with the corresponding Miller indices ((111), $(1\bar{1}\bar{1})$, $(\bar{1}1\bar{1})$ and $(\bar{1}\bar{1}1)$ respectively).

Using this convention Fig. 5.11 shows (i) the 3-D illustration of a jogged mobile dislocation, (ii) an overhead view of the jogged dislocation and jog slip plane, and (iii) a 2-D representation of the Thompson tetrahedron highlighting the directions of dislocation vector, Burgers vector, slip plane and force. This was done for the three cases: (i) pure edge (Fig 5.11a-c), (ii) pure screw (Fig 5.11d-f) and (iii) mixed 60° dislocations (Fig 5.11g-i). Here force F, per unit length of the dislocation, was considered to be the result of shear stress acting on the slip plane of the parent dislocation, acting in the direction perpendicular to the dislocation line. This is in line with how shear stress manifests itself as applied force on a dislocation. F is given by the equation

$$F = \tau \cdot b \qquad \text{Eq. 5.2}$$

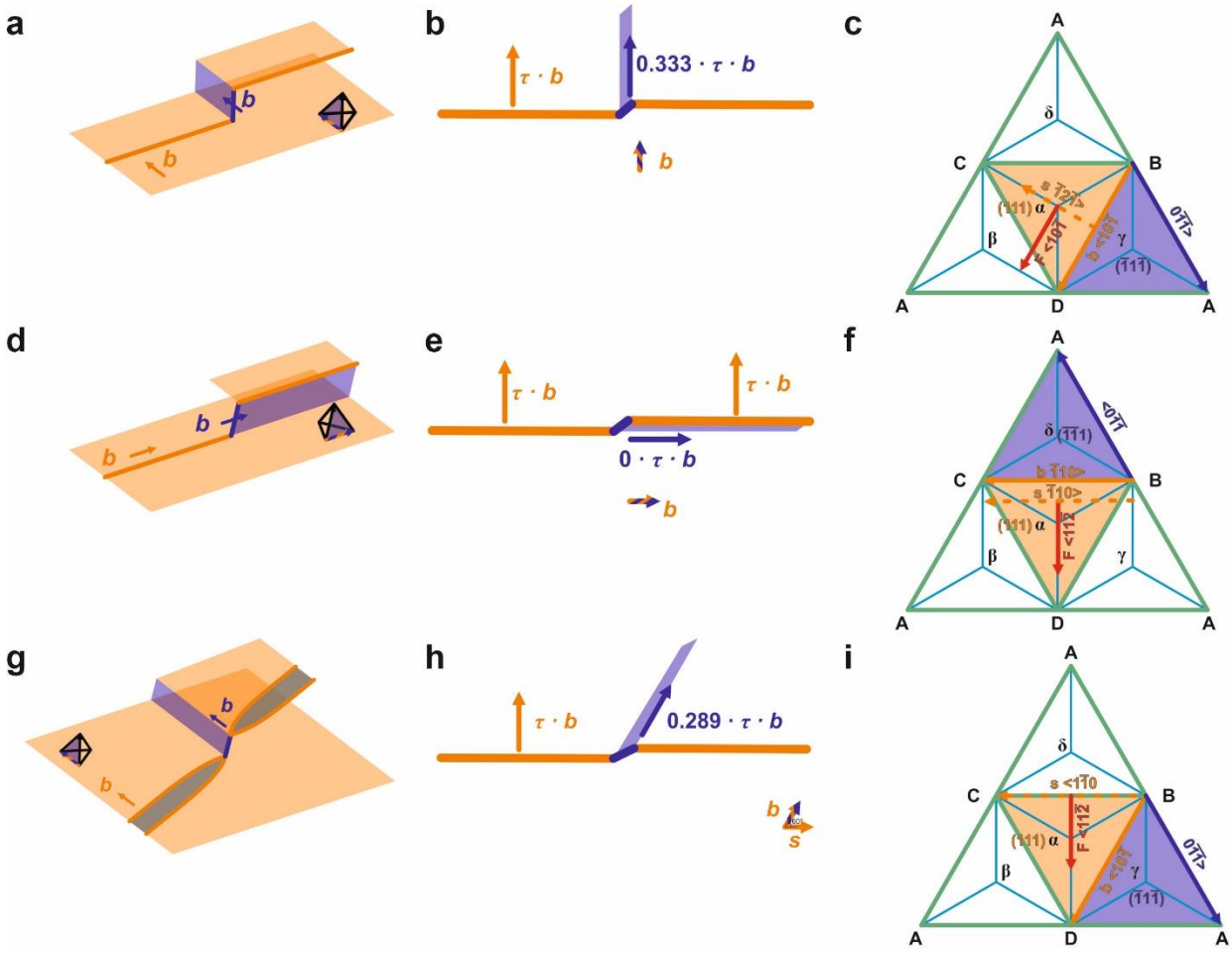

Figure 5.11: 3-D representation of jogged (a) edge, (d) screw and (g) mixed 60° dislocations. The respective overhead views in the [111] direction for (b) edge, (e) screw and (h) mixed 60° dislocations respectively. The Thompson tetrahedron is additionally provided with indications of the slip plane, dislocation line vector and Burgers vector of the parent dislocation and the jog. The Thompson tetrahedron representations correspond with (c) edge, (f) screw and (i) mixed 60° dislocations respectively. The arrows in (c), (f) and (i) represent only the direction of each of the specified parameters and their length should not be taken as an indicator of magnitude.

Since F acts in the direction perpendicular to the parent dislocation line vector, the component of F that acts on the jog of a parent edge dislocation is $F_{jog} = F \cdot \cos(0°) \cdot \cos(70.53°)$. This is the result of the projection of F (force as a result of shear stress on parent dislocation) on the slip plane of the jog. Conversely, in the case of a pure screw dislocation the force acting on the jogged portion is zero since the angle between the shear stress and the slip plane of the jog is 90° ($F_{jog} = F \cdot \cos(90°) \cdot \cos(70.53°)$).

In a mixed dislocation the slip plane of the jog is off axis from the shear stress direction by an angle equal to that between the dislocation line and Burgers vector. The force in this case varies with the sine of the angle between the dislocation line vector and the Burgers vector, represented as θ. A general form is $F_{jog} = F \cdot \sin\theta \cdot \cos(70.53°)$. In every case $cos(70.53°)$ is seen as a multiplier, since this is the projection of force as a result of the angles between the parent dislocation and jog slip planes. Considering this, for all cases, except in near pure screw dislocations, a finite fraction of the force is projected on the slip plane of the jog. This is seen as the reason why jogs in extended dislocations may move freely without vacancy formation as opposed to pure screw dislocations [106].

Fig 5.12, is a plot of force on the jog as a fraction of the force acting on the parent dislocation, for various angles between dislocation line and Burgers vector. It shows that that increasing edge nature of a dislocation correlates with increasing force projected onto the jog. Moreover, based on the analysis of Hirsch [120], jogs formed on dislocations of near edge nature are glissile. Conversely, extended dislocations of near screw nature are more likely to form sessile dislocation segments during dislocation interaction and jog formation.

A simplified equation for the stress to bow out the parent dislocation from the jogged pinning positions is given in Ref. [107] by

$$\tau_{bow} = \frac{\alpha G b}{l_0} \qquad \text{Eq. 5.3}$$

Here α is a coefficient associated with the mechanism of dislocation bowing out and l_0 is the spacing between jogs (α is material dependent and in the range of 0.1 - 0.2 for Cu [107]). The pinning stress is thus lower for more widely separated jogs. For more

widely spaced jogs, dislocations can bow out significantly before the jogged portion needs to lurch forward. On the other hand, for narrow separations, pinned screw dislocations have much less bow out capacity. To that end, they have significantly less mobility before jogged portions move forward while producing vacancies. A higher dislocation density has the indirect result of greater dislocation-dislocation interaction and thus smaller l_0. At cryogenic temperature jogged screw dislocations become less mobile and edge dislocations cannot dissipate the effects of dislocations pile up at barriers through cross-slip. The only remaining option is for activation of a dislocation source from the stress at the head of the dislocation pile-ups.

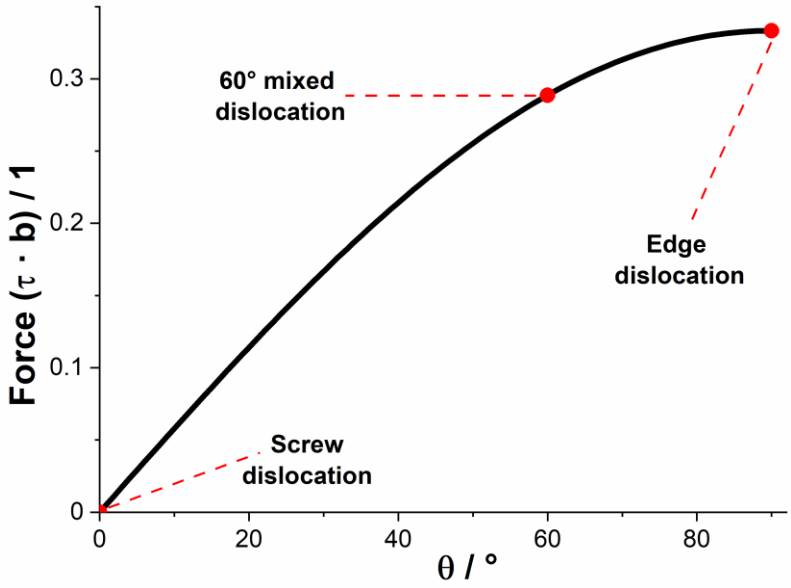

Figure 5.12: Plot of force on the jog in terms of $\tau \cdot b$, where τ is the shear stress experienced by the parent dislocation and b is the corresponding Burgers vector. θ is the angle between the dislocation line vector and the Burgers vector for the parent dislocation. $\theta = 90°$ indicates complete edge and $\theta = 0°$ indicates complete screw dislocation. The figure shows complete edge and screw as well as mixed 60° dislocations marked out.

iii. LC lock formation rate: As previously explained, the SFE of CoCrFeMnNi decreases with decreasing temperature and, correspondingly, Stacking Fault Width (SFW) increases.

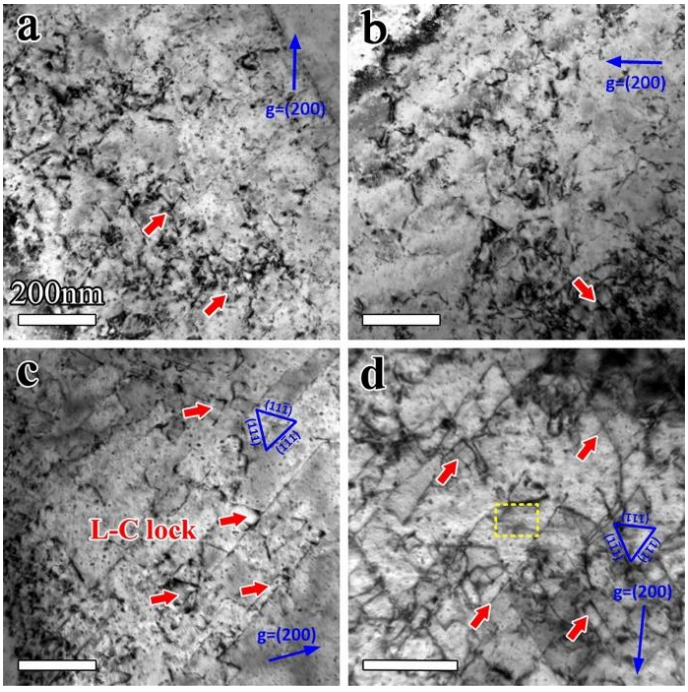

Figure 5.13: TEM micrographs of CoCrFeMnNi at a $\varepsilon_e = 8\,\%$ taken under the diffraction condition of $g = (200)$. (a) & (b) Micrographs of specimens deformed at 77 K. (c) & (d) Micrographs of specimens deformed at 4.2 K. The LC locks were indicated by red arrows. A large number of LC locks were found at 4.2 K than at 77 K this case. [121]

The interaction between solutes and dislocations is far more intense at cryogenic temperatures where distortion around a solute is severe, especially in CoCrFeMnNi, as elaborated in Sect. 4.1. This extends the SFW distribution as the leading and trailing Shockley partials are differently pinned, thus increasing the possibility of partials of two different slip systems interacting with each other.

Additionally, considering that there exists an inverse dependence of dislocation density on temperature for a given amount strain, the number of LC locks at lower temperatures is expected to be higher. This feature has been qualitatively verified for CoCrFeMnNi by Pu et al. [121]. Fig. 5.13, taken directly from Ref. [121], shows the TEM micrographs identifying LC locks at 77 K and 4.2 K. The number of locks detected at 4.2 K is significantly greater than at 77 K. No LC locks were detected at RT by the authors, however. All specimens were deformed to $\varepsilon_e \sim 8\,\%$. It is likely that the higher dislocation density at lower temperatures facilitated higher LC lock formation rate. It

would thus be easier to identify LC locks at lower temperature, even though they are formed at all temperatures.

iv. Pile-up characteristics: With respect to pile-ups, the stress at the head of a dislocation pile-up is dependent on the number of dislocations in the pile-up. Lower temperatures require larger external stresses for dislocation motion as well as activation of dislocation sources. The equilibrium length of the pile-up increases with decreasing SFE. The equilibrium SFW of the dislocations in the pile-up correspondingly becomes wider [122, 123, 124]. When the dislocation source is far from the LC lock (low dislocation density), the length of the pile-up is larger due to the lower SFE at lower temperatures. Alternatively, for a high dislocation density, where the source-barrier spacing is low, the space in between can be completely filled up by a lower number of dislocations when the SFE of the metal/alloy is lower. Thus, at lower temperatures, regardless of dislocation density the space between dislocation source and barrier is populated more easily. Thus expected probability of dislocation interaction between dislocations of intersecting slip systems is higher. LC lock formation rate is correspondingly greater at lower temperatures. The addition of dislocations to a pile-up continues until the stress at the head of the pile-up reaches the critical limit for a '*breakdown*'. As the number of dislocations in a pile-up increases, the inter-dislocation spacing decreases [122, 123].

5.4.4 Phenomenological model

Based on the results of the above sub-sections, a phenomenological model was developed. As the temperature decreases, SFE decreases and dislocation density associated with strain increases. This results in an increased formation rate of LC locks. During deformation, these locks act as barriers to dislocations causing pile-ups, further increasing the interactions between dislocations of different slip systems. However, dislocations can escape when a sufficient number of screw dislocations have piled up, equaling critical cross-slip stress at the head of the pile-up. Cross-slip is significantly favorable at higher temperatures and as the temperature decreases the cross-slip activation energy becomes higher. This makes cross-slip more difficult, owing to the decreasing contribution of thermal vibrations. Apart from this, jogged screw dislocations also generate vacancies during slip. Stress required for screw dislocation motion effectively increases at lower temperature. At some critical temperature,

the cross-slip stress, as a result of the aforementioned factors, becomes competitive with the stress to activate a dislocation source at the barrier (LC lock). Below this temperature, dislocation source activation at LC locks occurs consistently. The resulting effect is the cooperative motion of dislocations as opposed to only cross-slip of dislocations, one by one in sequence, at the head of the pile-up, with no substantial easing in stress. This is the transition point from continuous deformation to serrated deformation. Based on the relevant factors temperature and dislocation density dictate the point beyond which dislocation source activation, becomes so great in comparison to cross-slip that serrations are seen. For serrations to be seen at yield point, the temperature needs to be low enough that cross-slip is sufficiently restricted even at low mobile dislocation densities, e.g. as seen at 8/15 K. Alternatively, at higher temperatures, a minimum dislocation density is required, beyond which the proportion of LC locks are high enough and a sufficient number of dislocations are piled up unable to cross-slip, resulting in serrated plastic deformation, e.g. at 25/35 K,

Considering that dislocation density is a significant factor and that jogged screw dislocations, not just dislocations of screw nature, have restricted mobility, the results of the pre-deformed specimen can be explained with the given model and Eq. 5.3. During deformation, screw dislocations increasingly intersect forest dislocations, effectively reducing l_0 between jogged portions, hence making τ_{bow} significantly higher. In the pre-deformed specimen, the intrinsic properties of the material are the same as in the fully recrystallized specimen apart from the significantly higher dislocation density. Due to this high dislocation density, the l_0 is low and τ_{bow} is correspondingly high. However, since the yield stress is also much higher than for a fully recrystallized specimen so the required τ_{bow} is satisfied. Subsequent deformation leads to a greater level of dislocation interaction decreasing the l_0 even faster and restricting the cross-slip even more, which then manifests as the rapid change in $\Delta\sigma_e$. This is likely the result of the significantly higher dislocation density. Thus, while dislocation density influences serrated plastic deformation, it does so through affecting the relative lengths of the unjogged portions of screw dislocations.

5.5 Nature of strain during serrated plastic deformation

The nature of strain during serrated plastic deformation is, as with other stress drop phenomena, localized in nature. The strain was measured using extensometers attached to the specimen as shown in Fig. 5.14. The extensometer does not measure changes across the entire gauge section. It only registers strain variations when they occur in the gauge section within the purview of the extensometer. During continuous deformation no such issues occur since elongation is uniform in nature and the strain scales proportionally for any chosen length within the gauge section. However, for discontinuous plasticity this is not the case. Significant strain takes placed during the drop portion of a serration.

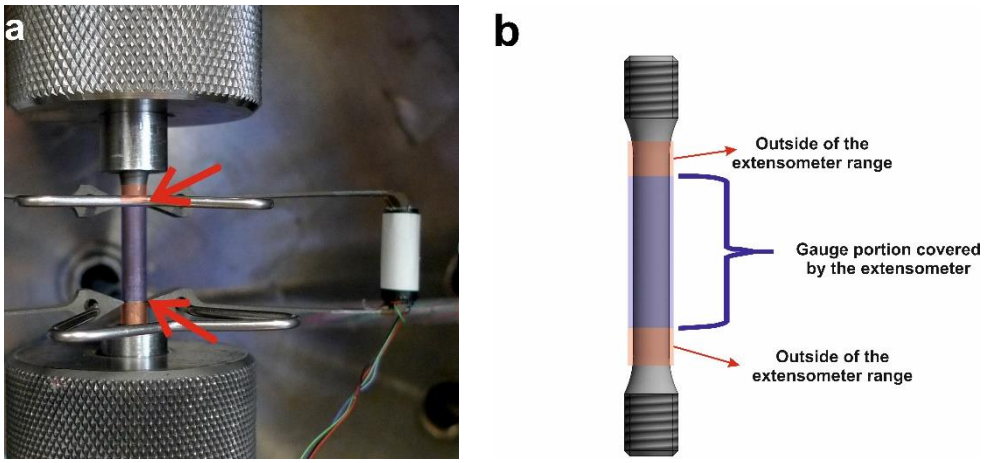

Figure 5.14: (a) Image of specimen attached to the upper and lower cross-heads of the testing machine. A pair of extensometers are attached to the specimen. The region in between the two clamped portions (marked by red arrows), is within the measurement region of the extensometer. This region is marked in blue. The region outside the measurement region, marked in red, undergoes elongation but is not under the purview of the extensometer. (b) A schematic illustrating the different regions in the tensile specimen. The color coding is the same in (a) and (b).

Fig. 5.15 shows the nature of strain variation in CoCrFeMnNi at 8 K, as measured by the extensometer. Three types of strain events are observed in Fig. 5.15b. The first is continuously increasing strain with time and is observed in between stress drops, seen as a smooth stress increase from minima to maxima. This is indicative of reloading of the

specimen post stress drop. Additionally, there are two types of events, being abrupt in nature: (i) A sudden strain jump, associated with the stress drop. A stress drop corresponds with sudden and significant plasticity manifested as a strain jump seen in the upper right inset of Fig. 5.15b. (ii) When this stress drop takes place outside of the extensometer purview it does not register any straining. A sudden localized plasticity results in an unloading in the rest of the specimen reflected as elastic strain recovery. This recovery is not significant but it is noticeable. In turn, it is registered as the negative strain event seen in the lower right inset of Fig. 5.15b.

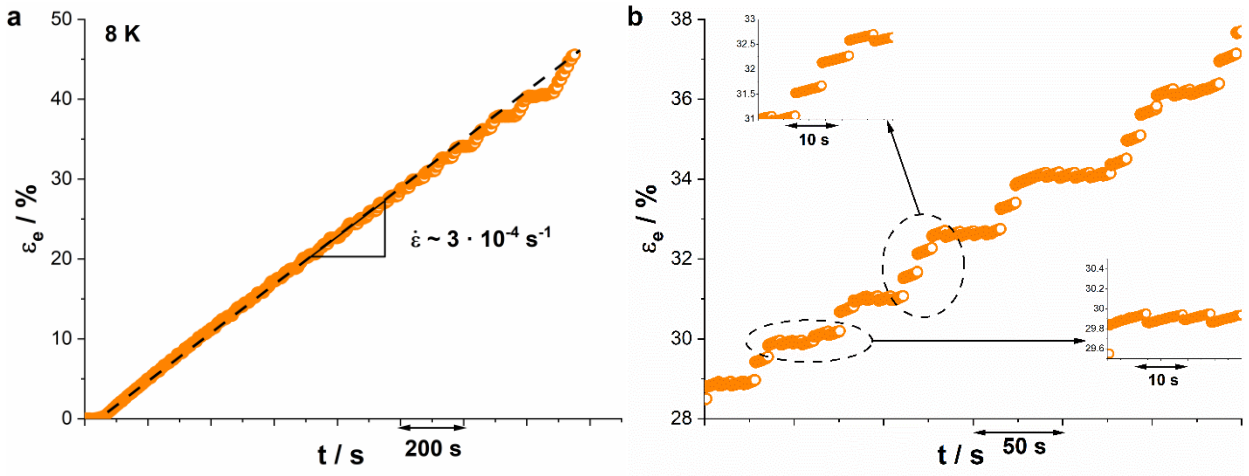

Figure 5.15: (a) Plot of $\varepsilon_e - t$ for CoCrFeMnNi deformed at 8 K, where ε_e is calculated based on extension value registered by the extensometer. The strain rate is marked in the figure. (b) The corresponding close up of $\varepsilon_e - t$. It shows that strain variation is made up of (i) continuous strain change, (ii) abrupt jump and (iii) abrupt small drop. The continuous portion is associated with the elastic reloading of the specimen after each stress drop. The positive strain jumps are associated with stress drops and localized deformation occurring inside the extensometer measurement region and the negative strain relaxations are associated with localized deformation outside the extensometer region. They are both highlighted in the insets.

If the plastic strain jump for a serration is not registered, then the following serration appears over the original one in the $\sigma_e - \varepsilon_e$ data. This is depicted in Fig. 5.16 with $\sigma_e - \varepsilon_e$ and $\sigma_e - t$ tandem plots, where both figures represent the same data set. Significantly more

serrations are visible in the $\sigma_e - t$ plot since in the $\sigma_e - \varepsilon_e$ serrations overlap and hide one another.

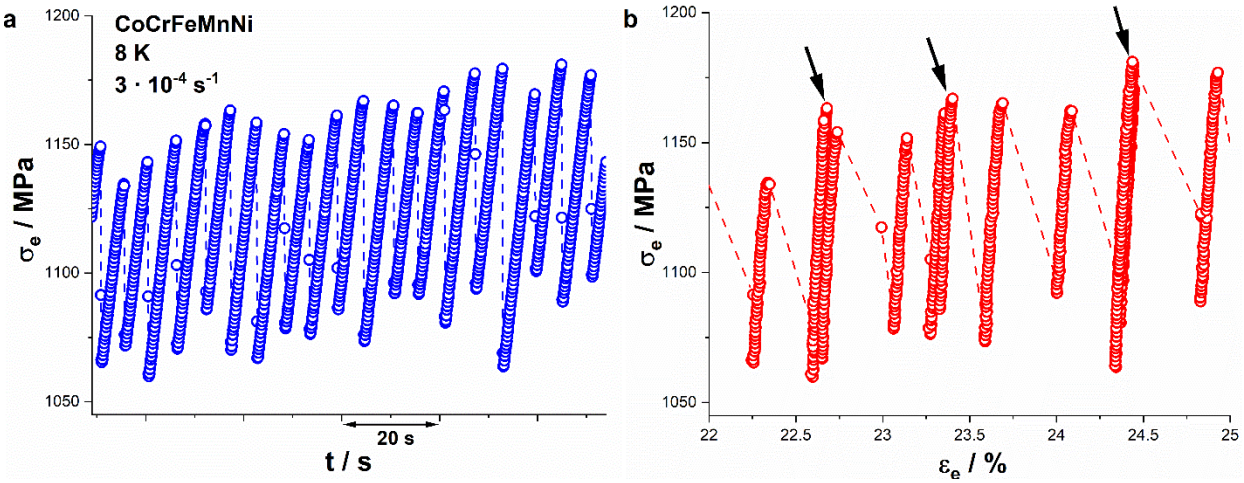

Figure 5.16: (a) Plot of $\sigma_e - t$ for CoCrFeMnNi deformed at 8 K and (b) corresponding $\sigma_e - \varepsilon_e$ plot. Both figures are plotted for the same data set. Black arrows in (b) mark out serrations that overlap since they are associated with strain events outside the extensometer range.

The overlapping serrations are marked by black arrows. For this reason, all the data related to the serrations was extracted using $\sigma_e - t$ data in combination with machine displacement (for procedural details see Appendix 11.2). Abrupt strain events of positive or negative nature, associated with strain within or outside the extensometer range, have previously been shown in Ref. [36]. Apart from localized microscopic strain, seen as serrations, deformation in CoCrFeMnNi additionally highlighted a type of strain that has previously gone unnoticed. Fig. 5.17a shows a close-up of $\sigma_e - t$ curve for CoCrFeMnNi at a 35 K. Aside from the sudden stress drops there is a step like secondary wave.

The second type of discontinuity has a larger wavelength (range of $\sim 40\ s$) compared to the sudden stress drop (range of $< 1\ s$). The discontinuity will be referred to as mesoscopic strain events and the localized sudden stress drops will be referred to as microscopic serrations. It should be noted that this feature is observed at even lower temperatures, however, is not readily obvious (marked in Fig. 5.17b and c). Additionally, it is apparent that

this behavior is seen in past reports as well [37, 109]. Previous reports have not identified this feature within their own reported data.

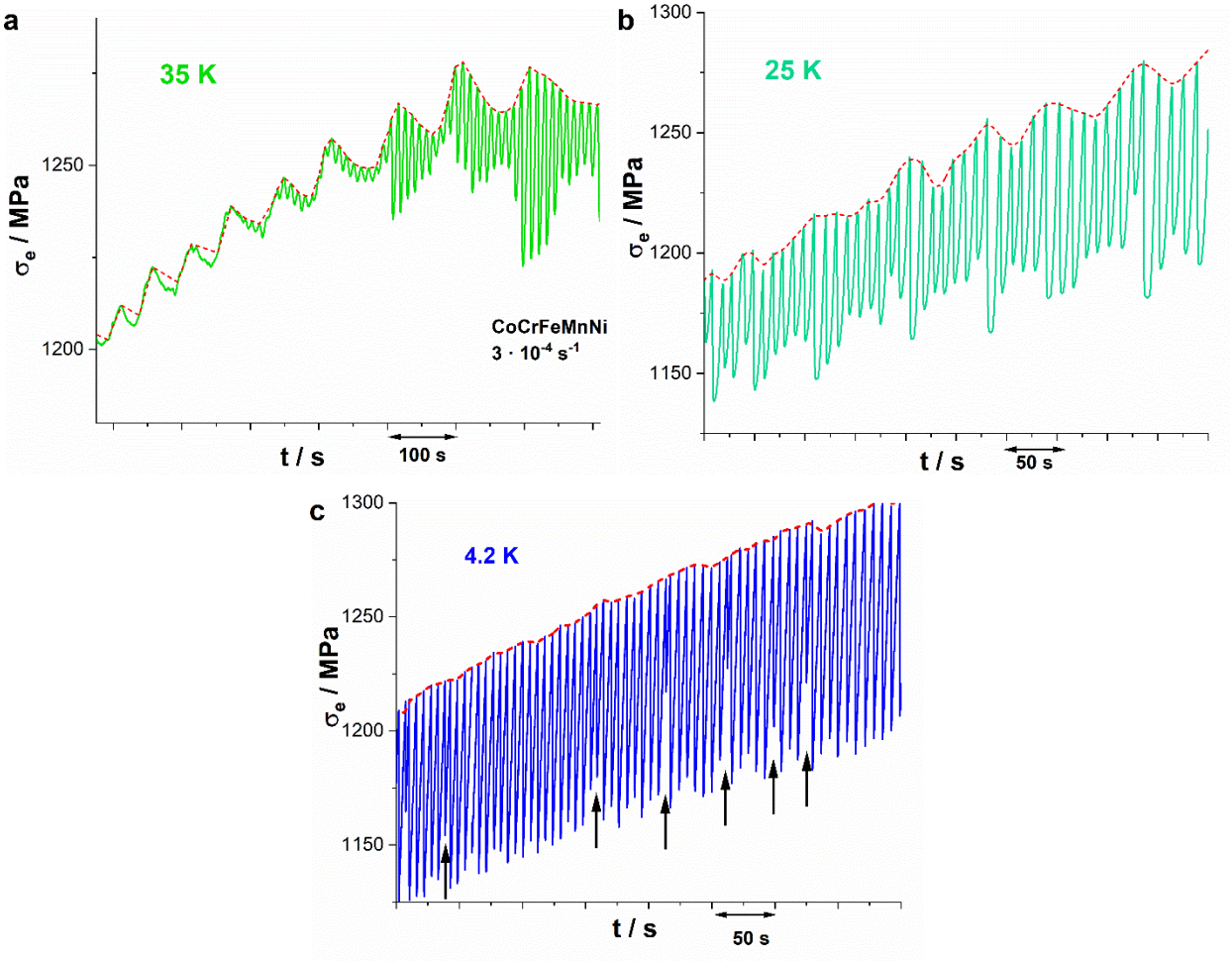

Figure 5.17: Plot of $\sigma_e - t$ for CoCrFeMnNi deformed at (a) 35 K (b) 25 K and (c) 4.2 K. The serrations vary on the basis of a mesoscopic wave. This wave is marked by the red dashed line. Additionally, to make the wave more apparent in (c) black arrows were added denoting jumps in σ_e.

The variation of strain may be explained in the context of the current model. A single serration is the result of microscopic strain from a localized set of dislocation proliferation events. These events take place at various lattice barriers on attaining a critical condition. This in turn results in localized strain. Then, the next localized event happens in the vicinity of this event. Thus localized plasticity events take place in close proximity to one another. In

this way, the microscopic strain events lead to mesoscopic strain. A mesoscopic region may strain until it is strain hardened so severely that a different mesoscopic region can manifest plasticity at a lower stress. In this way localized strain events are then shifted to a different, weaker region. This was investigated in the current results using the data from the specimen deformed at 8 K. Fig. 5.18 shows the $\sigma_{max} - t$ plot for CoCrFeMnNi deformed at 8 K. Here σ_{max} refers to the local maximum engineering stress of the serration. Since Digital Image Correlation (DIC) becomes difficult as a result of the cooling medium at such low temperatures, the evaluation was made using the current extensometer data. Correspondingly, strain can be classified as within the extensometer region (+ strain) and outside the extensometer region (- strain). In Fig. 5.18, for a truly random sequence where a microscopic serration occurs at a random point along the gauge length the sequence of red (- strain) and blue (+ strain) data points is mixed in no particular order.

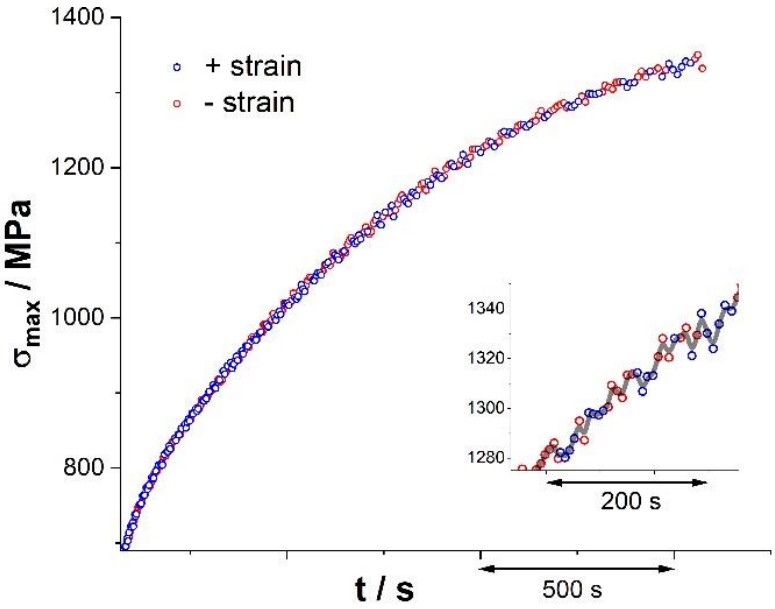

Figure 5.18: Plot of $\sigma_{max} - t$ for the serrated portion of CoCrFeMnNi deformed 8 K. Inset on bottom right shows close-up with a trace showing the secondary wave. Red data points indicate negatively registered strain (outside the extensometer) and blue data points indicate positively registered strain (inside the extensometer region).

Under these circumstance dissimilar strain events (+ strain and - strain) are most likely to occur around each other. If we consider groups of four serrations, an alternating sequence (the most common sequence) is expected approximately 38 times for the given test. This is also the least likely sequence, if microscopic serrations are expected to take place in local mesoscopic regions. The actual number of times this sequence is observed is 13. Of these 13, only 3 occur after $\varepsilon_e \sim 10$ %, contrary to a random case of 25. This is likely because at lower strains the mesoscopic strains consist of fewer microscopic events and at greater strains consist of more microscopic events. It should be noted that these estimates were made while actively considering the total number of serrations that occurred within the extensometer range and outside the extensometer range. These results indicate a highly non-random sequence of straining events. The microscopic serration events thus take place in the vicinity of previous serration events.

Section 5.4.3 reported the step like nature of strain for the high strain rate experiment. This is now identified as purely the mesoscopic wave. While it is still possible that localized heat dissipation plays a role, the step like shape is a result of mesoscopic deformation. In order to manifest plasticity at high strain rates, microscopic strain events throughout the sample are so great in number and overlap so significantly that only the resultant mesoscopic strain is visible. The microscopic events are not distinctly resolvable and so have no distinct effect on $\sigma_e - \varepsilon_e$ plot. This is akin to the effect of increased strain rate during the PLC effect where localized strain events are suppressed, however, the waviness of the $\sigma_e - \varepsilon_e$ curve is still visible at higher strain rates [125, 126]. Here as well, multiple localized events overlap and appear in a non-distinct manner.

5.6 A note on the effect of surface quality of the specimen

The specimens deformed in Sect. 5.3 had their surfaces fully polished to ensure maximum adherence to physical coupling between the specimen and the cooling media. Fine surface polishing was not employed for subsequent experiments. Based on the surface finish the frequency of the serrations varied. This is due to the stress concentrations on a rougher surface which facilitates easy straining. The present observation is in line with previous report on effect of surface finish on cryogenic deformation [127], where rougher surfaces prove to act as sources for dislocations, generating significantly more plasticity than for a

polished specimen. Ref. [127] showed a drop in yield stress for an unpolished specimen, however, that is not currently observed.

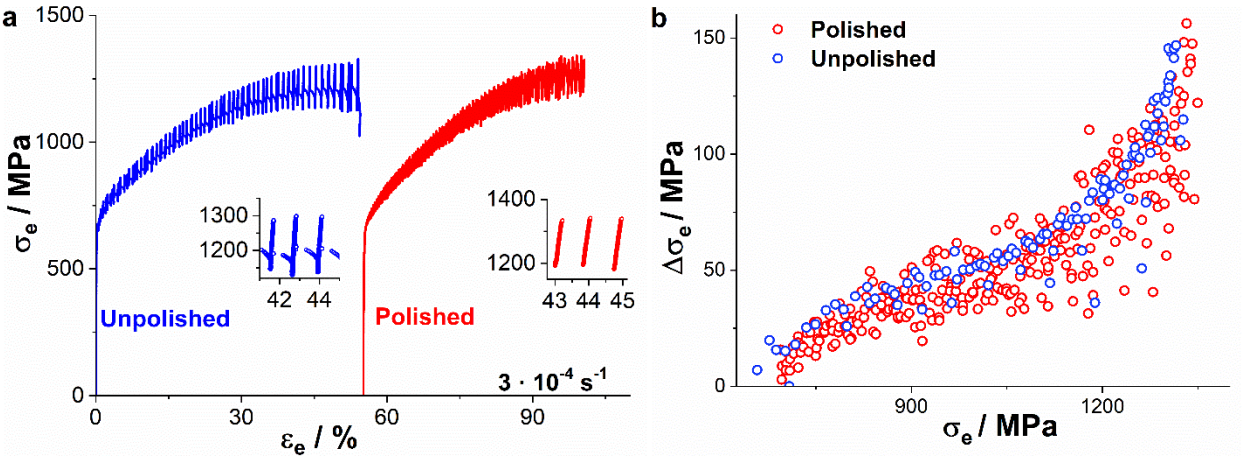

Figure 5.19: (a) Plot of $\sigma_e - \varepsilon_e$ for polished (red) and unpolished (blue) specimens of CoCrFeMnNi deformed 8 K. Insets show a close up of the serrated behavior. Additional data points for the unpolished specimen seen in the inset are a result of a higher acquisition rate (100 Hz), compared to the polished specimen (10 Hz). (b) Plot of $\Delta\sigma_e - \sigma_e$ plot for the specimens shown in (a).

Nevertheless, despite a change in surface quality, the stress drop trend is quite consistent (Fig 5.19b). Considering that the phenomenon of serrated plastic deformation revolves around stress drops and their change in amplitude, the effect of surface quality is irrelevant for current research. The qualitative strain based variations, like the appearance of microscopic and mesoscopic strain events, are also maintained regardless of surface quality.

5.7 Alternate theories and interpretations

While the thermomechanical instability and mechanical instability models were most intensely discussed in literature there exist alternative ideas. In some cases, they were seen as the root cause and in others as magnifier/modifier of the serrations. This section will tackle (i) drawbacks of theories in literature, either directly hypothesized, or through extensions, as well as (ii) drawbacks of the previously defined mechanical model.

5.7.1 Alternate hypotheses

i. Note on the thermomechanical model: The '*definitive*' proof for the thermomechanical model has thus far come in the form of temperature spikes coinciding with stress drop events. While they occur somewhat concurrently, as shown by Ogata et al. [38], it should be noted, that on closer inspection the temperature peaks occur at the end of the stress drop as reported in Ref. [99]. In Ref. [99], the temperature and stress is plotted as a function of strain, making the sequence of events unclear. When plotted as a function of time, however, the temperature spike appears after the stress drop as seen in Fig. 5.20 [128].

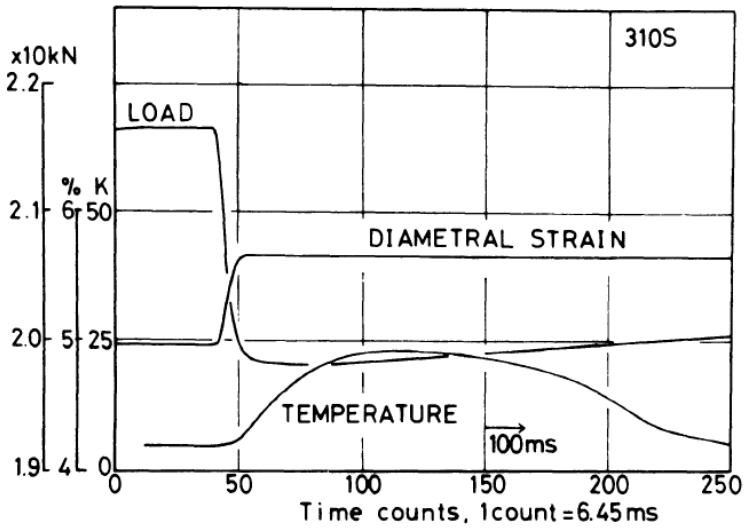

Figure 5.20: Plot of load, strain and temperature as measured for a single serration during uniaxial tensile deformation conducted on 310S steel. The image was taken directly from Ref. [128].

These results indicate that the stress drop is the cause and the temperature spike is the effect. If the temperature spike was the cause for thermal softening, then the peak of the temperature spike should coincide with middle of the stress drop where the drop rate is the fastest [93]. As noted above this is not so.

ii. TWIP/TRIP: As stated previously, a common probe material for study of serrations in the past was austenitic steel. Most austenitic steels are expected to show the TRIP effect and some have confirmed TRIPing at cryogenic temperatures [36, 110]. However, since

several other alloys and pure metals are not expected to show TRIP and yet exhibit serrated plastic deformation at low temperature, it can be disregarded as the cause. TWIP on the other hand is very consistently reported during cryogenic deformation.

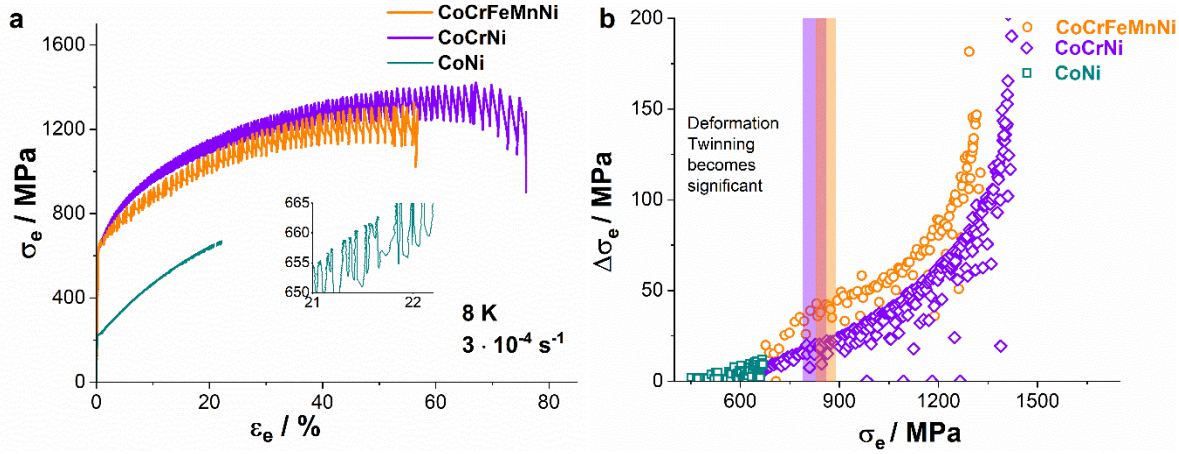

Figure 5.21: (a) $\sigma_e - \varepsilon_e$ curves of CoCrFeMnNi, CoCrNi and CoNi deformed at 8 K and (b) corresponding $\Delta\sigma_e - \sigma_e$ curves. There is a $\sigma_e - \varepsilon_e$ close-up of CoNi in (a) shown as an inset in order to illustrate the serrations. The approximate stress at which deformation twinning becomes significant in CoCrFeMnNi and CoCrNi is marked by translucent bands in (b).

Many of the probe materials, austenitic steel, pure elements like Cu and HEAs to name a few [77, 82, 96, 109], have evidence of the same. TWIP was thus considered a possible cause for cryogenic serrations [95, 96]. However, Fig. 5.21 shows the $\sigma_e - \varepsilon_e$ and $\Delta\sigma_e - \sigma_e$ curves for CoCrFeMnNi and CoCrNi, both of which show deformation twinning only beyond $\varepsilon_e \sim 6$ %. Nevertheless, serrations begin at the yield point. Additionally, CoNi also shows serrated plastic deformation despite showing negligible deformation twinning at these temperatures [30]. This eliminates TWIP as the cause for serrated plastic deformation. Whether or not twin boundaries affect the $\Delta\sigma_e$, is not yet readily clear. The current results show a consistent trend before and after activation of deformation twinning.

iii. Dislocation velocities: At cryogenic temperatures, the speed of dislocations is significantly higher. This is due to the lack of viscous dampening of dislocations, as a result of reduced phonon scattering [98, 129]. However, the latter is more prominent

in pure metals than in alloys. Correspondingly, the effects of reduced phonon scattering are most significant in dilute alloys and only very weak in concentrated alloys [130]. On the other hand, cryogenic serrations are most prominent in concentrated solid solutions as opposed dilute solid solutions [35]. Even in the current set of results, the CoCrFeMnNi, with a much higher solid solution strengthening component, exhibits intense serration behavior in comparison to CoNi. So despite the proposed possibility stated in Ref. [98], dislocation speed variation does not cause the cryogenic serrated plastic behavior.

iv. Solute effects: As mentioned previously, serration phenomena are exacerbated by solute content [35]. This could have been effected, in two ways: (i) the overall strength of the material increases due to solute content and correspondingly a greater stress drop intensity is seen; or because (ii) the dislocations are in some way pinned by the solute atoms and are unpinned at a critical stress. The former is not possible since in our current case, as seen in Fig. 5.21, the stress drop amplitude is greater for CoCrFeMnNi even though the strength of CoCrNi is greater. An increase in the overall strength does not translate to proportionally intense serrations. The latter point is similar to the PLC effect. The issue here is (i) there is no diffusion to allow for constant solute movement to defect sites and (ii) solute pinning has no reason to increase intensity with progressive straining. Serrations of the PLC effect are generally show serrations of low and consistent amplitude. Stress drops of 100 MPa, seen presently, are out of the range of influence of solutes. It is more likely that solutes have a significant influence on pinning Shockley partials and correspondingly changing the existing SFW. It in turn plays towards an inconsistent distribution of SFWs. This is seen at RT for CoCrFeMnNi [131], and is only expected to get more intense at cryogenic temperatures due to the reduced thermal activation of solutes (Sect. 4.1). Solutes in turn change the (i) energy required to constrict a dissociated pair of dislocations, (ii) dislocation spacing in pile-ups, (iii) LC lock formation ability, all of which are positively related to activating serrated plastic deformation. However, solute-dislocation interaction cannot be the primary cause for serrated plastic behavior.

v. Other barriers: Alternative barriers within a grain include cell walls, Taylor lattices, dense dislocation walls, twin boundary and secondary phases. Most of these features require a certain minimum deformation in order to be formed and serrations have been seen at yield point. Secondary phases do not change during deformation, so the change in stress drop intensity is unexplained. Considering that serrations are recognized in single crystals of pure metals as well, the possible cause needs to be something that can be seen within a given grain of a pure metal, without having to fulfill Taylor criterion.

5.7.2 Former mechanical models

Obst and Nyilas [37] verified the original model of Seeger [91] and made some additions. However, according to the description in their report, the instability condition required for serrations was either satisfied or unsatisfied for a given temperature. Correspondingly, below 35 K only serrated plastic deformation should be visible but at 35 and 25 K mixed behavior is seen. This issue is resolved by Skoczeń et al. [99] who assume an exponential change in LC locks in the temperature range below 40 K. In this regard it may be assumed that the LC lock density is quite low when the deformation begins at 25 and 35 K but after sufficient deformation the necessary lock density is achieved. It is achieved at a faster rate at lower temperatures, thus corresponding to lower critical strains to initiate serrated plastic deformation. However, this explanation has no phenomenological backing. As shown in Sect. 5.5.3, LC locks are formed at temperatures significantly greater than those where serrated plastic deformation is active. Instead of the zero LC lock density stated in Ref. [99] (Fig. 5.5a), an exponential increase in LC lock density below 40 K may be assumed, with a constant finite lock density at higher temperatures. Stage II deformation in single crystals is associated with LC lock formation. Work-hardening rates at stage II show relatively low changes in the temperate range of 0 – 293 K [78, 92]. This implies that the expected change in LC lock density should not be exponential in nature.

Conversely, under the current model, cross-slip is active below 35 K (in CoCrFeMnNi) and only decreases in propensity with decreasing temperature. Accordingly, cross-slip is initially viable at 35 and 25 K, but as deformation continues, a significant number of dislocation intersections occur between mobile and forest dislocations. The free dislocation length

between jogged portions (l_0) keeps decreasing. At some critical strain, the l_0 for a significant proportion of the (screw) dislocations is too low to bow out and continue slipping. Subsequently, a portion of the dislocation-based plasticity is carried out through dislocation proliferation events at dislocation pile-ups correspondingly seen as serrations. The instability condition is met after an initial stage of continuous deformation. At lower temperatures the tolerable l_0 keeps decreasing. In Ref. [99], if instead of the LC lock density the number of LC locks that have pile-ups incapable of cross-slip is considered, the model would be validated. However, an exponential increase is still unlikely. Thus, the current model is valid based on the experimental results of the present research, as well as those from previous reports. It resolves the inconsistencies in the previous models (both trivial [37] and conceptual [99]), while presenting suitable modifications.

6 Qualitative validation of the model

The current model is validated on multiple aspects through two experiments. The first experiment is a temperature jump experiment. During this investigation, a tensile test was conducted at a given temperature close to 0 K. Partway through the test the cross-head movement is stopped, the sample unloaded and the temperature changed. This step is repeated twice, so as to investigate three temperatures, for all of which serrations are expected. Based on the resulting trend in serrations, it is possible to identify the nature of the mechanical model. The second experiment is a tensile test conducted on an interstitially alloyed HEA provided by colleagues from the laboratory of Prof. Ian Baker, from the Thayer School of Engineering at Dartmouth. Based on the arguments from Chapt. 5, interstitial solutes should severely intensify the serration behavior. This and other observations from the test were used to verify the current model.

6.1 Temperature jump test

The temperature jump test was provided on CoCrFeMnNi in the fully recrystallized state. The tensile test was started at 8 K. Subsequently after $\varepsilon_e \sim 12\%$, the test was stopped and the temperature changed to 15 K. There are three possible effects from this temperature jump, as illustrated by the $\Delta\sigma_e - \sigma_e$ plots in Fig. 6.1. Fig. 6.1a and b show a condition where the instability condition is met at 8 K by some physical factor, e.g. a minimum dislocation density or minimum LC lock density. Based on Ref. [99] the density of these defects increases exponentially with decreasing temperature, below 40 K. In this respect, at lower temperatures the necessary dislocation/LC lock density is achieved due to its significantly higher production rate [99]. Since this is the critical factor in achieving instability and on changing the temperature to 15 K, the defect density remains unaffected; when the experiment continues at 15 K it should still have retained its instability condition and proceed onwards. This is one of the interpretations of Ref. [99]. In contrast, Fig. 6.1b describes a situation where the defect density increases more rapidly at lower temperatures. At a higher temperature, a strain is required for the necessary defect density to initiate serrated plastic deformation. After the temperature change in this case the instability condition is still met as the test begins. However, since the defect production rate is

significantly higher at 8 K and is necessary for constantly increasing serration intensity the stress drop amplitudes measured in this case should either plateau or decrease. This is an alternate interpretation of Ref. [99].

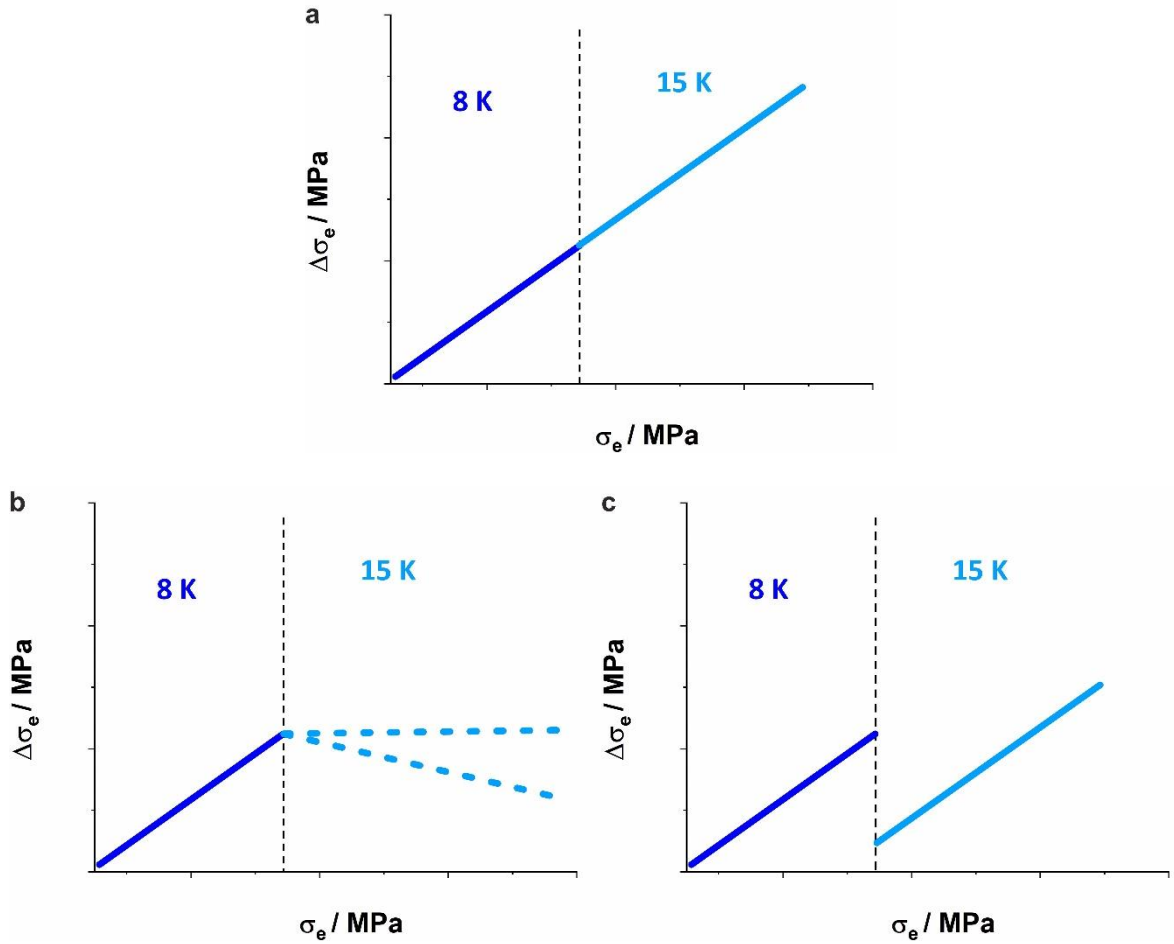

Figure 6.1: $(\Delta\sigma_e - \sigma_e)$ for tensile tests with an interrupted temperature jump. (a) and (b) show possible interpretations of the jump based on exponential change in LC lock density with decreasing temperatures stated in Ref. [99]. (c) shows the $(\Delta\sigma_e - \sigma_e)$ trend for the model in the current work, where the cross-slip ability changes at different temperatures and as a result the serration intensity changes.

Finally, if it is instead considered that both dislocation and LC lock densities do not change significantly in this temperature range, the instability condition is fulfilled by the proportion of screw dislocations that are mobile and the inherent cross-slip ability of dislocations in the specimen. After the interruption in the test and the reloading at 15 K the serrations are

expected to continue since they were observed in the original 15 K test. The $\Delta\sigma_e$ should increase consistently with σ_e. However, $\Delta\sigma_e$ should be lower after the interruption, since the serrations in the conventional 15 K test are less intense than at 8 K(Sect. 5.4.1). This is shown in Fig. 6.1c. During the actual test, after the jump to 15 K, additional temperature changes were made to 25 K and finally back to 8 K. The results are as depicted in Fig. 6.2.

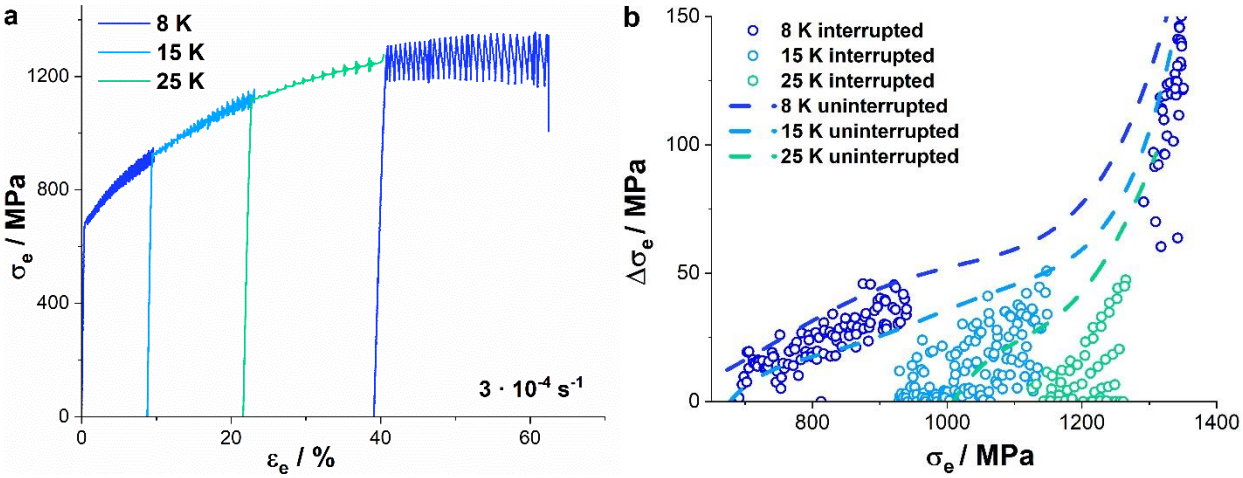

Figure 6.2: (a) ($\sigma_e - \varepsilon_e$) for tensile tests at multiple temperatures and (b) the corresponding ($\Delta\sigma_e - \sigma_e$) plot. The sequence was 8 K, 15 K, 25 K and 8 K again. The set of dashed lines in (b) represent the curves for the conventional uninterrupted test shown in Fig. 5.5 in Sect. 5.4.1.

The results are clearly indicative of the third case discussed above. This implies that the nature of the mechanical model is related to relative cross-slip abilities as a function of temperature and dislocation density. The $\Delta\sigma_e - \sigma_e$ variation for the uninterrupted tests have been included in Fig. 6.2b. At 8 K, there is a mild difference between the uninterrupted and interrupted test results, but this is likely related to the difference in σ_{YS} of the two specimens. If the $\Delta\sigma_e - \sigma_e$ curves are offset by the σ_{YS} difference ($\sigma_{YS} = 650\ MPa$ and $685\ MPa$), there is no difference in $\Delta\sigma_e - \sigma_e$ trends. However, $\Delta\sigma_e - \sigma_e$ are noticeably lower for the uninterrupted tests at 15 and 25 K. One possibility may be explained by the equation for τ_{bow} (Eq. 5.3). According to this the stress to move a pinned dislocation is inversely related to the length of the unpinned portion l_0. At lower temperatures, the minimum l_0 keeps increasing, since it varies directly with the energy to

add a vacancy to the end of a moving dislocation [107]. This energy for vacancy generation increases with decreasing temperature. It is thus likely that several dislocations are immobile at 8 K due to the low l_0, but at 15 K the critical l_0 is greater, making the same dislocations mobile. It should also be noted that since there is an unloading step between the temperature jump steps, there could be an effect on the state of dislocations. Dislocations bow out under stress. When unloaded the dislocations recede partially to the unbowed state, however, as a result of dislocation-dislocation interaction the dislocations do not necessarily recede completely. Correspondingly, the state of dislocations in an interrupted test at a given stress is different from the state of the dislocations in the microstructure of a specimen where no unloading has taken place.

Combined with the high stress, cross-slip is significantly more viable after an interruption and subsequent temperature jump. Correspondingly, serration behavior is not as intense. The same effect is seen at 25 K. However, when the temperature is changed back to 8 K, $\Delta\sigma_e$ increases significantly, mimicking the conventional 8 K curve. It should also be noted that the $\Delta\sigma_e - \sigma_e$ slopes are similar for a given temperature for both the interrupted and uninterrupted tests. While the results in the interrupted test do not overlap with the uninterrupted tests, a drop in $\Delta\sigma_e$, as seen here, can only be explained if serrations are not caused by an exponential change in either dislocation density or LC lock density as temperature decreases (for a given amount of strain). This experiment reinforces the current model where temperature, dislocation density and mobility dictate serration behavior, but serrations are not directly linked to defect density.

6.2 Interstitially alloyed HEA

To verify the cryogenic serration phenomenon in an interstitially alloyed single-phase FCC material, a carbon containing HEA with composition $(Fe_{40}Ni_{11}Mn_{35}Al_8Cr_6)$-$C_1$ was investigated [132]. The alloy was prepared by vacuum arc melting and drop casting as specified in Ref. [133]. It was homogenized in an evacuated glass ampule at 1150 °C for 8 h. The alloy shows a very large grain size in the range of 100 µm. The single phase microstructure is depicted in Fig. 6.3. This alloy was subjected to a tensile test at 4.2 K. The resulting $\sigma_e - \varepsilon_e$ and $\Delta\sigma_e - \sigma_e$ curves are illustrated along with CoCrFeMnNi for comparison (Fig. 6.4). Two new observations, that were not seen for CoCrFeMnNi and

CoCrNi, are (i) ($Fe_{40}Ni_{11}Mn_{35}Al_8Cr_6$)-$C_1$ showed a high initial $\Delta\sigma_e$ and (ii) at high strains the $\Delta\sigma_e$ showed a decreasing trend (Fig. 6.4c).

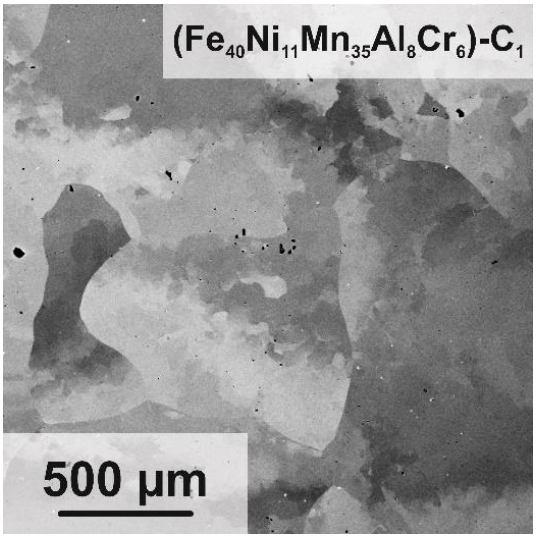

Figure 6.3: BSE orientation contrast image of ($Fe_{40}Ni_{11}Mn_{35}Al_8Cr_6$)-$C_1$ in the homogenized condition, annealed at 1150° C for 8 h.

The fractured specimen was subjected to SEM imaging and XRD analysis. BSE images in Fig. 6.5 show evidence of deformation twinning at 4.2 K. However, no martensite formation was observed (Fig. 6.6). The features seen in Fig. 6.5b appear to be microbands. Unlike, the deformation twins, the thickness of these features is in the range of a few 100 nm [134]. The electron channeling contrast in Fig. 6.5b also shows dislocation structures within these features, indicative of them being microbands. The SFE of ($Fe_{40}Ni_{11}Mn_{35}Al_8Cr_6$)-$C_1$ does not appear especially low based on the active deformation mechanisms. Correspondingly, the $\Delta\sigma_e$ should be less than that which is seen in Fig. 6.4b, especially with respect to CoCrFeMnNi. However, if the argument is restricted to difficulty of cross-slip (in the current model) instead of mobility of screw dislocation (based on Ref. [37, 91]) this result may be reasonable. Based on the effect of interstitial C, the cross-slip is made significantly more difficult, specifically through increased energy required for constriction of partial dislocations [135]. Thus, it would be reasonable that the most intense serrations are seen for an alloy with the greatest solute pinning effect.

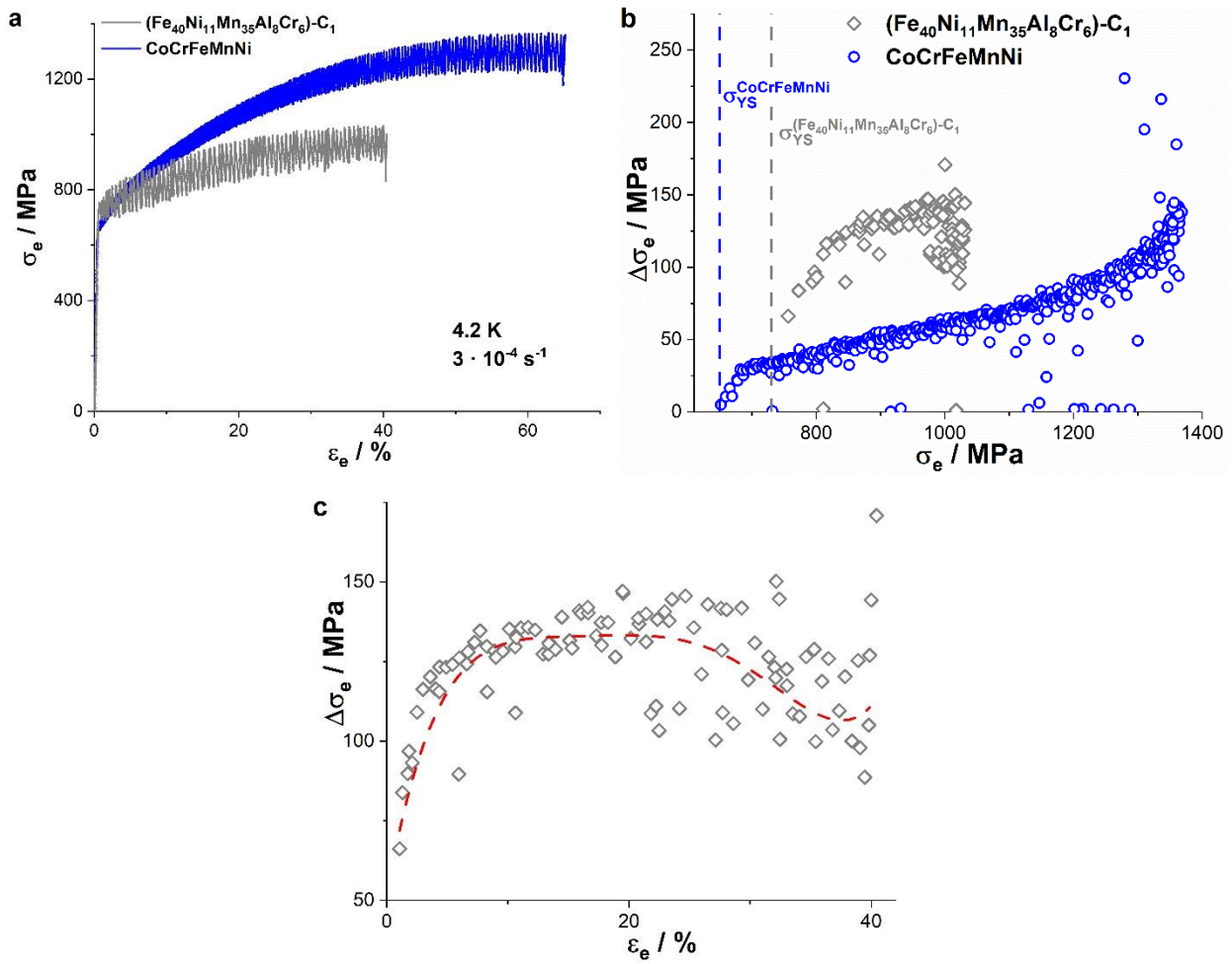

Figure 6.4: (a) $\sigma_e - \varepsilon_e$ for $(Fe_{40}Ni_{11}Mn_{35}Al_8Cr_6)$-$C_1$ and CoCrFeMnNi deformed at 4.2 K and (b) the corresponding $(\Delta\sigma_e - \sigma_e)$ plot. (c) The plot of $(\Delta\sigma_e - \varepsilon_e)$ for $(Fe_{40}Ni_{11}Mn_{35}Al_8Cr_6)$-$C_1$. The σ_{YS} for both alloys are marked as dotted lines in (b). The trend in (c) is indicated by the red dashed line.

The decreasing $\Delta\sigma_e$ is visualized clearly in Fig. 6.4c. This is a $\Delta\sigma_e - \varepsilon_e$ plot for $(Fe_{40}Ni_{11}Mn_{35}Al_8Cr_6)$-$C_1$ deformed at 4.2 K. The trend of the $\Delta\sigma_e - \varepsilon_e$, marked by the red dashed line, appears to decrease after $\varepsilon_e \sim 20\%$. This trend is non-intuitive. It contradicts the expected effect from increasing dislocation density. A possible reason is the activation of an additional carrier of plasticity which manifests sufficient strain in comparison to dislocation slip. However, the only additional deformation mechanism at these temperatures is that of deformation twinning, which is not expected to manifest a large proportion of the strain [21]. $(Fe_{40}Ni_{11}Mn_{35}Al_8Cr_6)$-$C_1$ is reported to have shown microband formation at RT

as well as at cryogenic temperatures. It is reportedly more prominent at lower temperature [136].

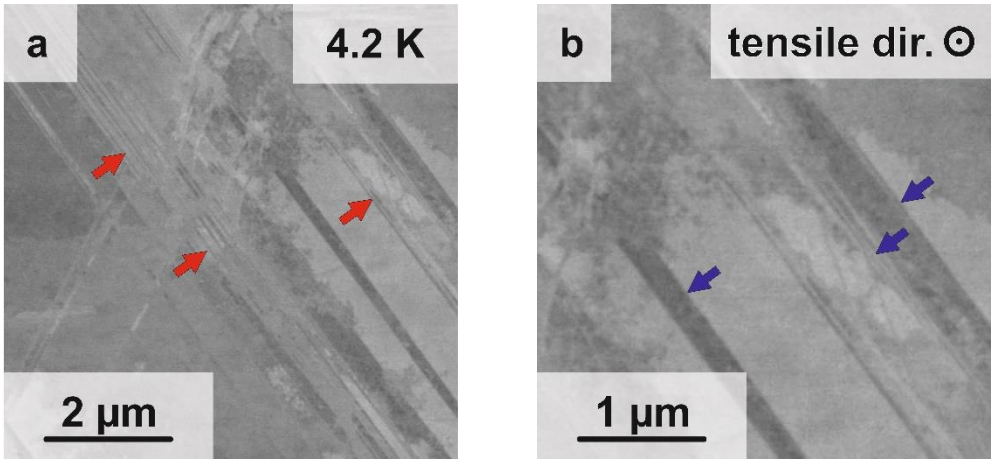

Figure 6.5: BSE orientation contrast images of ($Fe_{40}Ni_{11}Mn_{35}Al_8Cr_6$)-$C_1$ deformed at 4.2 K. (a) Micrograph showing deformation twins indicated by red arrows. (b) Micrograph showing microbands indicated by blue arrows. The loading direction is the same in both figures.

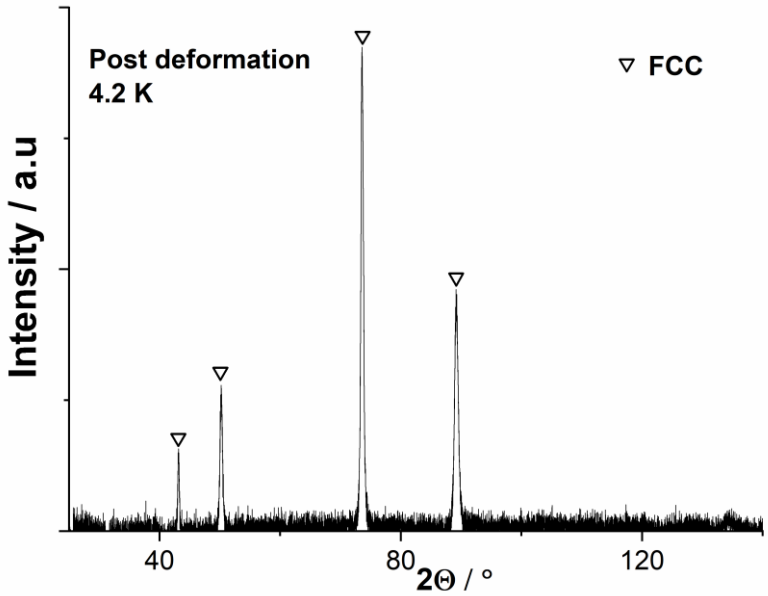

Figure 6.6: XRD analysis of ($Fe_{40}Ni_{11}Mn_{35}Al_8Cr_6$)-$C_1$ deformed at 4.2 K. The surface analyzed was longitudinal to the direction of tensile loading. The four peaks that were identified belong to the FCC crystal structure.

In the current case, dislocations pile-up at dense dislocation walls and the stress field serves to increase dislocation activity within the wall. This results in a splitting of the wall to form microbands [133, 134]. The microbands themselves have an associated width making it a volume defect rather than just a planar defect. Based on these observations, it is likely that the regions outside microbands keep decreasing in volume fraction with deformation. These regions are where dislocation interactions take place resulting in pile-ups at LC locks which ultimately lead to serrated plastic deformation. An increasing microband region (i) increases the chance of dislocation microband interaction as opposed to dislocation-dislocation interaction and (ii) increased dislocation activity within the microband. The stresses from the dislocations within the microband are screened due to low energy structures like cell blocks within the microband [137, 138]. Further analysis has to be done in order to verify this hypothesis but martensite formation in 304 stainless steel shows a similar trend as with $(Fe_{40}Ni_{11}Mn_{35}Al_8Cr_6)$-$C_1$ [36]. The $\Delta\sigma_e$decreases after the activation of TRIP in 304 stainless steel[5]. Martensite would also act as a volume defect as opposed to a planar defect. Once again, the glide region within the matrix decreases as martensite volume increases. Future work will be aimed at clarifying this point.

[5] This point was either not noticed or not addressed by the original authors

7 Summary

The current research investigated low temperature cryogenic deformation of CoCrFeMnNi and CoCrNi with a special focus on serrated plastic deformation. Over the course of the research work, multiple hypotheses stated in literature were tested and modified based on the results. These relate both, (i) to the active deformation mechanisms and their relative contribution to deformation characteristics, as well as (ii) to the proposed mechanisms for serrated plastic deformation.

Deformation characteristics of CoCrFeMnNi and CoCrNi were investigated at room and cryogenic temperatures to (i) establish the effect of temperature on deformation characteristics and (ii) verify previous hypotheses in relation to cryogenic deformation. Firstly, the approximate solid solution strengthening resulting from local lattice distortion, in CoCrNi and CoCrFeMnNi was compared through a $\sigma_{YS} - T$ variation. The results yielded fairly similar slopes indicating that CoCrNi possessed no distinct solid solution strengthening advantage in comparison to CoCrFeMnNi in the polycrystalline state, despite such an expectation based on previous results [11]. At RT, both alloys deform primarily through dislocation based plasticity but CoCrNi additionally shows deformation twinning. Both alloys reveal significant twinning at cryogenic temperatures, however. This deformation twinning proves to be the primary contributor to work-hardening during plastic deformation in both alloys. The deformation twinning itself was found to increase in propensity during deformation as a result of the increasing stress as well progressive grain rotation to achieve a higher fraction of grains that are texturally favorable for twinning.

Apart from the prevalent TWIP seen in these alloys, TRIP was also a significant point of interest. With respect to the same, despite the predicted activation of TRIP in CoCrFeMnNi at 4.2 K [28], no such transformation was found. CoCrFeMnNi only shows dislocation and twin based deformation at all temperatures between 295 and 4.2 K. In contrast, CoCrNi shows significant quantities of ε-martensite having been formed at twin boundaries at 8 K. However, despite the mass proliferation of ε-martensite on practically all twin boundaries there is no strengthening contribution from this behavior, contrary to the assertions in

Ref. [27]. The strengthening in both TWIP CoCrFeMnNi and TWIP + TRIP CoCrNi was the same.

At temperatures near 0 K, the appearance of intense serrated plastic deformation in CoCrFeMnNi was used as the basis of understanding of cryogenic serrated plastic deformation. Based on the analysis of deformation behavior already done it is clear that the serrated plastic deformation is not associated with a newly activated deformation mechanism at very low temperatures. Despite alternative expectations [95, 96], neither TWIP nor TRIP were critical requirements for this phenomenon. Serration behavior additionally went unaffected by varying heat dissipation parameters. This was contrary to the expected effect of localized thermal softening at these low temperatures [93]. Instead the cause was narrowed down to the activation of dislocation sources at the heads of pile-ups at LC locks. This model proposed using dislocation pile-ups at LC locks was a modification of the basis for serrations proposed by Seeger [91] and formerly validated by Obst and Nyilas [37]. However, while Ref. [37] provides a suitable interpretation of the original basis, it failed to explain the occurrence of mixed (continuous and discontinuous) deformation at certain temperatures. This is explained by the current model which provides a gradual transition for the instability condition based on dislocation density and temperature as opposed to discrete transition at different temperatures as formerly proposed in Ref. [37]. This model also circumnavigates the phenomenological problems faced when using the analytical solution for the gradual transition in instability condition provided in Ref. [99]. The model itself consists of dislocation proliferation that occurs as a result of inability of screw dislocations to cross-slip at low temperatures, for a variety of reasons. This leads to pile-up of dislocations, which, by virtue of the stress field generated at the head of the pile-up, activates a dislocation source which results in sudden dislocation motion of a massive number of dislocations. The corresponding result is of easy and massive dislocation motion, appearing as a stress drop/serration. This model thus (i) explains the cause for serrated plastic deformation, (ii) explains the reasons for transition from continuous to discontinuous deformation, (iii) explains the results previously published reports which have specified alternative hypotheses, and (iv) invalidates certain assertions of the former models.

8 Bibliography

[1] B. S. Murty, J. W. Yeh and S. Ranganathan, High-Entropy Alloys, Amsterdam, Boston, Heidelberg, London, New York, Oxford, Paris, San Diego, San Francisco, Singapore, Sydney, Tokyo: Elsevier, 2014.

[2] D. B. Miracle and O. N. Senkov, "A critical review of high entropy alloys and related concepts," *Acta Materialia,* vol. 122, pp. 448 - 511, 2017.

[3] J.-W. Yeh, "Physical Metallurgy of High-Entropy Alloys," *JOM,* vol. 67, pp. 2254 - 2261, 2015.

[4] J.-W. Yeh, Y.-L. Chen, S.-J. Lin and S.-K. Chen, "High-Entropy Alloys – A New Era of Exploitation," *Materials Science Forum,* vol. 560, pp. 1 - 9, 2007.

[5] E. P. George, D. Raabe and R. O. Ritchie, "High-entropy alloys," *Nature Reviews Materials,* vol. 4, pp. 515 - 534, 2019.

[6] D. B. Miracle, "Critical Assessment 14: High entropy alloys and their development as structural materials," *Materials Science and Technology,* vol. 31, pp. 1142 - 1147, 2015.

[7] D. B. Miracle, J. D. Miller, O. N. Senkov, C. Woodward, M. D. Uchic and J. Tiley, "Exploration and Development of High Entropy Alloys for Structural Applications," *Entropy,* vol. 16, pp. 494 - 525, 2014.

[8] Y. F. Ye, Y. H. Zhang, Q. F. He, Y. Zhuang, S. Wang, S. Q. Shi, A. Hu, J. Fan and Y. Yang, "Atomic-scale distorted lattice in chemically disordered equimolar complex alloys," *Acta Materialia,* vol. 150, pp. 182 - 194, 2018.

[9] B. Cantor, I. T. H. Chang, P. Knight and A. J. B. Vincent, "Microstructural development in equiatomic multicomponent alloys," *Materials Science and Engineering: A,* Vols. 375 - 377, pp. 213 - 218, 2004.

[10] Z. Wu, H. Bei, F. Otto, G. Pharr and E. George, "Recovery, recrystallization, grain growth and phase stability of a family of FCC-structured multi-component equiatomic solid solution alloys," *Intermetallics,* vol. 46, pp. 131 - 140, 2014.

[11] Z. Wu, H. Bei, G. Pharr and E. George, "Temperature dependence of the mechanical properties of equiatomic solid solution alloys with face-centered cubic crystal structures," *Acta Materialia,* vol. 81, pp. 428 - 441, 2014.

[12] F. Otto, A. Dlouhý, C. Somsen, H. Bei, G. Eggeler and E. P. George, "The influences of temperature and microstructure on the tensile properties of a CoCrFeMnNi high-entropy alloy," *Acta Materialia,* vol. 61, no. 15, pp. 5743 - 5755, 2013.

[13] B. Gludovatz, A. Hohenwarter, K. V. S. Thurston, H. Bei, Z. Wu, E. P. George and R. O. Ritchie, "Exceptional damage-tolerance of a medium-entropy alloy CrCoNi at cryogenic temperatures," *Nature Communications,* vol. 7, pp. 1 - 8 (Art. no. 10602), 2016.

[14] G. Laplanche, A. Kostka, C. Reinhart, J. Hunfeld, G. Eggeler and E. P. George, "Reasons for the superior mechanical properties of medium-entropy CrCoNi compared to high-entropy CrMnFeCoNi," *Acta Materialia,* vol. 128, pp. 292 - 303, 2017.

[15] O. N. Senkov, J. M. Scott, S. V. Senkova, D. B. Miracle and C. Woodward, "Microstructure and room temperature properties of a high-entropy TaNbHfZrTi alloy," *Journal of Alloys and Compounds,* vol. 509, no. 20, pp. 6043 - 6048, 2011.

[16] J. P. Couzinié, G. Dirras, L. Perrière, T. Chauveau, E. Leroy, Y. Champion and I. Guillot, "Microstructure of a near-equimolar refractory high-entropy alloy," *Materials Letters,* vol. 126, pp. 285 - 287, 2014.

[17] J. P. Couzinié, L. Lilensten, Y. Champion, G. Dirras, L. Perrière and I. Guillot, "On the room temperature deformation mechanisms of a TiZrHfNbTa refractory high-entropy alloy," *Materials Science & Engineering A,* vol. 645, pp. 255 - 263, 2015 .

[18] G. Dirras, H. Couque, L. Lilensten, A. Heczel, D. Tingaud, J.-P. Couzinié, L. Perrière, J. Gubicza and I. Guillot, "Mechanical behavior and microstructure of Ti20Hf20Zr20Ta20Nb20 high-entropy alloy loaded under quasi-static and dynamic compression conditions," *Materials Characterization,* vol. 111, pp. 106 - 113, 2016.

[19] L. Lilensten, J. P. Couzinié, L. Perrière, A. Hocini, C. Keller, G. Dirras and I. Guillot, "Study of a bcc multi-principal element alloy: Tensile and simple shear properties and underlying deformation mechanisms," *Acta Materialia,* vol. 142, pp. 131 - 141, 2018.

[20] F. Otto, N. L. Hanold and E. P. George, "Microstructural evolution after thermomechanical processing in an equiatomic, single-phase CoCrFeMnNi high-entropy alloy with special focus on twin boundaries," *Intermetallics,* vol. 54, pp. 39 - 48, 2014.

[21] G. Laplanche, A. Kostka, O. Horst, G. Eggeler and E. P. George, "Microstructure evolution and critical stress for twinning in the CrMnFeCoNi high-entropy alloy," *Acta Materialia,* vol. 118, pp. 152 - 163, 2016.

[22] A. J. Zaddach, C. Niu, C. C. Koch and D. L. Irving, "Mechanical Properties and Stacking Fault Energies of NiFeCrCoMn High-Entropy Alloy," *JOM,* vol. 65, pp. 1780 - 1789, 2013.

[23] B. Gludovatz, E. P. George and R. O. Ritchie, "Processing, Microstructure and Mechanical Properties of the CrMnFeCoNi High-Entropy Alloy," *JOM,* vol. 67, pp. 2262 - 2270, 2015.

[24] S. Curtze and V.-T. Kuokkala, "Dependence of tensile deformation behavior of TWIP steels on stacking fault energy, temperature and strain rate," *Acta Materialia,* vol. 58, no. 15, pp. 5129 - 5141, 2010.

[25] R. Kalsar, P. Khandal and S. Suwas, "Effects of Stacking Fault Energy on Deformation Mechanisms in Al-Added Medium Mn TWIP Steel," *Metallurgical and Materials Transactions A,* vol. 50, pp. 3683 - 3696, 2019.

[26] J.-K. Kim and B. C. De Cooman, "Stacking fault energy and deformation mechanisms in Fe-xMn-0.6C-yAl TWIP steel," *Materials Science & Engineering A,* vol. 676, pp. 216 - 231 , 2016.

[27] J. Miao, C. Slone, T. Smith, C. Niu, H. Bei, M. Ghazisaeidi, G. M. Pharr and M. J. Mills, "The evolution of the deformation substructure in a Ni-Co-Cr equiatomic solid solution alloy," *Acta Materialia,* vol. 132, pp. 35 - 48, 2017.

[28] S. Huang, W. Li, S. Lu, F. Tian, J. Shen, E. Holmström and L. Vitos, "Temperature dependent stacking fault energy of FeCrCoNiMn high entropy alloy," *Scripta Materialia,* vol. 108, pp. 44 - 47, 2015.

[29] A. S. Tirunilai, J. Sas, K.-P. Weiss, H. Chen, D. V. Szabó, S. Schlabach, S. Haas, D. Geissler, J. Freudenberger, M. Heilmaier and A. Kauffmann, "Peculiarities of deformation of CoCrFeMnNi at cryogenic temperatures," *Journal of Materials Research,* vol. 33, no. 19, pp. 3287 - 3300, 2018.

[30] A. S. Tirunilai, T. Hanemann, C. Reinhart, V. Tschan, K.-P. Weiss, G. Laplanche, J. Freudenberger, M. Heilmaier and A. Kauffmann, "Comparison of cryogenic deformation of the concentrated solid solutions CoCrFeMnNi, CoCrNi and CoNi," *Materials Science and Engineering: A,* vol. 783, pp. 1 - 10 (Art. no. 139290), 2020.

[31] A. S. Tirunilai, T. Hanemann, K.-P. Weiss, J. Freudenberger, M. Heilmaier and A. Kauffmann, "Dislocation-based serrated plastic flow of high entropy alloys at cryogenic temperatures," *Acta Materialia,* vol. 200, pp. 980 - 991, 2020.

[32] A. H. Cottrell, "LXXXVI. A note on the Portevin-Le Chatelier effect," *Philosophical Magazine,* vol. 44, pp. 829 - 832, 1953.

[33] A. Yilmaz, "The Portevin–Le Chatelier effect: a review of experimental findings," *Science and Technology of Advanced Materials,* vol. 12, pp. 1 - 16 (Art. no. 063001), 2011.

[34] A. V. D. Beukel, "Theory of the Effect of Dynamic Strain Aging on Mechanical Properties," *Physica Status Solidi A,* vol. 30, no. 197, pp. 197 - 206, 1975.

[35] V. V. Pustovalov, "Serrated deformation of metals and alloys at low temperatures," *Low Temperature Physics,* vol. 34, pp. 683 - 723, 2008.

[36] J. Tabin, B. Skoczen and J. Bielski, "Strain localization during discontinuous plastic flow at extremely low temperatures," *International Journal of Solids and Structures,* Vols. 97 - 98 , pp. 593 - 612, 2016.

[37] B. Obst and A. Nyilas, "Experimental evidence on the dislocation mechanism of serrated yielding in f.c.c. metals and alloys at low temperatures," *Materials Science and Engineering: A,* vol. 137, pp. 141 - 151, 1991.

[38] T. Ogata, K. Ishikawa, K. Hiraga, K. Nagai and T. Yuri, "Temperature rise during the tensile test in superfluid helium," *Cryogenics,* vol. 25, no. 8, pp. 444 - 446, 1985.

[39] T. Ogata, T. Yuri and Y. Ono, "Review of specimen heating in mechanical tests at cryogenic temperatures," *AIP Conference Proceedings,* vol. 1574, no. 86, pp. 86 - 91, 2014.

[40] J. Sas, K.-P. Weiss and N. Bagrets, "CryoMaK – the Overview of Cryogenic Testing Facilities in Karlsruhe," *Acta Metallurgica Slovaca,* vol. 21, no. 4, pp. 330-338, 2015.

[41] P. Bhattacharjee, G. Sathiaraj, M. Zaid, J. Gatti, C. Lee, C.-W. Tsai and J.-W. Yeh, "Microstructure and texture evolution during annealing of equiatomic CoCrFeMnNi high-entropy alloy," *Journal of Alloys and Compounds,* vol. 587, pp. 544 - 552, 2014.

[42] G. Laplanche, O. Horst, F. Otto, G. Eggeler and E. P. George, "Microstructural evolution of a CoCrFeMnNi high-entropy alloy after swaging and annealing," *Journal of Alloys and Compounds,* vol. 647, pp. 548 - 557, 2015.

[43] A. Srinivasan, A. Kauffmann, J. Sas, K.-P. Weiss, H. Chen, M. Heilmaier and J. Freudenberger, "Peculiarities of deformation of CoCrFeMnNi at very low tempearture," *DFG SPP 1st General Meeting, Hannover,* pp. 1-11 (https://www.sppccahea.uni-bayreuth.de/pool/dokumente/KA-4631_1.pdf), 2017.

[44] F. Otto, A. Dlouhý, K. G. Pradeep, M. Kuběnová, D. Raabe, G. Eggeler and E. P. George, "Decomposition of the single-phase high-entropy alloy CrMnFeCoNi after prolonged anneals at intermediate temperatures," *Acta Materialia,* vol. 112, pp. 40 - 52, 2016.

[45] E. J. Pickering, R. Muñoz-Moreno, H. J. Stone and N. G. Jones, "Precipitation in the equiatomic high-entropy alloy CrMnFeCoNi," *Scripta Materialia,* vol. 113, pp. 106 - 109, 2016.

[46] J. Ding, Q. Yu, M. Asta and R. O. Ritchie, "Tunable stacking fault energies by tailoring local chemical order in CrCoNi medium-entropy alloys," *Proceedings of the National Academy of Sciences of the United States of America,* vol. 115, no. 36, pp. 8919 - 8924, 2018.

[47] Q.-J. Li, H. Sheng and E. Ma, "Strengthening in multi-principal element alloys with local-chemical-order roughened dislocation pathways," *Nature Communications,* vol. 10, pp. 1 - 11 (Art. no. 3563), 2019.

[48] R. Zhang, S. Zhao, J. Ding, Y. Chong, T. Jia, C. Ophus, M. Asta, R. O. Ritchie and A. M. Minor, "Short-range order and its impact on the CrCoNi medium-entropy alloy," *Nature,* vol. 581, pp. 283 - 287, 2020.

[49] B. Yin, S. Yoshida, N. Tsuji and W. A. Curtin, "Yield strength and misfit volumes of NiCoCr and implications for short-range-order," *Nature Communications,* vol. 11, pp. 1 - 7 (Art. no. 2507), 2020.

[50] S. I. Hong, J. Moon, S. K. Hong and H. S. Kim, "Thermally activated deformation and the rate controlling mechanism in CoCrFeMnNi high entropy alloy," *Materials Science and Engineering: A,* vol. 682, pp. 569 - 576, 2017.

[51] G. Laplanche, J. Bonneville, C. Varvenne, W. Curtin and E. P. George, "Thermal activation parameters of plastic flow reveal deformation mechanisms in the CrMnFeCoNi high-entropy alloy," *Acta Materialia,* vol. 143, pp. 257 - 264, 2018.

[52] S. Allain, J.-P. Chateau, O. Bouaziz, S. Migot and N. Guelton, "Correlations between the calculated stacking fault energy and the plasticity mechanisms in Fe-Mn-C alloys," *Materials Science and Engineering: A,* Vols. 387 - 389, pp. 158 - 162, 2004.

[53] C. Niu, C. R. LaRosa, J. Miao, M. J. Mills and M. Ghazisaeidi, "Magnetically-driven phase transformation strengthening in high entropy alloys," *Nature Communications,* vol. 9, pp. 1 - 9 (Art. no. 1363), 2018.

[54] C. E. Slone, S. Chakraborty, J. Miao, E. P. George, M. J. Mills and S. R. Niezgoda, "Influence of deformation induced nanoscale twinning and FCC-HCP transformation on hardening and texture development in medium entropy CrCoNi alloy," *Acta Materialia,* vol. 158, pp. 38 - 52, 2018.

[55] M. Schneider, E. George, T. Manescau, T. Záležák, J. Hunfeld, G. E. A. Dlouhý and G. Laplanche, "Analysis of strengthening due to grain boundaries and annealing twin boundaries in the CrCoNi medium-entropy alloy," *International Journal of Plasticity,* vol. 124, pp. 155 - 169, 2020.

[56] Z. C. Cordero, B. E. Knight and C. A. Schuh, "Six decades of the Hall–Petch effect – a survey of grain-size strengthening studies on pure metals," *International Materials Reviews,* vol. 61, no. 8, pp. 495 - 512, 2016.

[57] R. Labusch, "A Statistical Theory of Solid Solution Hardening," *Physica Status Solidi A,* vol. 41, pp. 659 - 669, 1970.

[58] C. Varvenne, A. Luque and W. A. Curtin, "Theory of strengthening in fcc high entropy alloys," *Acta Materialia,* vol. 118, pp. 164-176, 2016.

[59] G. P. M. Leyson and W. A. Curtin, "Friedel vs. Labusch: the strong/weak pinning transition in solute strengthened metals," *Philosophical Magazine,* vol. 93, no. 19, pp. 2428 - 2444, 2013.

[60] C. R. LaRosa, M. Shih, C. Varvenne and M. Ghazisaeidi, "Solid solution strengthening theories of high-entropy alloys," *Materials Characterization,* vol. 151, pp. 310 - 317, 2019.

[61] L. Owen, E. Pickering, H. Playford, H. Stone, M. Tucker and N. Jones, "An assessment of the lattice strain in the CrMnFeCoNi high-entropy alloy," *Acta Materialia,* vol. 122, pp. 11 - 18, 2017.

[62] H. S. Oh, D. Ma, G. P. Leyson, B. Grabowski, E. S. Park, F. Körmann and D. Raabe, "Lattice Distortions in the FeCoNiCrMn High Entropy Alloy Studied by Theory and Experiment," *Entropy,* vol. 18, no. 9, pp. 321 - 329, 2016.

[63] N. L. Okamoto, K. Yuge, K. Tanaka, H. Inui and E. P. George, "Atomic displacement in the CrMnFeCoNi high-entropy alloy – A scaling factor to predict solid solution strengthening," *AIP Advances,* vol. 6, no. 12, pp. 1 - 8 (Art. no. 125008), 2016.

[64] H. Chen, A. Kauffmann, S. Laube, I.-C. Choi, R. Schwaiger, Y. Huang, K. Lichtenberg, F. Müller, B. Gorr, H.-J. Christ and M. Heilmaier, "Contribution of Lattice Distortion to Solid Solution Strengthening in a Series of Refractory High Entropy Alloys," *Metallurgical and Materials Transactions A,* vol. 49, pp. 772 - 781, 2018.

[65] A. Haglund, M. Koehler, D. Catoor, E. P. George and V. Keppens, "Polycrystalline elastic moduli of a high-entropy alloy at cryogenic temperatures," *Intermetallics,* vol. 58, pp. 62 - 64, 2015.

[66] G. Laplanche, O. Horst, P. Gadaud, F. Otto, G. Eggeler and E. P. George, "Temperature dependencies of the elastic moduli and thermal expansion coefficient of an equiatomic, single-phase CoCrFeMnNi high-entropy alloy," *Journal of Alloys and Compounds,* vol. 623, pp. 348 - 353, 2015.

[67] G. Laplanche, P. Gadaud, C. Bärsch, K. Demtröder, C. Reinhart, J. Schreuer and E. George, "Elastic moduli and thermal expansion coefficients of medium-entropy subsystems of the CrMnFeCoNi high-entropy alloy," *Journal of Alloys and Compounds,* vol. 746, pp. 244 - 255, 2018.

[68] H. Bahmanpour, A. Kauffmann, M. S. Khoshkhoo, K. M. Youssef, S. Mula, J. Freudenberger, J. Eckert, R. O. Scattergood and C. C. Koch, "Effect of stacking fault energy on deformation behavior of cryo-rolled copper and copper alloys," *Materials Science and Engineering: A,* vol. 529, pp. 230 - 236, 2011.

[69] N. L. Okamoto, S. Fujimoto, Y. Kambara, M. Kawamura, Z. M. T. Chen, H. Matsunoshita, K. Tanaka, H. Inui and E. P. George, "Size effect, critical resolved shear stress, stacking fault energy, and solid solution strengthening in the CrMnFeCoNi high-entropy alloy," *Scientific Reports,* vol. 6, pp. 1 - 10 (Art. no. 35863), 2016.

[70] Z.-H. Jin, P. Gumbsch, E. Ma, K. Albe, K. Lu, H. Hahn and H. Gleiter, "The interaction mechanism of screw dislocations with coherent twin boundaries in different face-centred cubic metals," *Scripta Materialia,* vol. 54, no. 6, pp. 1163 - 1168, 2006.

[71] Z.-H. Jin, P. Gumbsch, K. Albe, E. Ma, K. Lu, H. Gleiter and H. Hahn, "Interactions between non-screw lattice dislocations and coherent twin boundaries in face-centered cubic metals," *Acta Materialia,* vol. 56, no. 5, pp. 1126 - 1135, 2008.

[72] T. Ezaz, M. D. Sangid and H. Sehitoglu, "Energy barriers associated with slip–twin interactions," *Philosophical Magazine,* vol. 91, no. 10, pp. 1464 -1488, 2011.

[73] L. Rémy, "Twin-Slip interaction in F.C.C. Crystals," *Acta Metallurgica,* vol. 25, no. 6, pp. 711 - 714, 1977.

[74] S. Mahajan and G. Y. Chin, "Twin-slip, twin-twin and slip-twin interactions in Co-8 wt.% Fe alloy single crystals," *Acta Metallurgica,* vol. 21, no. 2, pp. 173 - 179, 1973.

[75] S. Asgari, E. El-Danaf, S. R. Kalidindi and R. D. Doherty, "Strain Hardening Regimes and Microstructural Evolution during Large Strain Compression of Low Stacking Fault Energy FCC Alloys That Form Deformation Twins," *Metallurgical and Materials Transactions A,* vol. 28, pp. 1781 - 1795, 1997.

[76] I. Gutierrez-Urrutia and D. Raabe, "Dislocation and twin substructure evolution during strain hardening of an Fe–22 wt.% Mn–0.6 wt.% C TWIP steel observed by electron channeling contrast imaging," *Acta Materialia,* vol. 59, no. 16, pp. 6449 - 6462, 2011.

[77] T. H. Blewitt, R. R. Coltman and J. K. Redman, "Low-Temperature Deformation of Copper Single Crystals," *Journal of Applied Physics,* vol. 28, pp. 651 - 661, 1957.

[78] T. E. Mitchell and P. R. Thornton, "The work-hardening characteristics of Cu and α-brass single crystals between 4•2 and 500°K," *The Philosophical Magazine,* vol. 8, no. 91, pp. 1127 - 1159, 1963.

[79] D. Weiner, "Mechanical twinning in Cu single crystals," *Acta Metallurgica,* vol. 20, no. 10, pp. 1235 - 1239, 1972.

[80] A. Kauffmann, "Gefügeverfeinerung durch mechanische Zwillingsbildung in Kupfer und Kupfermischkristalllegierungen," *Dissertation, Technische Universität Dresden,* 2014.

[81] S. M. Copley and B. H. Kear, "The dependence of the width of a dissociated dislocation on dislocation velocity," *Acta Metallurgica,* vol. 16, no. 2, pp. 227 - 231 , 1968.

[82] A. Kauffmann, J. Freudenberger, H. Klauß, V. Klemm, W. Schillinger, V. S. Sarma and L. Schultz, "Properties of cryo-drawn copper with severely twinned microstructure," *Materials Science and Engineering: A,* vol. 588, pp. 132 - 141, 2013.

[83] A. Kauffmann, J. Freudenberger, H. Klauß, W. Schillinger, V. S. Sarma and L. Schultz, "Efficiency of the refinement by deformation twinning in wire drawn single phase copper alloys," *Materials Science and Engineering: A,* vol. 624, pp. 71 - 78, 2015.

[84] A. Kauffmann, J. Freudenberger, D. Geissler, S. Yin, W. Schillinger, V. S. Sarma, H. Bahmanpour, R. Scattergood, M. Khoshkhoo, H. Wendrock, C. Koch, J. Eckert and L. Schultz, "Severe deformation twinning in pure copper by cryogenic wire drawing," *Acta Materialia,* vol. 59, no. 20, pp. 7816-7823, 2011.

[85] G. I. Taylor, "Plastic Strain in Metals," *Journal of the Institute of Metals ,* vol. 62, pp. 307 - 324 , 1938.

[86] J. A. Venables, "Deformation twinning in face-centred cubic metals," *Philosophical Magazine,,* vol. 6, no. 63, pp. 379 - 396, 1961.

[87] M. Koyama, T. Sawaguchi, T. Lee, C. S. Lee and K. Tsuzaki, "Work hardening associated with ε-martensitic transformation, deformation twinning and dynamic strain aging in Fe–17Mn–

0.6C and Fe–17Mn–0.8C TWIP steels," *Materials Science and Engineering: A,* vol. 528, no. 24, pp. 7310 - 7316, 2011.

[88] G. B. Olson and M. Cohen, "A general mechanism of martensitic nucleation: Part I. General concepts and the FCC - HCP transformation," *Metallurgical Transactions A,* vol. 7, pp. 1897 - 1904, 1976.

[89] S. Chen, H. Oh, B. Gludovatz, S. J. Kim, E. S. Park, Z. Zhang, R. O. Ritchie and Q. Yu, "Real-time observations of TRIP-induced ultrahigh strain hardening in a dual-phase CrMnFeCoNi high-entropy alloy," *Nature Communications,* vol. 2020, pp. 1 - 8 (Art. no. 128), 11.

[90] A. N. Stroh, "A theory of the fracture of metals," *Advances in Physics,* vol. 6, no. 24, pp. 418 - 465, 1957.

[91] A. Seeger, "The mechanism of glide and work hardening in Face-Centered Cubic and Hexagonal-Close Packed metals," in *Dislocations and Mechanical Properties of Crystals*, New York, John Wiley & Sons, Inc., 1958, pp. 243 - 330.

[92] P. Haasen, "Plastic deformation of nickel single crystals at low temperatures," *Philosophical Magazine,* vol. 3, no. 28, pp. 384-418, 1958.

[93] Z. Basinski, "The instability of plastic flow of metals at very low temperatures," *Proceedings of the Royal Society A,* vol. 240, no. 1221, pp. 354 - 358, 1957.

[94] Z. S. Basinski, "The Instability of Plastic Flow of Metals at Very Low Temperatures. II," *Australian Journal of Physics,* vol. 13, no. 2, pp. 354 - 358, 1960.

[95] W. Han, Y. Liu, F. Wan, P. Liu, X. Yi, Q. Zhan, D. Morrall and S. Ohnuki, "Deformation behavior of austenitic stainless steel at deep cryogenic temperatures," *Journal of Nuclear Materials,* vol. 504, pp. 29 - 32 , 2018.

[96] J. Liu, X. Guo, Q. Lin, Z. He, X. An, L. Li, P. K. Liaw, X. Liao, L. Yu, J. Lin, L. Xie, J. Ren and Y. Zhang, "Excellent ductility and serration feature of metastable CoCrFeNi high-entropy alloy at extremely low temperatures," *Science China Materials,* vol. 62, no. 6, pp. 853 - 863, 2018.

[97] R. Zürecher, V. Gröger and F. Stangler, "Discontinuous Flow in Cu-Be2 between 4.2 and 12.5 K," *Physica Status Solidi A,* vol. 84, pp. 475 - 480, 1984.

[98] R. B. Schwarz and R. Labusch, "Dynamic simulation of solution hardening," *Journal of Applied Physics,* vol. 49, no. 10, pp. 5174 - 5187, 1978.

[99] B. Skoczeń, J. Bielski, S. Sgobba and D. Marcinek, "Constitutive model of discontinuous plastic flow at cryogenic temperatures," *International Journal of Plasticity,* vol. 26, no. 12, pp. 1659 - 1679, 2010.

[100] M. Tufano, C. Zauner and A. Morasch, "Innovative setup for cryogenic mechanical testing of high-strength metallic alloys," *CEAS Space Journal,* vol. 11, pp. 241 - 246, 2019.

[101] R. Gröger, V. Vitek and A. Dlouhý, "Effective pair potential for random fcc CoCrFeMnNi alloys," *Modelling and Simulation in Materials Science and Engineering,* vol. 28, pp. 1 - 25 (Art. no. 075006), 2020.

[102] K. Jin, B. C. Sales, G. M. Stocks, G. D. Samolyuk, M. Daene, W. J. Weber, Y. Zhang and H. Bei, "Tailoring the physical properties of Ni-based single-phase equiatomic alloys by modifying the chemical complexity," *Scientific Reports,* vol. 6, pp. 1 - 10 (Art. no. 20159), 2016.

[103] K. Jin, S. Mu, K. An, W. Porter, G. Samolyuk, G. Stocks and H. Bei, "Thermophysical properties of Ni-containing single-phase concentrated solid solution alloys," *Materials & Design,* vol. 117, pp. 185 - 192, 2017.

[104] A. L. Woodcraft, "Predicting the thermal conductivity of aluminium alloys in the cryogenic to room temperature range," *Cryogenics,* vol. 45, no. 6, pp. 421 - 431, 2005.

[105] V. A. Strizhalo, V. Y. Bugaev and M. I. I., "Effect of Strain rate on features of discontinuous flow for titanium alloys under static tension conditions at 4.2 K," *Strength of Materials,* vol. 22, no. 35, pp. 1279 - 1283 (Translated from Problemy Prochnosti), 1990.

[106] J. P. Hirth and J. Lothe, "Glide of jogged dislocations," in *Theory of dislocations*, New York, St. Louis, San Francisco, Toronto, London, Sydney, McGraw-Hill Book Company, 1968, pp. 535 - 556.

[107] A. Seeger, "CXXXII. The generation of lattice defects by moving dislocations, and its application to the temperature dependence of the flow-stress of F.C.C. crystals," *The London, Edinburgh, and Dublin Philosophical Magazine and Journal of Science,* vol. 46, no. 382, pp. 1194 - 1217, 1955.

[108] B. Skoczeń, J. Bielski and J. Tabin, "Multiaxial constitutive model of discontinuous plastic flow at cryogenic temperatures," *International Journal of Plasticity,* vol. 55, pp. 198 - 218, 2014.

[109] B. Obst and D. Pattanayak, "Discontinuous deformation modes of nitrogen-stabilized austenitic steel," in *Advances in Cryogenic Engineering Materials 28*, New York, Plenum Press, 1982, pp. 57 - 65.

[110] J. Tabin, B. Skoczen and J. Bielski, "Discontinuous plastic flow coupled with strain induced fcc–bcc phase transformation at extremely low temperatures," in *Mechanics of Materials*, 129, 2019, pp. 23 - 40.

[111] B. S. Gottfried, C. J. Lee and K. J. Bell, "The leidenfrost phenomenon : film boiling of liquid droplets on a flat plate," *International Journal of Heat and Mass Transfer,* vol. 9, no. 11, pp. 1167 - 1188, 1966.

[112] S. N. Komnik and V. V. Demirski, "Study of the instability boundaries of plastic flow in Cu + 14 at.% Al single crystals at low temperatures," *Crystal Research & Technology,* vol. 19, no. 6, pp. 863 - 872, 1984.

[113] R. B. Schwarz and J. W. Mitchell, "Dynamic dislocation phenomena in single crystals of Cu-10.5-at. %-Al alloys at 4.2 K," *Physical Review B,* vol. 9, no. 8, pp. 3292 - 3299, 1974.

[114] J. Bouquerel, K. Verbeken and B. C. De Cooman, "Microstructure-based model for the static mechanical behaviour of multiphase steels," *Acta Materialia,* vol. 54, no. 6, pp. 1443 - 1456, 2006.

[115] A. Seeger, J. Diehl, S. Mader and H. Rebstock, "Work-hardening and work-softening of face centred cubic metal crystals," *Philosophical Magazine,* vol. 2, no. 15, pp. 323 - 350, 1957.

[116] M. S. Duesbery, N. P. Louat and K. Sadananda, "The mechanics and energetics of cross-slip," *Acta Metallurgica et Materialia,* vol. 40, no. 1, pp. 149 - 158, 1992.

[117] J. Bonneville and B. Escaig, "Cross-slipping process and the stress-orientation dependence in pure copper," *Acta Metallurgica,* vol. 27, no. 9, pp. 1477 - 1486 , 1979.

[118] C. Jin, Y. Xiang and G. Lu, "Dislocation cross-slip mechanisms in aluminum," *Philosophical Magazine,* vol. 91, no. 32, pp. 4109 - 4125, 2011.

[119] J. Marian, J. Knap and M. Ortiz, "Nanovoid deformation in aluminum under simple shear," *Acta Materialia,* vol. 53, no. 10, pp. 2893 - 2900, 2005.

[120] P. B. Hirsch, "Extended Jogs in Dislocations in Face-centred Cubic Metals," *The Philosophical Magazine: A Journal of Theoretical Experimental and Applied Physics,* vol. 7, no. 73, pp. 67 - 93, 1962.

[121] Z. Pu, Z. C. Xie, R. Sarmah, Y. Chen, C. Lu, G. Ananthakrishna and L. H. Dai, "Spatio-temporal dynamics of jerky flow in high-entropy alloy at extremely low temperature," *Philosophical Magazine,* vol. 101, no. 2, pp. 154 - 178, 2020.

[122] X. Zhang, "A continuum model for dislocation pile-up problems," *Acta Materialia,* vol. 128, pp. 428 - 439, 2017.

[123] B. Pan, Y. Shibutani, X. Zhang and F. Shang, "Effect of dislocation pile-up on size-dependent yield strength in finite single-crystal micro-samples," *Journal of Applied Physics,* vol. 118, no. 1, pp. 1 - 8 (Art. no. 014305), 2015.

[124] S. I. Hong and C. Laird, "Mechanisms of slip mode modification in F.C.C. solid solutions," *Acta Metallurgica et Materialia,* vol. 38, no. 8, pp. 1581 - 1594, 1990.

[125] A. Benallal, T. Berstad, T. Børvik, O. S. Hopperstad and R. Nogueira de Codes, "Effects of strain rate on the characteristics of PLC deformation bands for AA5083-H116 aluminium alloy," *Philosophical Magazine,* vol. 88, no. 28 - 29, pp. 3311 - 3338, 2008.

[126] D. Canadinc, C. Efstathiou and H. Sehitoglu, "On the negative strain rate sensitivity of Hadfield steel," *Scripta Materialia,* vol. 59, no. 10, pp. 1103 - 1106, 2008.

[127] V. N. Kovaleva and V. A. Moskalenko, "Quality of surface treatment and plastic deformation of titanium alloys at 2.5 to 293 K," *Cryogenics,* vol. 29, no. 10, pp. 1002 - 1005, 1989.

[128] K. Nagai, T. Yuri, Y. Nakasone, T. Ogata and K. Ishikawa, "Effects of gage diameter and strain rate on tensile deformation behavior of 32Mn-7Cr steel at 4 K," in *Advances in Cryogenic Engineering Materials 32*, New York and London, Plenum Press, 1986, pp. 313 - 320.

[129] A. S. Argon, Strengthening Mechanisms in Crystal Plasticity, New York: Oxford University Press, 2008.

[130] K. Kamada and I. Yoshizawa, "The Anomalies in Temperature Dependence of the Yield Stress of Cu Base Solid Solutions," *Journal of the Physical Society of Japan,* vol. 31, no. 4, pp. 1056 - 1068, 1971.

[131] T. M. Smith, M. S. Hooshmand, B. D. Esser, F. Otto, D. W. McComb, E. P. George, M. Ghazisaeidi and M. J. Mills, "Atomic-scale characterization and modeling of 60° dislocations in a high-entropy alloy," *Acta Materialia,* vol. 110, pp. 352 - 363, 2016.

[132] Z. Wang and I. Baker, "Interstitial strengthening of a f.c.c. FeNiMnAlCr high entropy alloy," *Materials Letters,* vol. 180, pp. 153 - 156, 2016.

[133] Z. Wang, I. Baker, Z. Cai, S. Chen, J. D. Poplawsky and W. Guo, "The effect of interstitial carbon on the mechanical properties and dislocation substructure evolution in Fe40.4Ni11.3Mn34.8Al7.5Cr6 high entropy alloys," *Acta Materialia,* vol. 120, pp. 228 - 239, 2016.

[134] I. Gutierrez-Urrutia and D. Raabe, "Microbanding mechanism in an Fe–Mn–C high-Mntwinning-induced plasticity steel," *Scripta Materialia,* vol. 69, no. 1, pp. 53 - 56, 2013.

[135] S. D. Andrews, H. Sehitoglu and I. Karaman, "Constriction energy in the presence of a solute field," *Journal of Applied Physics,* vol. 87, no. 5, pp. 2194 - 2203, 2000.

[136] Z. Wang, H. Bei and I. Baker, "Microband induced plasticity and the temperature dependence of the mechanical properties of a carbon-doped FeNiMnAlCr high entropy alloy," *Materials Characterization,* vol. 139, pp. 373 - 381, 2018.

[137] B. Bay, N. Hansen, D. A. Hughes and D. Kuhlmann-Wilsdorf, "Overview no. 96 evolution of f.c.c. deformation structures in polyslip," *Acta Metallurgica et Materialia,* vol. 40, no. 2, pp. 205 - 219, 1992.

[138] D. Kuhlmann-Wilsdorf, "Theory of Plastic Deformation:- properties of low energy dislocation structures*," *Materials Science and Engineering ,* vol. A113, pp. 1 - 41, 1989.

8.1 Publications from current work

[29] A. S. Tirunilai, J. Sas, K.-P. Weiss, H. Chen, D. V. Szabó, S. Schlabach, S. Haas, D. Geissler, J. Freudenberger, M. Heilmaier and A. Kauffmann, "Peculiarities of deformation of CoCrFeMnNi at cryogenic temperatures," *Journal of Materials Research,* vol. 33, no. 19, pp. 3287 - 3300, 2018.

[30] A. S. Tirunilai, T. Hanemann, C. Reinhart, V. Tschan, K.-P. Weiss, G. Laplanche, J. Freudenberger, M. Heilmaier and A. Kauffmann, "Comparison of cryogenic deformation of the concentrated solid solutions CoCrFeMnNi, CoCrNi and CoNi," *Materials Science and Engineering: A,* vol. 783, pp. 1 - 10 (Art. no. 139290), 2020.

[31] A. S. Tirunilai, T. Hanemann, K.-P. Weiss, J. Freudenberger, M. Heilmaier and A. Kauffmann, "Dislocation-based serrated plastic flow of high entropy alloys at cryogenic temperatures," *Acta Materialia,* vol. 200, pp. 980 - 991, 2020.

9 List of Tables

10 List of Figures

11 Appendix

11.1 Twin boundary estimation

In Sect. 4.2.1, the relative strengthening contribution from deformation twinning was estimated as a function of extent of deformation. The estimation was made using the Eq. 8.1 (same as Eq. 4.4) from Ref. [76].

$$\sigma = \sigma_0 + \frac{f_{twin} \cdot K_{HP}}{\sqrt{\lambda_{twin}}} \qquad \text{Eq. 8.1}$$

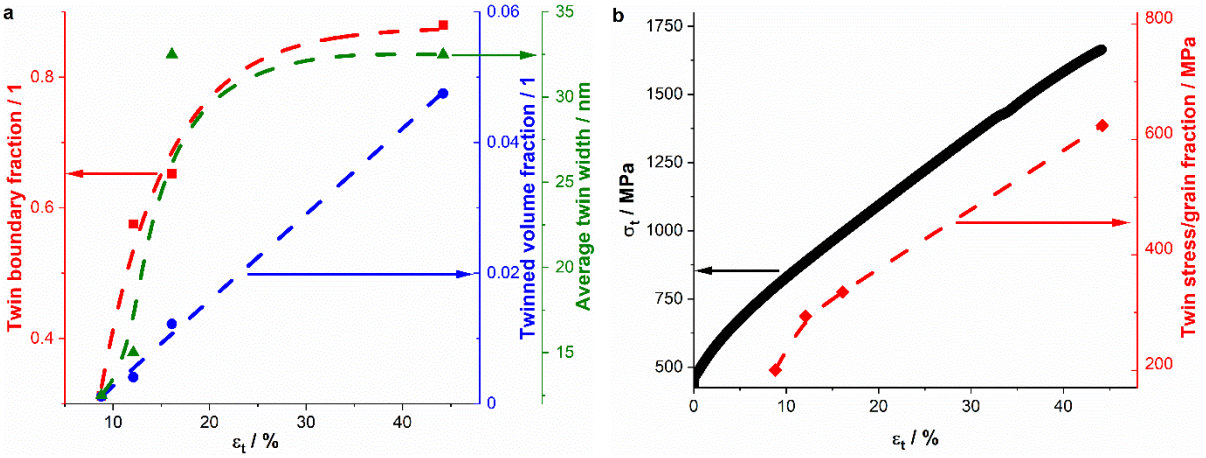

Figure 11.1: (a) Plot of twin boundary length as a fraction of total HAGB length, volume of twinned fraction and average width of deformation twins as a function of true strain. (b) $\sigma_t - \varepsilon_t$ plot of CoCrFeMnNi deformed at 77 K and the calculated stress contribution from twinning based on the increasing twin volume with ε_t. The twin volume fraction and average twin width were taken from Ref. [21]. They were used to calculate twin boundary length, shown in (a), which was subsequently used to estimate twin stress contribution in combination with Eq. 4.4. The stress contribution from twinning was expressed as a function of fraction of grains that exhibited twinning. The calculations were made for a square area of 1000 X 1000 µm side length.

While Otto et al. [12], had already estimated the value of K_{HP}, the other variables in the equation were estimated from Ref. [21]. Laplanche et al. [21] had estimated the progressive change in twin width and twin volume fraction with engineering strain. Fig. 11.1a (same as

Fig. 4.9a) illustrates these values. To estimate twin length and new boundaries introduced through twinning, a hypothetical area of 1000 μm X 1000 μm was considered to be investigated.

It was assumed that twin length is in the order of grain sizes. Additionally, twin boundaries (twin-matrix habit planes) of a single deformation twin were assumed to be parallel to each other. It was also reasonably assumed that twin width is orders of magnitude smaller than twin length. Based on this the total length of twins was calculated using twin width and twin volume fraction given in Ref. [21]. The hypothetical grains presently considered for this evaluation are hexagonal in shape with edge to opposite edge distance of 16 μm. This was the average grain size for the specimens investigated in Ref. [21]. Under these considerations when a certain twin length was calculated as being formed, it was assumed to be distributed uniformly among all the grains. Correspondingly, the addition of n deformation twins to a grain was considered to divide the grain in n+1 parts.

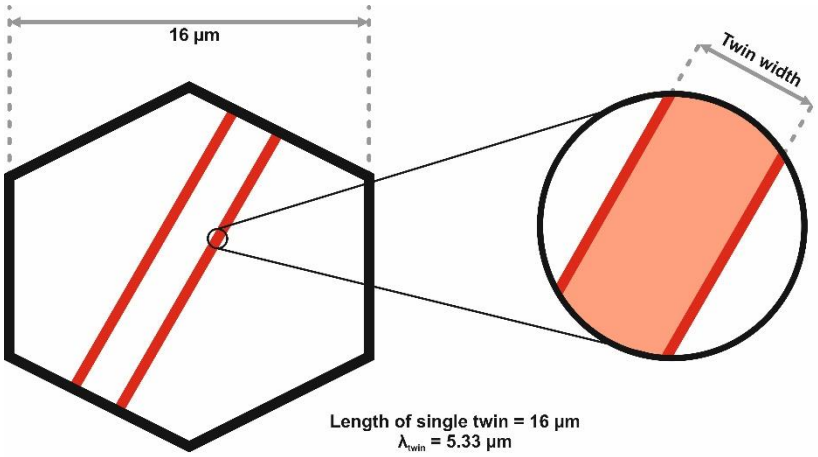

Figure 11.2: A single grain with two deformation twins. For grains of this shape and dimensions, linear grain intercept method results in an average grain size of 16 μm. A close-up of each of the deformation twins is as shown in the circular field to the right. The red highlighted region depicts twinned region and the dark red lines depict twin boundaries. The average twin width is between 10 and 35 nm [21].

Thus, λ_{twin}could be estimated. Using these values, $\frac{f_{twin} \cdot K_{HP}}{\sqrt{\lambda_{twin}}}$ term for stress contribution from twinning could be expressed in terms of fraction of grains that actually undergo twinning. This is seen if Fig. 11.1b (same as Fig. 4.9b). It should be noted that since these

estimations are based multiple assumptions and simplifications, the value is not necessarily reproducible. The purpose of the plot is establishing the significant contribution towards increase in stress from deformation twinning. An accurate estimate would likely result in values in the same range as seen here.

11.2 Serration data estimation

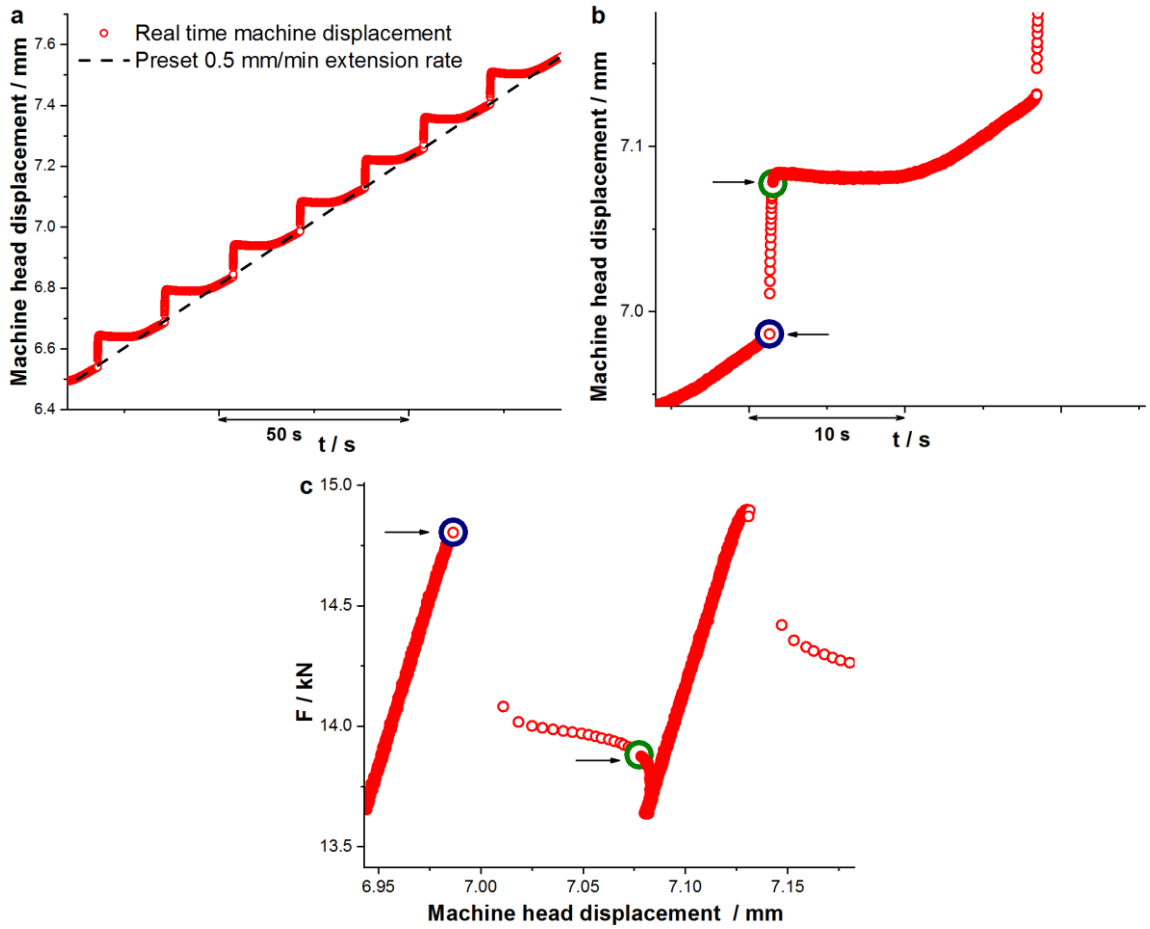

Figure 11.3: (a) Machine displacement vs. time, (b) close up of machine displacement vs. time and corresponding (c) force vs. machine displacement close up. Points marked in blue indicate local maxima while those marked in green indicate local minima. Both maxima and minima points are indicated by arrows as well. For details how these extreme were evaluated, please refer to the text.

Fig. 11.3(a) illustrates the variation of machine displacement as a function of time, while Fig. 11.3(b) is a close-up of the same. For continuous deformation of a specimen, the expectation is that of a positive linear variation of machine displacement with time, equaling

the extension rate of the machine cross-head (marked by the black dashed line in Fig. 11.3(a)). The test is displacement controlled and operates under a preset extension rate, so a sudden stress drop would ideally be accommodated by a corresponding drop in the force applied by the machine to maintain the constant extension rate. However, for a sudden drop in stress (like in the case of a serration), due to the limited stiffness of the machine and a finite reaction time, there is no instantaneous drop in machine force to maintain the extension rate. This results in a sudden and rapid extension event, as seen in Fig. 11.3(b), since the applied force has not been lowered sufficiently yet, to accommodate the preset extension rate. Quickly thereafter, the applied force by the machine is lowered. Though, this drop in force is greater than the drop in force corresponding to stress drop of the specimen. Thus, only a part of the total observed drop in force is a result of contribution form the specimen. To identify the point of transition from drop in force due to specimen to drop in force due to machine overcompensation, the machine displacement is examined. Essentially, since there is a greater drop in applied force than needed to cause plastic deformation in the specimen, the specimen is currently loaded below its elastic limit. Additionally, the current machine displacement rate is higher than the preset 0.5 mm/min. This is accommodated by ensuring no further change in cross-head displacement takes place. This can be seen as the plateau portion in Fig. 11.3(b) following the jump. This continues till the local extension rate is equal to the preset extension rate. This is clear from Fig. 11.3(a) where the dotted line which represents the preset appears as the average of the step like serrated behavior. Based on the above sequence of events, for a single serration there is a stress drop for the specimen followed by an extension in the stress drop form the machine. The latter part provides no additional machine displacement or specimen straining. During the actual stress drop caused by the specimen there is a jump in the machine displacement. Therefore, the start of the serration is marked by the point immediately preceding the jump and the end is marked by the point immediately preceding the plateau of the machine displacement. These sets of points are marked in Fig. 11.3(b) and correspondingly on the stress strain diagrams on Fig. 11.3(c). The stress maxima and minima determined by these methods are significantly more accurate than measurements of absolute maxima and minima for a given serration. This makes comparison between serration data under different experimental conditions plausible. For the test conducted in the ATLAS machine at 4.2 K the minima was taken as the

absolute value. In this case the machine stiffness was extremely high making machine contribution to the stress drop practically negligible.

12 Permission for use of published content

Listed below are the licenses allowing the use of previously published work in the current thesis [29, 58, 99, 128]. No licenses were required for content use from Refs. [30, 31].

1) Tirunilai et al. [29]

SPRINGER NATURE LICENSE TERMS AND CONDITIONS
Mar 12, 2021

This Agreement between Mr. Aditya Srinivasan Tirunilai ("You") and Springer Nature ("Springer Nature") consists of your license details and the terms and conditions provided by Springer Nature and Copyright Clearance Center.

License Number	5026480724589
License date	Mar 12, 2021
Licensed Content Publisher	Springer Nature
Licensed Content Publication	Journal of Materials Research
Licensed Content Title	Peculiarities of deformation of CoCrFeMnNi at cryogenic temperatures
Licensed Content Author	Aditya Srinivasan Tirunilai et al
Licensed Content Date	Oct 1, 2018
Type of Use	Thesis/Dissertation
Requestor type	academic/university or research institute
Format	print and electronic
Portion	full article/chapter
Will you be translating?	no
Circulation/distribution	1 - 29
Author of this Springer Nature content	yes
Title	Cryogenic deformation of CoCrFeMnNi with a focus on serrated plastic deformation
Institution name	Karlsruhe Institute of Technology
Expected presentation date	Jun 2021
Requestor Location	Mr. Aditya Srinivasan Tirunilai Engelbert-Arnold-Strasse 4 Building 10.91 R310 Karlsruhe, 76131 Germany Attn: Mr. Aditya Srinivasan
Total	0.00 EUR

2) Varvenne et al. [58]

ELSEVIER LICENSE
TERMS AND CONDITIONS

Mar 12, 2021

This Agreement between Mr. Aditya Srinivasan Tirunilai ("You") and Elsevier ("Elsevier") consists of your license details and the terms and conditions provided by Elsevier and Copyright Clearance Center.

License Number	5026481177689
License date	Mar 12, 2021
Licensed Content Publisher	Elsevier
Licensed Content Publication	Acta Materialia
Licensed Content Title	Theory of strengthening in fcc high entropy alloys
Licensed Content Author	Céline Varvenne,Aitor Luque,William A. Curtin
Licensed Content Date	Oct 1, 2016
Licensed Content Volume	118
Licensed Content Issue	n/a
Licensed Content Pages	13
Start Page	164
End Page	176
Type of Use	reuse in a thesis/dissertation
Portion	figures/tables/illustrations
Number of figures/tables/illustrations	1
Format	both print and electronic
Are you the author of this Elsevier article?	No
Will you be translating?	No
Title	Cryogenic deformation of CoCrFeMnNi with a focus on serrated plastic deformation
Institution name	Karlsruhe Institute of Technology
Expected presentation date	Jun 2021
Portions	Figure 2
Requestor Location	Mr. Aditya Srinivasan Tirunilai Engelbert-Arnold-Strasse 4 Building 10.91 R310 Karlsruhe, 76131 Germany Attn: Mr. Aditya Srinivasan
Publisher Tax ID	GB 494 6272 12
Total	0.00 EUR

3) Skoczeń et al. [99]

ELSEVIER LICENSE
TERMS AND CONDITIONS

Mar 12, 2021

This Agreement between Mr. Aditya Srinivasan Tirunilai ("You") and Elsevier ("Elsevier") consists of your license details and the terms and conditions provided by Elsevier and Copyright Clearance Center.

License Number	5026480298480
License date	Mar 12, 2021
Licensed Content Publisher	Elsevier
Licensed Content Publication	International Journal of Plasticity
Licensed Content Title	Constitutive model of discontinuous plastic flow at cryogenic temperatures
Licensed Content Author	B. Skoczeń,J. Bielski,S. Sgobba,D. Marcinek
Licensed Content Date	Dec 1, 2010
Licensed Content Volume	26
Licensed Content Issue	12
Licensed Content Pages	21
Start Page	1659
End Page	1679
Type of Use	reuse in a thesis/dissertation
Portion	figures/tables/illustrations
Number of figures/tables/illustrations	2
Format	both print and electronic
Are you the author of this Elsevier article?	No
Will you be translating?	No
Title	Cryogenic deformation of CoCrFeMnNi with a focus on serrated plastic deformation
Institution name	Karlsruhe Institute of Technology
Expected presentation date	Jun 2021
Portions	Figure 4 and Figure 6
Requestor Location	Mr. Aditya Srinivasan Tirunilai Engelbert-Arnold-Strasse 4 Building 10.91 R310 Karlsruhe, 76131 Germany Attn: Mr. Aditya Srinivasan
Publisher Tax ID	GB 494 6272 12
Total	0.00 EUR
Terms and Conditions	

4) Nagai et al. [128]

SPRINGER NATURE LICENSE
TERMS AND CONDITIONS

Mar 12, 2021

This Agreement between Mr. Aditya Srinivasan Tirunilai ("You") and Springer Nature ("Springer Nature") consists of your license details and the terms and conditions provided by Springer Nature and Copyright Clearance Center.

License Number	5026480517503
License date	Mar 12, 2021
Licensed Content Publisher	Springer Nature
Licensed Content Publication	Springer eBook
Licensed Content Title	Effects of Gage Diameter and Strain Rate on Tensile Deformation Behavior of 32Mn-7Cr Steel at 4 K
Licensed Content Author	Kotobu Nagai, Tetsumi Yuri, Yuji Nakasone et al
Licensed Content Date	Jan 1, 1986
Type of Use	Thesis/Dissertation
Requestor type	academic/university or research institute
Format	print and electronic
Portion	figures/tables/illustrations
Number of figures/tables/illustrations	1
Will you be translating?	no
Circulation/distribution	1 - 29
Author of this Springer Nature content	no
Title	Cryogenic deformation of CoCrFeMnNi with a focus on serrated plastic deformation
Institution name	Karlsruhe Institute of Technology
Expected presentation date	Jun 2021
Portions	Figure 8
Requestor Location	Mr. Aditya Srinivasan Tirunilai Engelbert-Arnold-Strasse 4 Building 10.91 R310 Karlsruhe, 76131 Germany Attn: Mr. Aditya Srinivasan
Total	0.00 EUR

13 Acknowledgements

This thesis could not have been done without the help and support of several people both within and outside the Institute for Applied Materials – Materials Science and Engineering (IAM-WK) at the Karlsruhe Institute of Technology (KIT).

Firstly, I would like to thank Prof. Heilmaier for the opportunity to work in the Physical Metallurgy group (PhM) and pursue my doctorate. I am grateful for the chance to work in a supportive scientific environment where I could realize productive research. I am also grateful for the consistent and timely feedback on several matters, both technical and presentational, during the course of the doctorate. I take this opportunity to thank Prof. Gunther Eggeler for his willingness to provide a second review for this thesis. This thesis would have been inconceivable without the constant support from Dr. Alexander Kauffmann. His consistent guidance on all matters, small and large has been a crucial part of my doctorate. Dr. Kauffmann's strong willed focus during times of stagnation and patience during setbacks were a big part of achieving fruitful results. Most of all, his openness to discuss topics, often twice or thrice, gave me the confidence to tackle problems and move forward. I wholeheartedly thank him for all the support and guidance he has provided. I am thankful for the funding received by the Deutsche Forschungsgemeinschaft, specifically though the Schwerpunktprogramm (SPP 2006: grants no. KA 4631/1-1 and WE 6279/1-1).

I was consistently helped by my colleagues and collaborators throughout the course of my time at Karlsruhe. An integral part of the work was carried out by my project partner Ms. Theresa Hanemann in the Institute for Technical Physics. Her work ethic was inspirational and her ideas were greatly helpful in achieving success. I would like to thank Dr. Klaus-Peter Weiss for the opportunity to carry out experiments under his supervision. His guidance is greatly appreciated. I would also like to thank Dr. Jan Sas, Mr. Valentin Tschan and Mr. Lukas Kneller for all the help they provided me in carrying out the cryogenic tensile tests. I was also greatly aided by my colleagues in the PhM group. Dr. Hans Chen and Dr. Sascha Seils, never failed to provide guidance and support when needed. Dr. Seils' words of encouragement were very helpful. I am thankful to Mrs. Camelia Schulz for the interesting scientific discussions we had and for being there for me during tumultuous times. I am

grateful to Dr. Ulla Hauf for helping me navigate the waters early on and for all the advice she gave me. A special thanks goes to Mr. Stephan Laube for the daily discussions we had. The critical approaches developed during these discussions helped shape many of my scientific arguments. He has also proven to be an invaluable friend and I thank him for his friendship. I would like to thank the various members of PhM, including, Dr. Anke Schmitt, Dr. Daniel Schliephake, Ms. Susanne Obert, Ms. Frauke Hinrichs, Mr. Georg Winkens and Mr. Ioannis Sprenger, for their insightful feedback as well as support. I was greatly helped by Ms. Antje Dollmann. Her clarifications and descriptions greatly benefited my work and I appreciate all of the talks we had. Practically all the specimens I worked on were processed in some way at in Leibniz Institute for Solid State and Materials Research (IFW) Dresden by Prof. Jens Freudenberger. His constant support as well as incisive feedback on a multitude of technical matters served to enrich my thesis. I greatly appreciate all that he has done. Part of the characterization for my work was carried out at Ruhr University Bochum in the laboratory of Dr. Guillaume Laplanche. I would like to thank him for this as well as his astute observations and comments on the work. It was quite helpful in improving its quality. I would like to thank Mr. Christian Reinhart for all the work he did with the TEM characterization. I take this opportunity to thank Prof. Ian Baker of the Thayer school of Engineering, Dartmouth College, for sharing raw material which proved useful in the course of research. I would also like to thank my student assistants during my term at KIT, including Mr. Simon Kunz, Ms. Marla Braun, Mr. Iskandar Ghariani and Mr. Shrey Thakkar for their work. Throughout the course of my work I was frequently helped, guided and endured by the various members of IAM-WK who constantly accommodated me. To that end, I would especially like to thank Mrs. Michaela Nagel and Mrs. Nadine Kandora-Mann at the Metallography laboratory and Mrs. Bianka Konstantin.

Finally, such an endeavor would not have been possible had I not been unfailingly sustained by my friends and family. I am thankful to my mother for all the love and support she gave me, for her unfailing faith in my abilities and her confidence in my success, regardless of the situation. I am grateful for the example my father set and the lessons I learnt from him, they were undeniably needed during my doctoral studies. A sincere thanks goes to Dr. Jeyaraam Ramanarayanan, who was always present for scientific discussions as well as an open ear for problems. I also thank Ms. Shakthipriya Bhaskar, who was always available for a consultation

on both technical and personal issues. I am grateful to Ms. Basabdatta Gupta for all the times she was there for me. She has truly been a supportive and understanding friend. I also thank my other friends, Mr. Sandeep Bindiganavile Satyanarayana, Mr. Rakesh R. Kamath, Mr. Aditya Patel, Mr. Ghanashyam Vinod Tatti, Ms. Silva Basu and Mr. Sridhar Kamoji, who were subjected to multiple unannounced calls, only to be both encouraging and kind. I also thank Mr. Russ Kyle for staying on me and helping me strive for bigger things. My friends and family have made me feel loved and appreciated and reassured me at every turn. I am truly grateful for all that they have done for me.